Article

# Hierarchically Porous Osteoinductive Poly(hydroxyethyl methacrylate-*co*-methyl methacrylate) Scaffold with Sustained Doxorubicin Delivery for Consolidated Osteosarcoma Treatment and Bone Defect Repair

S. Sreeja, Ramesh Parameshwar, P. R. Harikrishna Varma, and G. S. Sailaja*

Cite This: https://dx.doi.org/10.1021/acsbiomaterials.0c01628

Read Online

ACCESS | Metrics & More | Article Recommendations | Supporting Information

**ABSTRACT:** A bifronted cure system for osteosarcoma, a common aggressive bone tumor, is highly in demand to prevail the postsurgical adversities in connection with systemic chemotherapy and repair of critical-size bone defects. The hierarchically porous therapeutic scaffolds presented here are synthesized by free radical-initiated copolymerization of hydroxyethyl methacrylate and methyl methacrylate [HEMA/MMA 80:20 and 90:10 mM, $H_2O$/NaCl porogen], which are further surface-phosphorylated [P-PHM] and transformed to bifunctional by impregnating doxorubicin (DOX) [DOXP-PHM]. The P-PHM scaffolds exhibited porous microarchitecture analogous to native cancellous bone (scanning electron microscopy analysis), while X-ray photoelectron spectroscopy analysis authenticated surface phosphorylation. Based on pore characteristics, swelling attributes and slow-pace degradation, P-PHM9163 and P-PHM8263 (HEMA/MMA 90:10 and 80:20 with $H_2O$/NaCl: 60/3.0 weight %, respectively) were chosen from the series and evaluated for osteoinductive efficacy *in vitro*. Both P-PHM9163 and P-PHM8263 invoked calcium phosphate mineralization in simulated physiological conditions (day 14) with Ca/P ratios of 1.58 and 1.66 respectively, comparable to human bone (1.67). Early biomineralization (Alizarin Red S and von Kossa staining) was evidenced at day 7, while osteoblast differentiation was verified by time-dependent expression of the typical late marker, osteocalcin, at day 14 and 21 in rat bone marrow mesenchymal cells. DOX-loaded P-PHM9163 (DOXP-PHM9163) exhibited pH-responsive (tumor analogous pH; 6.5) sustained release of DOX for prolonged time (up to 45 days) and invoked cellular alterations by cortical stress fiber formation and DNA fragmentation in human osteosarcoma cells leading to early apoptosis (24 h), validated by annexin V/PI staining (FACS) and immunostaining (F-actin/DAPI). Subsequent to DOX release tenure, the scaffold induced the formation of well-organized, porous post-release Ca-P apatite coating (Ca/P is 1.3) in simulated body fluid (day 14) which further endorses the dual functionality of the system. Altogether, the results accentuate that DOXP-PHM9163 is a potential bifunctional therapeutic scaffold capable of extended localized chemotherapeutic delivery in-line with inherent osteogenesis for efficient bone cancer treatment.

**KEYWORDS:** apoptosis, bifunctional, biomineralization, bone regeneration, porous copolymer, osteosarcoma, sustained release
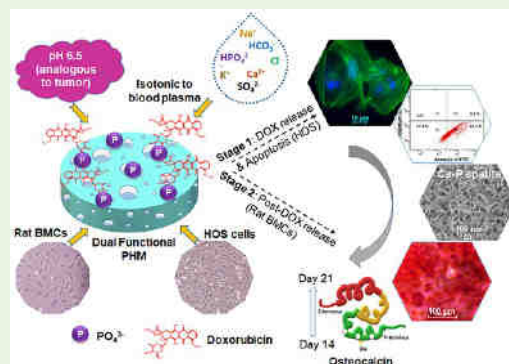
## 1. INTRODUCTION

Osteosarcoma is the most common aggressive primary malignancy among bone tumors (3−5%) highly prevalent in the age group less than 30 years. It is hallmarked by immature osteoid tissue formation elicited by uncontrolled proliferation and differentiation of osteoprogenitor cells.[1,2] The present conservative mode of treatments predominantly employ pre- and/or postoperative chemotherapy/radiation in conjunction with surgery in order to condense tumor mass prior to surgery and subsequently eradicate residual tumor cells after resection, respectively. The neoadjuvant and adjuvant chemotherapy together with surgery have led to a revolutionary progress in long-term survival rate of osteosarcoma patients.[3,4] Despite these advancements in therapeutic measures, shortcomings still persists that give rise to critical challenges in safeguarding the life of survivors. Of these setbacks, chronic systemic toxicity of chemotherapeutics owing to its nonlocalized administration became the primary concern in the orthopedic clinical sector. Besides irreversible systemic toxicity, nonspecific administration also reduces availability of therapeutic dosage at the target site because of rapid clearance from the circulatory system.[5]

**Scheme 1. Schematic Representation of Free Radical-Initiated Copolymerization of HEMA and MMA**
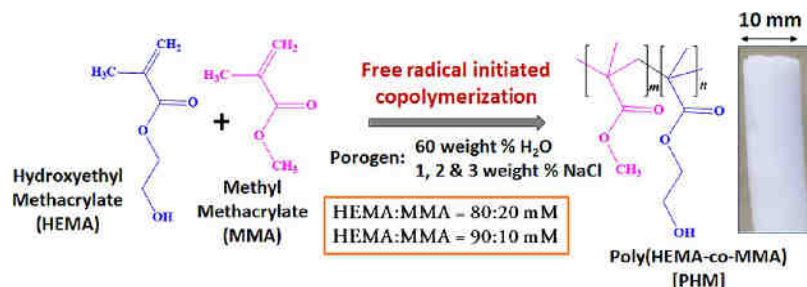


Further, the structural intricacy as well as highly metastatic nature of the tumor prevent complete annihilation by surgical resection, leading to its recurrence. Moreover, the bone deformities may be of large size that prohibit self-healing mechanism of bone and calls for additional management to rectify the defect. Altogether, there is an inevitable requirement of two different therapeutic measures to address the postsurgery care more effectively.

Based on recent advancements in tissue engineering, an increasing volume of research has been concentrating on the development of bone substitutes with custom-made micro-architecture and physicomechanical properties comparable to native bone.[6] Bioactive three-dimensional (3D) porous polymer or ceramic scaffolds or its conjugated forms have been considered as a judicious choice of bone substitutes which can mimic the host tissue to facilitate nutrient transfer and subsequently establish cellular and molecular signaling pathways to ensure defective bone restoration.[7−11] In addition, nanoparticle-based localized drug delivery vehicles have been found effective for specific bone cancer therapy.[12,13] However, a therapeutic system which can address both adjuvant chemotherapy and repair of bone defect would be the preferred choice to overcome the aforementioned adversities of contemporary treatment modalities.

Dual-functional bone substitutes are anticipated to function by sustained localized release of anticancer agents which mitigate residual cancer cells through prolonged, tumor-specific mode of action and induce osteogenesis afterward as a second phase. While designing such a dual functional bone graft for osteosarcoma treatment, pore characteristics and biodegradation profile play pivotal roles in dictating controlled release of the chemotherapeutics.[14] Bone grafts such as poly-$\varepsilon$-caprolactone loaded with doxorubicin or dexamethasone have been investigated for localized tumor therapy and bone cell regeneration.[15,16] In addition, polymer or nanoparticle or its complexes—aided drug delivery systems have been proposed for bone cancer treatment to ensure therapeutic specificity.[12,13,17] However, it is pertinent to disclose that development of an osteoinductive scaffold with sustained drug delivery potential holding optimal porosity, mechanical strength and desired biodegradation profile simultaneously is indeed a challenging task.

Poly(hydroxyethyl methacrylate) [poly(HEMA)], owing to its well-known hydrogel characteristics, excellent biocompatibility and capability to complex with other molecules through its −OH group, is highly acceptable for diverse biomedical applications.[18−21] However, excessive swelling elicits necessity for modifications of this biocompatible hydrogel to further modulate its physicochemical, mechanical and bifunctional characteristics, thereby customizing its biodegradation profile.[22] Our previous reports testify that 2-hydroxy ethyl

methacrylate (HEMA) can be effectively used to impart functionalization to the methyl methacrylate solid polymer [methyl methacrylate (MMA) and HEMA molar ratio is 0.90:0.07], where the −OH groups of HEMA in the copolymer led to surface phosphorylation and promoted bone bonding *in vivo*.[23,24]

Inspired from our previous findings, here, we present porous bifunctional poly(HEMA-*co*-MMA) therapeutic scaffolds synthesized with reverse composition of HEMA and MMA at two different millimolar ratios (HEMA/MMA 90:10 and 80:20). The therapeutic copolymer scaffold with a customized biodegradation profile and hierarchical porosity was synthesized by free radical copolymerization employing biocompatible porogens ($H_2O$/NaCl), followed by surface phosphorylation and impregnation of doxorubicin (DOX). The bifunctionality of the scaffold with respect to drug delivery and *in vitro* osteogenesis was validated by pH-triggered sustained DOX release in tumor analogous pH and in rat bone marrow mesenchymal cells [rBMC(s)], respectively.

## 2. EXPERIMENTAL SECTION

**2.1. Materials.** HEMA, MMA, benzoyl peroxide (BPO), ethylene glycol dimethacrylate (EGDMA), phosphorus pentoxide ($P_2O_5$),
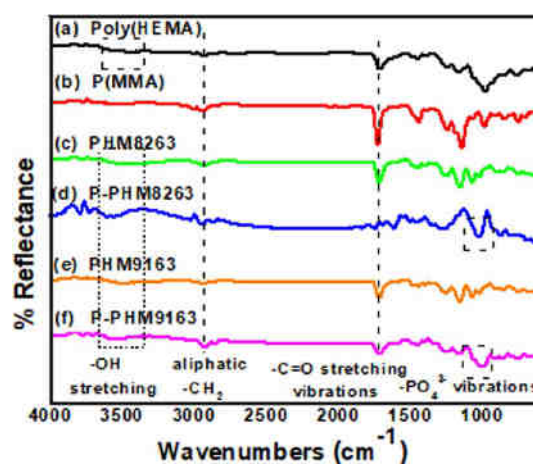


**Figure 1.** ATR spectra of (a) poly(HEMA), (b) poly(MMA) [P(MMA)], (c) PHM8263, (d) P-PHM8263, (e) PHM9163 and (f) P-PHM9163.

phosphoric acid, and chemicals for phosphate-buffered saline (PBS), phosphate buffer (PB) and simulated body fluid (SBF) were procured from Merck, India. Doxorubicin hydrochloride (DOX) was purchased from AK scientific, United States. Dulbecco's modified eagle medium (DMEM) and fetal bovine serum (FBS) were purchased from Gibco, Thermo Fischer Scientific, India, while other reagents for cell culture
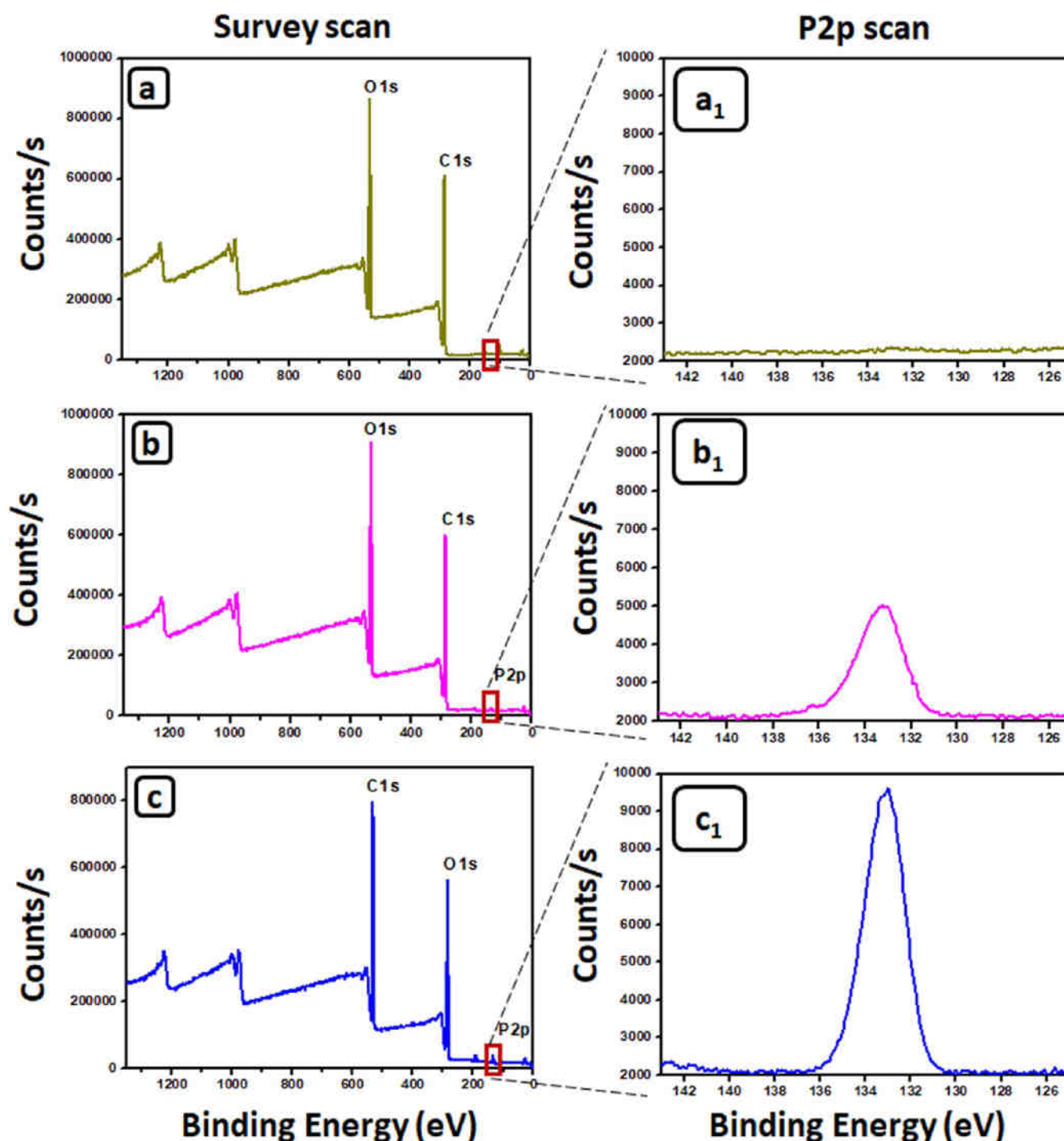
**Figure 2.** XPS survey scan recorded on PHM9163 (a), P-PHM8263 (b) and P-PHM9163 (c). Typical high-resolution P2p scan of PHM9163, P-PHM8263 and P-PHM9163 are presented as ($a_1$), ($b_1$) and ($c_1$), respectively.

were purchased from HiMedia, India. All chemicals used for the present study were of analytical grade.

**2.2. Methods.** *2.2.1. Synthesis of Porous PHM Scaffolds.* Poly(HEMA-*co*-MMA) [PHM] scaffolds with hierarchical porous structures were synthesized by free radical-initiated copolymerization reaction (Scheme 1) of monomers HEMA and MMA at 80:20 and 90:10 mM ratios using 0.5 weight % BPO as the initiator and 60 weight % water with 1−3 weight % NaCl as porogen in RB flask at 80 °C under constant stirring. Cross-linking was established with 0.01 weight % of EGDMA. Viscosity of the prepolymer increases as the polymerization reaction propagates and transferred to a cylindrical mold (inner diameter is 1 cm) which was then allowed to complete

polymerization at 80 °C in a hot air oven. The PHM collected was washed several times with Milli-Q ultrapure water to remove the porogen/unreacted monomers, dried, and cut into discs of ∼1 mm thickness and used for the experiments. The scaffolds from 80:20 series were labelled as PHM82, PHM8261, PHM8262 and PHM8263, while 90:10 series were marked as PHM91, PHM9161, PHM9162 and PHM9163 ("6" indicates 60 weight % water; "1", "2" and "3" represent amount of NaCl).

*2.2.2. Surface Functionalization of PHM Scaffolds.* The PHM scaffolds were surface-phosphorylated as per our previously reported protocol with slight modifications.[24,25] Briefly, PHM scaffolds were treated with 76% (w/v) $P_2O_5$, and the phosphorylation reaction was
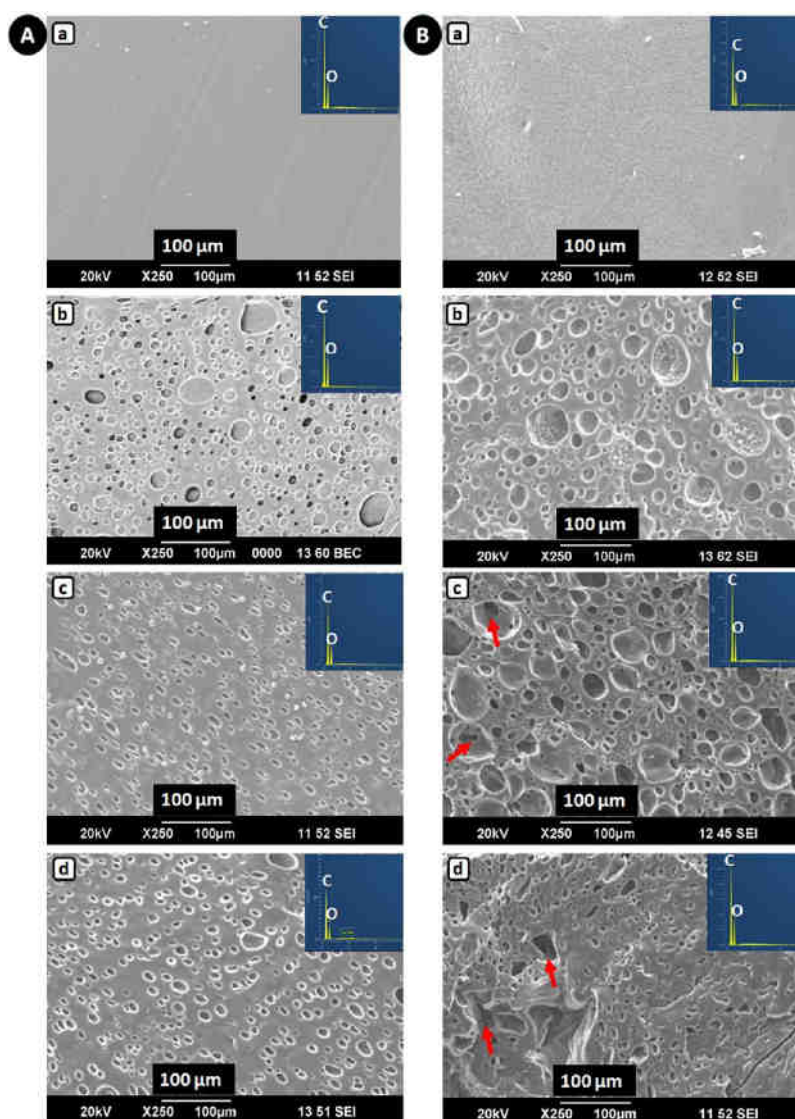
C

**Figure 3.** SEM images of PHM scaffolds. (A) 80:20 series, where (a−d) are PHM82, PHM8261, PHM8262 and PHM8263, respectively; (B) 90:10 series, where (a−d) are PHM91, PHM9161, PHM9162 and PHM9163, respectively. Red arrows indicate deep pores. EDX spectra (presented as inset) depict peaks corresponding to the elements C and O.

performed at 50 °C for 1 h. The unreacted medium was removed by washing with distilled water until neutral pH and air-dried at 37 °C. The scaffolds were renamed as P-PHM82, P-PHM8261, P-PHM8262, P-PHM8263, P-PHM91, P-PHM9161, P-PHM9162 and P-PHM9163 respectively, after surface phosphorylation.

*2.2.3. Physicochemical Characterizations of the Scaffolds.* The polymerization reaction was confirmed by attenuated total reflection (ATR) analysis (FTIR Prestige 21, Shimadzu, Japan) at a resolution of 4 cm$^{-1}$. The surface morphology, porosity and pore diameter of the scaffolds were analyzed using scanning electron microscopy (SEM; JEOL model JSM-6390LV) complemented with energy-dispersive X-ray analysis (EDX) and elemental mapping (OXFORD XMX N) which provide information about the surface-bound phosphate groups. The surface phosphorylation of PHM scaffolds was confirmed by X-ray photoelectron spectroscopy (XPS) (Thermo Fischer Scientific ESCALAB Xi+, India) analysis.

*2.2.4. Porosity Measurement.* The gravimetric method was used to determine porosity of the scaffolds.[26] Density of the scaffolds [$\rho$(scaffold)] and actual density of the polymer [$\rho$(polymer)] were computed to calculate porosity as per eq 1.

$$\text{Porosity of scaffolds (\%)} = \left(1 - \frac{\rho(\text{scaffold})}{\rho(\text{polymer})}\right) \times 100 \tag{1}$$

*2.2.5. In Vitro Swelling and Degradation Study.* The water absorption capacity of PHM scaffolds was determined as per the protocol described previously.[27] For this, triplicates of the samples in separate containers were immersed in PBS (1×; pH 7.34) at 37 °C for 5 days and weight of the swollen samples at predefined time points were recorded. Degree of swelling was calculated as per eq 2. The effect of surface functionalization on hydrophilicity of the scaffolds was evaluated by comparing the swelling degree of phosphorylated samples with nonphosphorylated samples.

$$\text{Degree of swelling (\%)} = \frac{M_{\text{w}} - M_{\text{d}}}{M_{\text{d}}} \times 100 \tag{2}$$

where $M_{\text{w}}$ and $M_{\text{d}}$ are wet mass and dry mass of the scaffold, respectively.

Further, the static water contact angle goniometry (ramé-hart instrument co.) was performed with the scaffolds by the sessile-drop method to validate the wettability. After exposure to the water droplet (~4 μL) for 20 s, the contact angle measurements were carried out at five distinct locations of the scaffold.
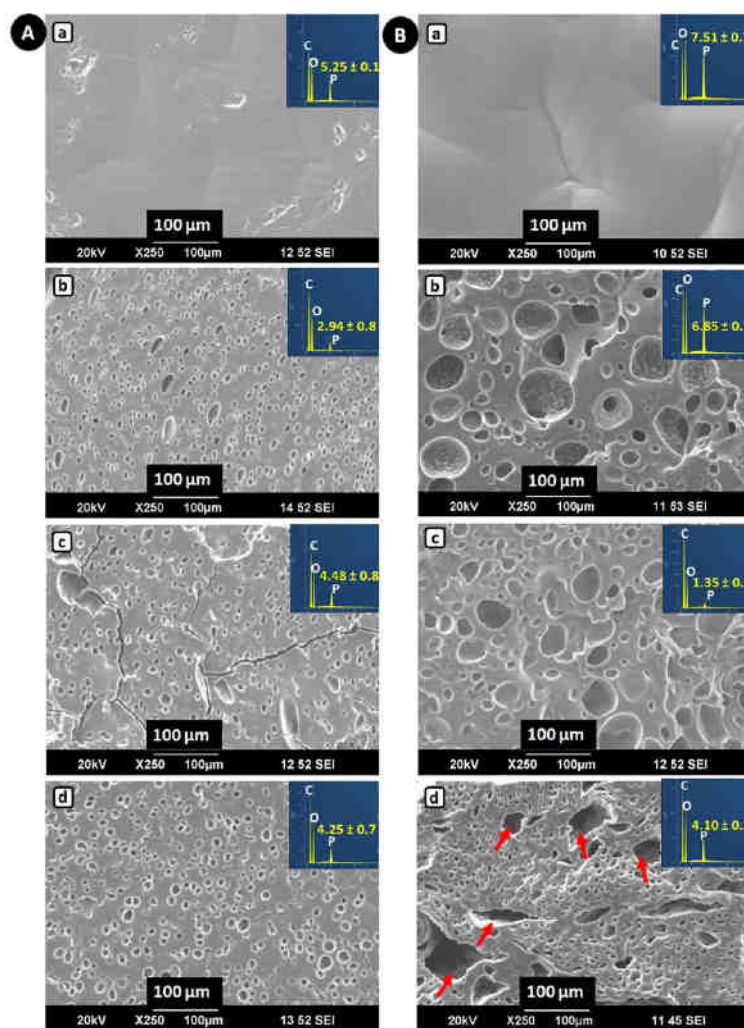
**Figure 4.** SEM images of phosphorylated PHM scaffolds. (A) 80:20 series in which (a−d) are P-PHM82, P-PHM8261, P-PHM8262 and P-PHM8263, respectively; (B) 90:10 series in which (a−d) are P-PHM91, P-PHM9161, P-PHM9162 and P-PHM9163, respectively. Red arrows indicate deep, interconnected pores. Corresponding EDX spectra depicting the phosphate group in terms of P (atomic %) are presented as the inset.

**Table 1. Porosity of PHM and P-PHM Scaffolds with Different Compositions**[a]

| PHM Scaffolds | Porosity (%) | P-PHM Scaffolds | Porosity (%) |
|---|---|---|---|
| PHM8261 | 25.4 ± 3.0 | P-PHM8261 | 22.2 ± 3.5 |
| PHM8262 | 24.7 ± 10.0 | P-PHM8262 | 25.7 ± 1.5 |
| PHM8263 | 29.9 ± 7.1 | P-PHM8263 | 28.3 ± 4.6 |
| PHM9161 | 30.6 ± 3.2 | P-PHM9161 | 20.4 ± 8.0 |
| PHM9162 | 40.5 ± 9.2 | P-PHM9162 | 29.2 ± 6.8 |
| PHM9163 | 42.7 ± 9.6 | P-PHM9163 | 35.6 ± 6.6 |

[a]Note: all values are presented as mean ± SD. There are no statistically significant variations in porosity ($p > 0.05$) observed when compared with respective samples.

*In vitro* degradation behavior was assessed by incubating the scaffolds in PBS (pH 7.34) under dynamic condition at 37 °C for 60 days. The buffer was replaced at every 24 h to ensure constant pH. Percentage degradation of the scaffolds was calculated as per eq 3.[28,29]

$$\text{Degradation of the scaffold (\%)} = \frac{M_i - M_t}{M_t} \times 100 \qquad (3)$$

where $M_i$ and $M_t$ are the initial weight and weight of the sample after degradation, respectively. Based on the outputs of SEM analysis, swelling and degradation studies, P-PHM9163 and P-PHM8263 were chosen for further investigations.

*2.2.6. Compression Strength.* Compression strength of PHM9163 and P-PHM9163 scaffolds was determined according to ASTM standard (D 695-96) using Universal Testing Machine (Instron, UK). A crosshead speed of 0.5 mm/min was used to determine compression stress and Young's modulus.

*2.2.7. Cell Viability and Cell Adhesion.* Cytocompatibility of the scaffolds was assessed by 3-(4,5-dimethylthiazol-2-yl)-2,5-diphenylte-trazolium bromide (MTT) assay. Human osteosarcoma cells, MG-63, obtained from National Centre for Cell Science (NCCS), Pune, India were cultured in complete cell culture medium [DMEM along with 10% FBS and 1% penicillin−streptomycin solution]. The extracts of the scaffolds ($n = 4$) were prepared in the medium at 37 ± 2 °C for 24 h according to the ISO 10993 guideline. The extracts were filtered (0.22 $\mu$m filter membrane) and used for the assay. The cells at a density of $1 \times 10^4$ cells/well were seeded to 96 well plate, and 100 $\mu$L of the extract was added after the cells attained normal adhered morphology. MTT (0.5 mg/mL) was added to the culture at predefined time points (24 h and day 5) and incubated for 4 h at 37 °C in CO$_2$ incubator. The formazan crystals formed were solubilized with dimethyl sulfoxide, and absorbance was measured at 570 nm.
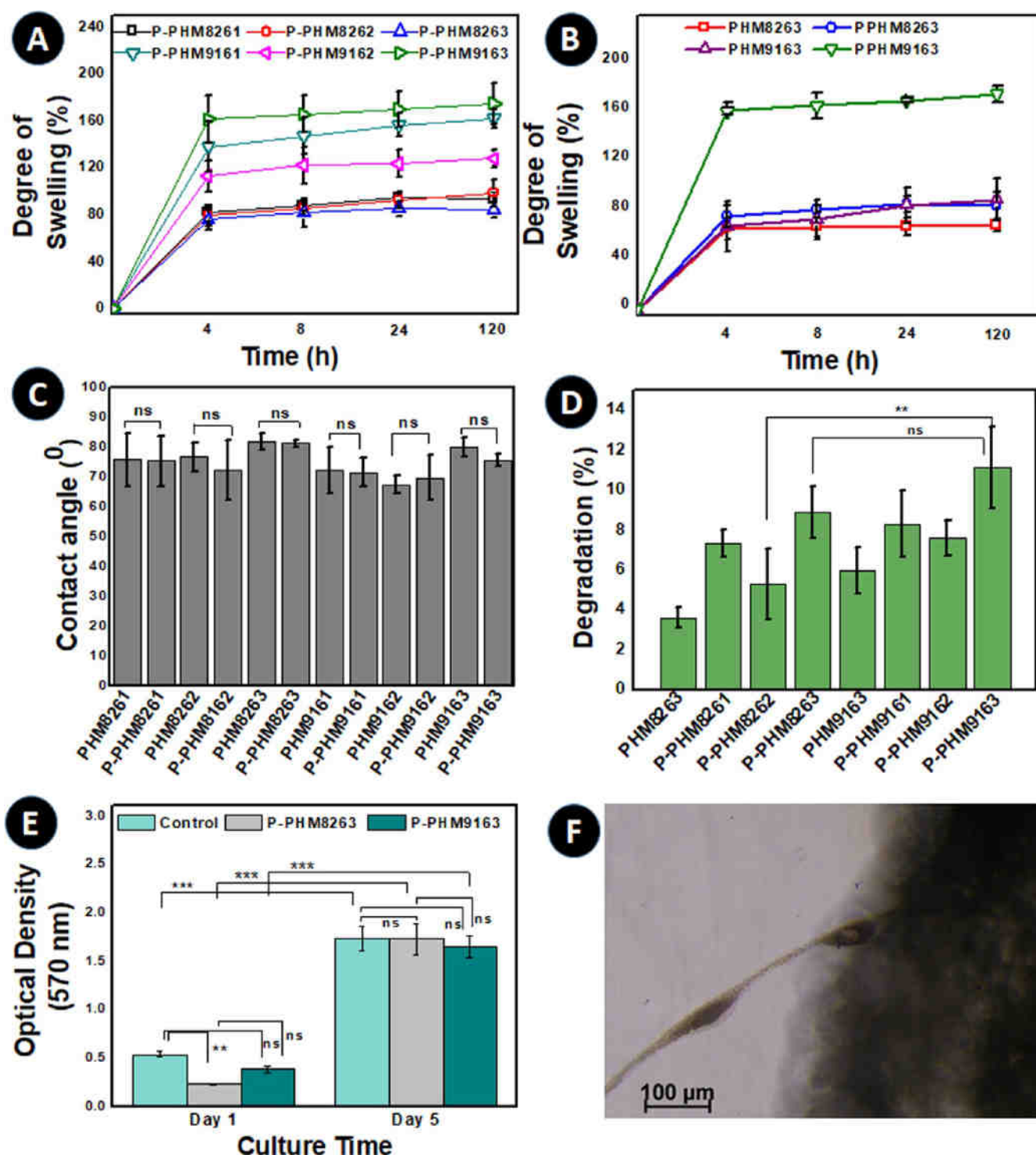
**Figure 5.** (A) Swelling behavior of P-PHM scaffolds (90:10 and 80:20); (B) difference in degree of swelling between PHM and P-PHM scaffolds; (C) contact angle values of PHM and P-PHM scaffolds; (D) *in vitro* degradation (%) profile of P-PHM scaffolds; (E) cell viability data by MTT assay performed in MG-63 cells; and (F) optical microscopic image of MG-63 cells adhered on P-PHM9163 (scaffold appears as black). Note: all values are presented as mean $\pm$ SD. "ns" indicates statistical nonsignificance ($p > 0.05$), while "**" and "***"represent statistical significance ($p < 0.01$ and $p < 0.001$, respectively)].

The cell viability was expressed in terms of optical density (570 nm).[30] Further, the microscopic images of MG-63 cells cultured on the scaffolds were captured to visualize cell−material interaction.

*2.2.8. Evaluation of In Vitro Mineralization in SBF.* The scaffolds having dimensions 10 mm diameter and 1 mm height were used for *in vitro* mineralization assay in SBF with ionic concentrations similar to human blood plasma as detailed by Kokubo and Takadama, 2006.[31]

The scaffolds were incubated in SBF (pH 7.4) at 37 °C for 14 days, refreshed the medium at every 24 h and collected on day 7 and 14. The scaffolds were washed carefully to remove excess ions and dried at 37 °C for overnight. Field emission SEM (FESEM)−EDX (Carl Zeiss Sigma, Germany; XFlash 6I100 Bruker, USA) analysis was performed to observe the biomimetic mineralization and to calculate Ca/P ratio.
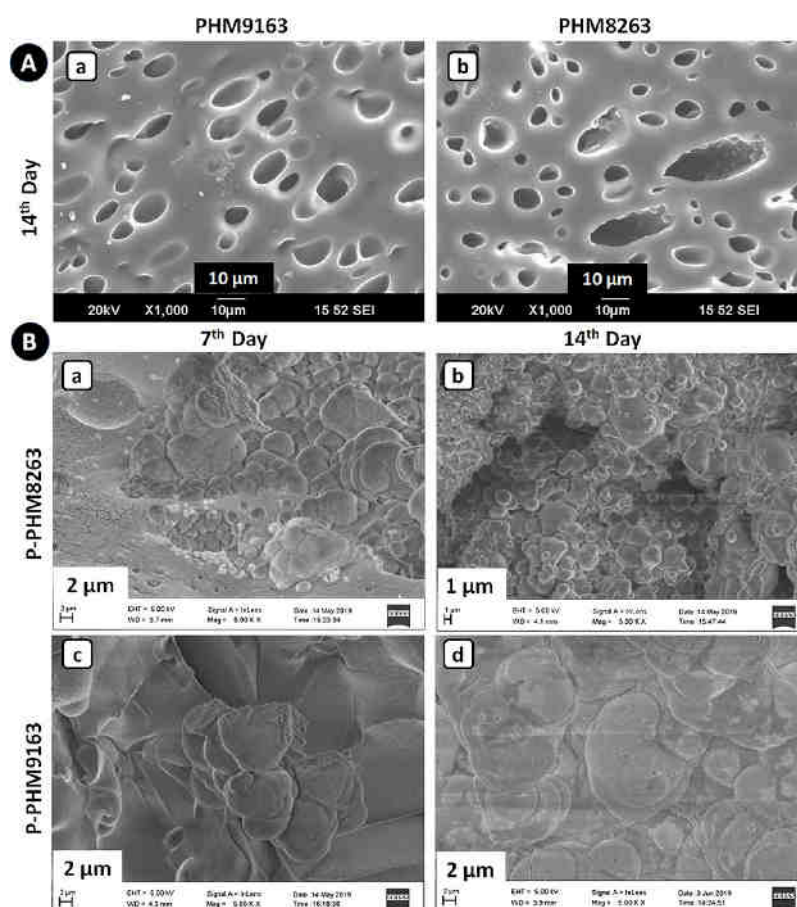
**Figure 6.** *In vitro* biomimetic mineralization. (A) SEM images of unmodified scaffolds (PHM9163 and PHM8263) on day 14. (B) FESEM images of mineralized scaffolds [(a): P-PHM8263-7th day; (b): P-PHM8263-14th day; (c): P-PHM9163-7th day; and (d): P-PHM9163-14th day].

**2.2.9. Isolation of rBMC(s).** The rBMCs were isolated from Sprague Dawley rat's femur bone according to a protocol we have optimized recently.[29] Prior approval from Institutional Animal Ethics Committee has been taken for rBMCs isolation (363/GO/Re/S/01/CPCSEA, 28.12.2017/07). The isolated rBMCs were cultured in complete cell culture medium [DMEM with 10% (v/v) FBS and 1% (v/v) antibiotic solution] in a $CO_2$ incubator (New Brunswick Galaxy 170 S, Germany). After two days of culture, the unattached cells were washed off and the culture was continued until third passage. The cells were then used for conducting biofunctional assays to evaluate new bone formation potential of the scaffolds.

**2.2.10. Evaluation of Morphology of rBMCs.** The rBMCs at a density of $1 \times 10^4$ cells/well were seeded on P-PHM8263 and P-PHM9163 scaffolds in a 24-well plate in order to observe the morphology of adhered cells on the scaffolds. Following 5 days of culture, the cells were fixed with 2.0% (v/v) glutaraldehyde solution, washed carefully with cacodylate buffer (0.2 M; pH 7.34), and dehydrated by graded alcohol.[32] Finally, the scaffolds were air-dried and gold-sputtered prior to FESEM imaging.

**2.2.11. Alizarin Red S and von Kossa Staining.** The rBMCs ($1 \times 10^4$ cells) were cultured on P-PHM8263 and P-PHM9163 scaffolds ($n$ = 3; 10 mm diameter × 1 mm height) in complete DMEM for 14 days. Alizarin Red S (ARS) and von Kossa (VK) staining were performed to evaluate the biomineralization potential of the scaffolds according to the previously reported protocols with minor modifications.[33−35] On 14th day of culture, the cells on the scaffolds were fixed with 4% (w/v) paraformaldehyde (PFA) and stained with 40 mM ARS (pH 4.2) for 20 min with continuous shaking. Subsequently, the scaffolds were washed to remove unbound stain and finally observed using a phase-contrast inverted microscope (Nikon Eclipse Ti2 Series, India). In the case of VK staining, the cells were fixed with 4% (w/v) PFA, treated with 5% (w/v) silver nitrate

solution and exposed to UV light for 20 min. The reaction was arrested by 5% (w/v) sodium thiosulphate and viewed under the phase contrast microscope (Nikon Eclipse Ti2 Series, India). The control cells (cells cultured without scaffold) and unmodified scaffolds (PHM8263 and PHM9163) with dimensions 5 mm × 5 mm (diameter × height) were also treated in the same way for both staining methods.

**2.2.12. Assessment of Osteocalcin activity by ELISA.** The late osteogenic marker, osteocalcin, was quantified to analyze the osteoblast formation on the scaffolds. For this, the rBMC cells ($1 \times 10^4$ cells) were cultured on the scaffolds ($n$ = 6) in complete DMEM (D). After 48 h, three of the scaffolds ($n$ = 3) were supplemented with osteogenic differentiation media (ODM; O) (Himedia Pvt. Ltd, India), while the remaining three ($n$ = 3) from all groups were retained as such. The cells supplemented with ODM were maintained as positive controls, while the cells cultured in DMEM without scaffolds were kept as negative controls. The medium was refreshed at every 48 h. The cells were harvested at specified time points (day 14 and 21), and the cell lysate was prepared by frequent freeze−thaw method with PBS. The osteocalcin activity was quantified using the rat osteocalcin/bone Gla protein ELISA kit (Origin diagnostics, India) as per the manufacturer's protocol. The result is expressed as ng/mg protein. Protein estimation was carried out by the procedure reported by Lowry et al.[36]

**2.2.14. Actin/DAPI Staining.** Human osteosarcoma cells, HOS, were seeded ($3 \times 10^3$ cells) on surface-coated glass coverslips in a 24-well cell culture plate and allowed to attain their normal morphology. The cells were then treated with the extracts, containing DOX, released from DOXP-PHM8263 (31 $\mu$M) and DOXP-PHM9163 (43 $\mu$M) in PBS after 24 h of incubation. The cells were fixed with 4% (w/v) PFA for 30 min after 24 and 48 h of treatment and subsequently permeabilized with 50% ice-cold methanol for 10 min.
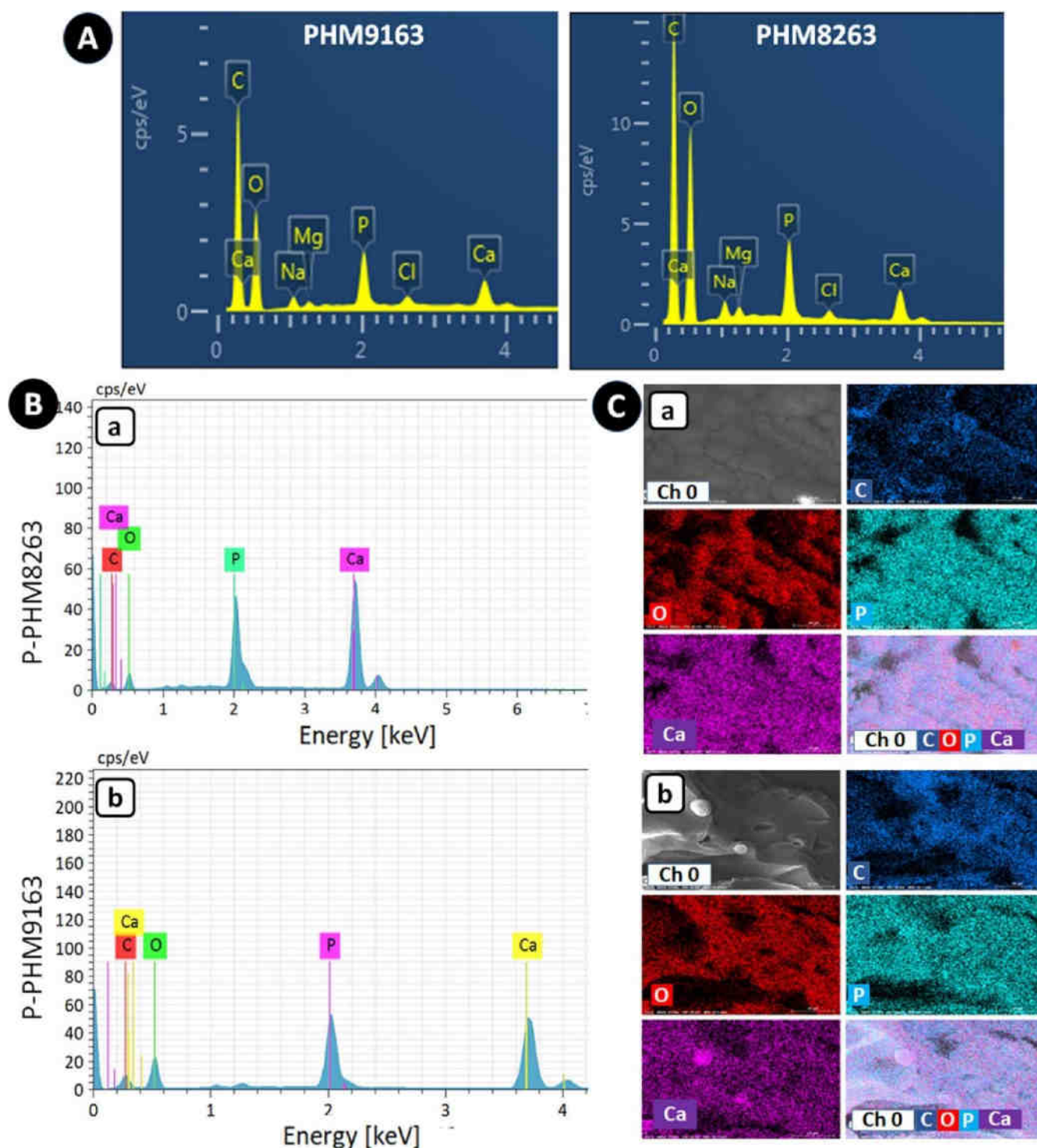
**Figure 7.** EDX spectra and elemental mapping of the scaffolds after incubation in SBF for 14 days. (A) EDX spectra (14th day) of PHM scaffolds; (B) EDX spectra of P-PHM scaffolds [(a) P-PHM8263-14th day and (b) P-PHM9163-14th day]; (C) elemental mapping of P-PHM scaffolds [(a) P-PHM8263-14th day and (b) P-PHM9163-14th day]. Elemental mapping illustrates individual element distribution of C, O, P and Ca along with its merged form.

After blocking with bovine serum albumin [2% (w/v)], the cells were stained with Alexa Fluor 488 Phalloidin (Thermo Fisher Scientific, India) to visualize F-actin cytoskeleton of the cells followed by counterstaining of the nuclei with 4′,6-diamidino-2-phenylindole (DAPI). The fluorescent images of the cells were captured (60× magnification; oil immersion) using phase-contrast inverted fluorescent microscope (Nikon Eclipse Ti2 Series, India).

Further, DOXP-PHM9163 scaffolds were incubated with HOS cells (1 × 10⁴ cells per well) cultured in a 6-well plate for 48 h and measured pH of the culture media at pre-defined time intervals (2, 4, 6, 24 and 48 h), in order to observe the influence of early release of DOX on pH of the tumor microenvironment (*in vitro*). The untreated cells were used as the control group of this experiment. Subsequent to DOX release for 48 h, the scaffolds were gently washed with PBS

**Table 2. Ca and P (atomic %) of PHM and P-PHM Scaffolds after Incubation in SBF[a]**

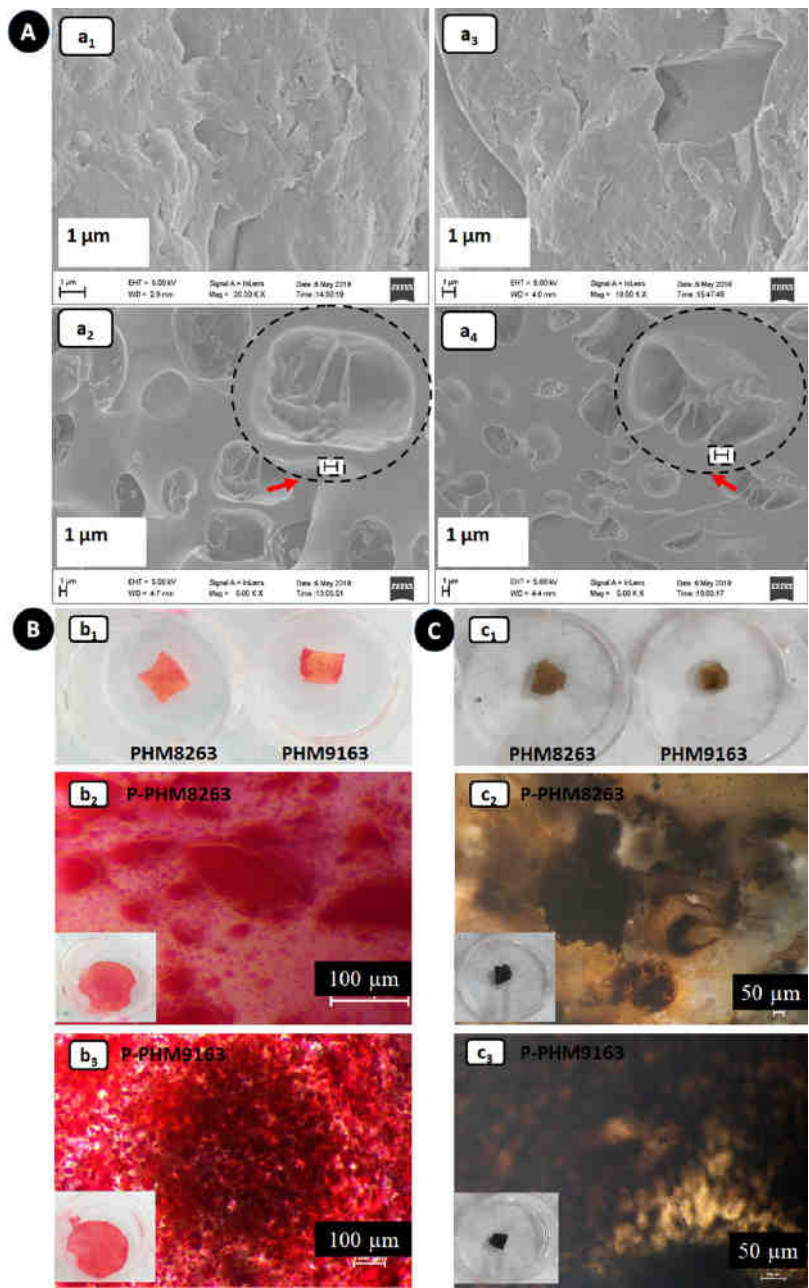| Immersion time | Elements | PHM8263 | P-PHM8263 | PHM9163 | P-PHM9163 |
|---|---|---|---|---|---|
| 7th day | Ca | | $0.54 \pm 0.37$ | | $2.04 \pm 1.40$ |
| | P | | $0.33 \pm 0.18$ | | $2.45 \pm 1.18$ |
| | Ca/P | | 1.63 | | 0.83 |
| 14th day | Ca | $0.8 \pm 0.05$ | $10.25 \pm 1.35$ | $1.58 \pm 0.09$ | $14.9 \pm 5.63$ |
| | P | $1.51 \pm 0.04$ | $6.49 \pm 1.57$ | $0.99 \pm 0.07$ | $8.95 \pm 2.50$ |
| | Ca/P | 0.53 | 1.58 | 0.63 | 1.66 |

[a]Note: all values are presented as mean $\pm$ SD.



**Figure 8.** rBMCs adhesion and biomineralization of P-PHM scaffolds. (A) FESEM images of P-PHM scaffolds after incubation with rBMCs, where (a$_1$) and (a$_2$) represent P-PHM8263, while (a$_3$) and (a$_4$) indicate P-PHM9163 [magnified images are in dotted circle; scale bar is 1 $\mu$m]. (B) ARS staining of unmodified (b$_1$) and modified (b$_2$: P-PHM8263 and b$_3$: P-PHM9163) scaffolds. (C) VK staining of unmodified (c$_1$) and modified (c$_2$: P-PHM8263 and c$_3$: P-PHM9163) scaffolds.

(1×) and SEM analysis (SEM; JEOL model JSM-6390LV) was performed to investigate its microarchitecture.

*2.2.15. Annexin V/PI Dual Staining.* A quantitative assessment of cell death following treatment with DOX released from DOXP-PHM9163 has been performed by fluorescein isothiocyanate (FITC)-
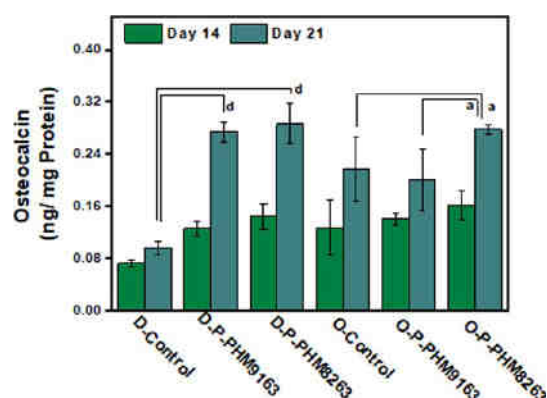
**Figure 9.** Osteoblast differentiation potential of the scaffolds—osteocalcin level [note: D-control, D-P-PHM9163 and D-P-PHM8263 indicate the treatment groups were supplemented with DMEM, while O-control, O-P-PHM9163, and O-P-PHM8263 represent the treatment groups supplemented with osteogenic medium. Note: all values are presented as mean ± SD. "a" indicates statistical nonsignificance ($p > 0.05$) and "d" represents statistical significance ($p < 0.001$)].

conjugated annexin V apoptosis assay using FITC Annexin V Apoptosis Detection Kit I (BD Pharmingen). Briefly, the HOS were cultured ($1 \times 10^6$ cells) in cell culture flasks (25 cm$^2$) and allowed to reach adhered morphology. The cells were then treated with DOX (released from DOXP-PHM9163 for 24 h in DMEM) for 24 h. The

cells treated with Triton X-100 (0.005% in complete DMEM) serve as positive control, while the cells without any treatments have been taken as negative control for the study. After incubation, the cells were harvested by trypsinization, washed with PBS and re-suspended in annexin binding buffer to obtain a concentration of ∼$1 \times 10^6$ cells/mL. Subsequently, annexin V and PI were added and incubated for 15 min in dark at room temperature as per the manufacturer's protocol. Soon after the staining process, flow cytometric analysis was executed to determine apoptotic and nonapoptotic cell population using fluorescence-activated cell sorting (FACS) (BD Bioscience).

*2.2.16. In Vitro Mineralization Potential of DOXP-PHM9163 Scaffolds after DOX Release.* Subsequent to the cumulative release of DOX, the DOXP-PHM9163 was incubated in SBF and collected at day 14 to observe their mineralization efficacy by FESEM−EDX. This study serves as a reference to the biomineralization potential of the bifunctional scaffold after its function as localized drug (DOX) delivery vehicle.

*2.2.13. Preparation of DOX-Loaded PHM Scaffolds and In Vitro DOX Release Study.* The chemotherapeutic agent DOX was incorporated into P-PHM9163 and P-PHM8263 scaffolds of size 1 cm × 0.1 cm (diameter × height), labelled as DOXP-PHM9163 and DOXP-PHM8263 respectively, in order to transform the scaffolds as a bifunctional system. The microarchitecture and hydrophilicity of the scaffolds are anticipated to offer eligibility to act as a bifunctional system. Precisely, the scaffolds were incubated with 100 mL of DOX solution in distilled water (0.1 mg/mL) for 48 h in dynamic conditions at 37 °C. The drug-loaded scaffolds were washed for multiple times with distilled water to remove unbound DOX. The concentration of DOX loaded into the scaffolds was calculated by eq 4.[6]
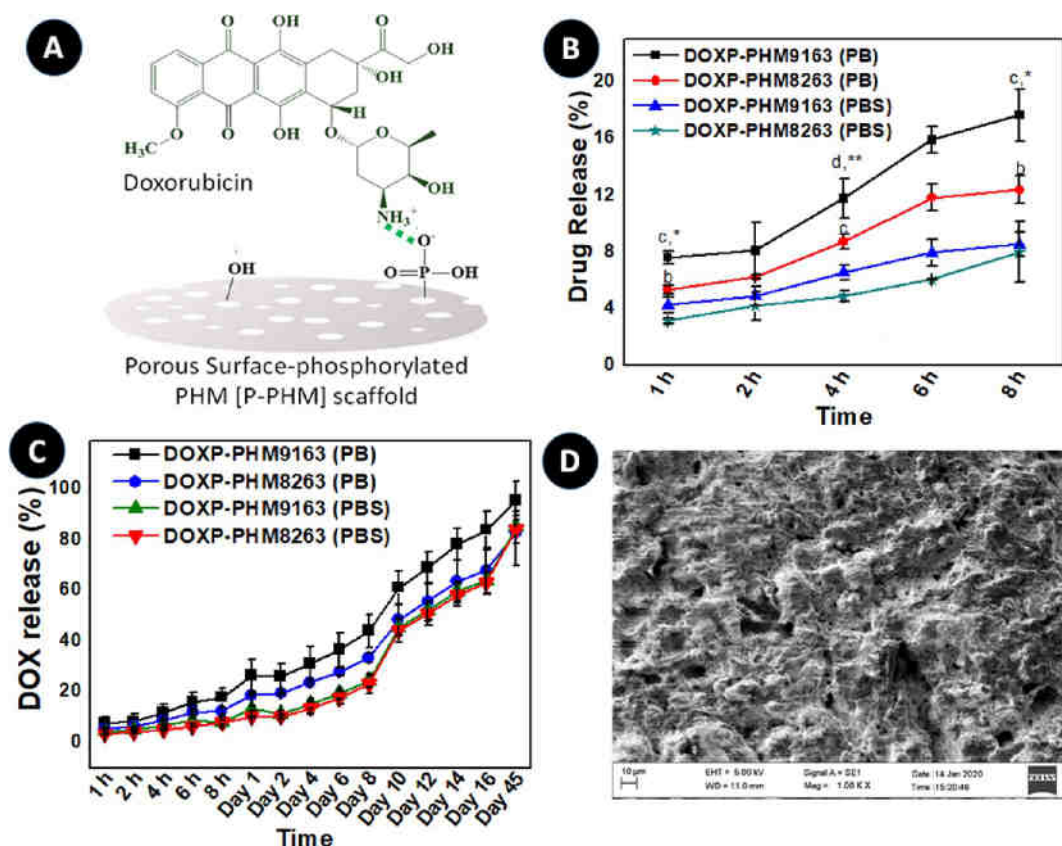


**Figure 10.** Cumulative release profile of DOX from DOXP-PHM9163 and DOXP-PHM8263 in PB (pH 6.5) and PBS (pH 7.34). (A) Schematic presentation of possible interaction between the phosphorylated scaffold and DOX; (B) DOX release for short period of time; (C) DOX release for prolonged period of 45 days; (D) FESEM image depicting surface morphology of DOXP-PHM9163 after DOX release for 45 days (scale bar is 10 μm). Note: all values are presented as mean ± SD. "b" and "*", "c" and "**", and "d" indicate statistical significance ($p < 0.05$, $p < 0.01$, $p < 0.001$, respectively) compared with DOXP-PHM9163 (PBS) and DOXP-PHM8263 (PB).
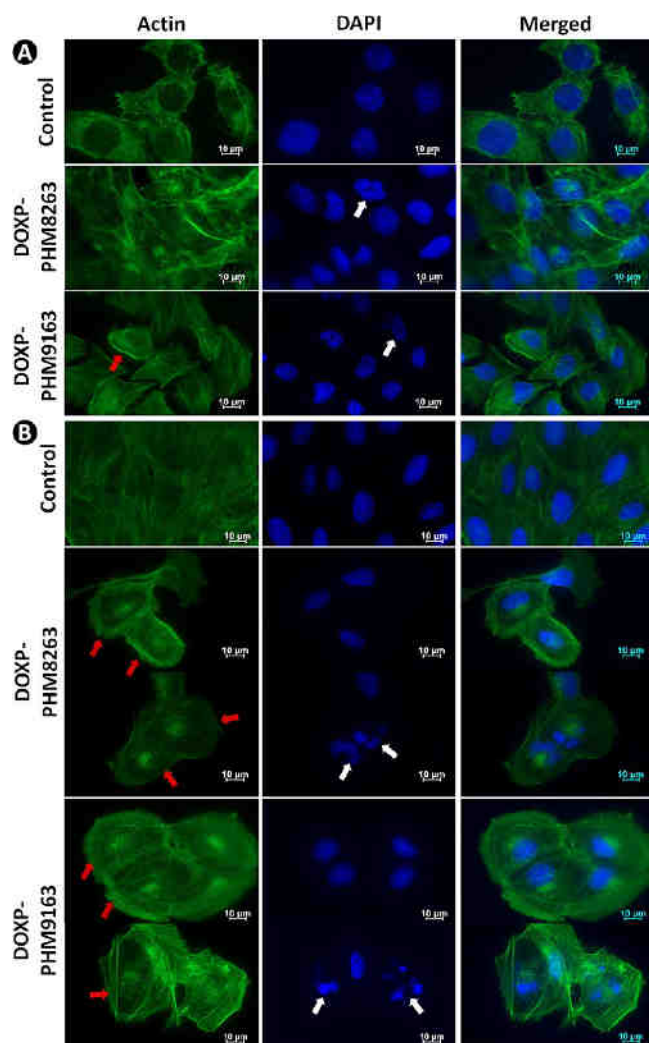
**Figure 11.** DOX released from DOXP-PHM scaffold-induced alterations in actin cytoskeleton and nuclei of HOS cells. (A,B) Representative images of F-actin (green) and DAPI (blue)-stained cells treated for 24 and 48 h respectively, where white arrows highlight fragmented nuclei and red arrows indicate cortical ring formation. Scale bar is 10 $\mu$m.

Percentage of DOX loaded

$$= \frac{Initial\ DOX\ concentration - Unbound\ DOX\ concentration}{Initial\ DOX\ concentration}$$

$$\times\ 100 \tag{4}$$

DOX release was determined by incubating the scaffolds in PBS (pH 7.34) at 37 ± 2 °C in dynamic condition (60 rpm). To mimic the slightly acidic pH of tumor microenvironment (pH 6.0−6.9), the scaffolds were also incubated in PB (pH 6.5) at the same conditions.[37,38] At specified time intervals, 1 mL of the release medium was collected from each set of the samples and replaced with equal volume of fresh medium up to 45 days. The concentration of DOX in the release medium was calculated by measuring absorbance at 480 nm using a multiwell plate reader (Spark Multimode Microplate Reader, Tecan, Switzerland).

*2.2.17. Statistical Analysis.* All the values are presented as mean ± SD. The level of statistical significance was measured by Tukey's multiple comparison test using GraphPad Instat3 software.

**2.3. Results and Discussion.** *2.3.1. Physicochemical Characterization of PHM and P-PHM Scaffolds.* ATR spectral analysis carried out in PHM scaffolds (Figure 1) provided confirmative evidences of copolymerization. The ATR spectrum of poly(HEMA) has a broad

peak at 3556 cm$^{-1}$ that corresponds to −OH stretching, while the characteristic peak at 1713 cm$^{-1}$ is ascribed to stretching vibrations of ester carbonyl, C═O [Figure 1a]. An additional small peak appeared at 2930 cm$^{-1}$ is contributed to stretching vibrations of −CH$_2$ (aliphatic).[39,40] Peaks corresponding to stretching vibrations of C═O and aliphatic −CH$_2$ were viewed in the spectrum of PMMA depicted in Figure 1b.[41] The poly(HEMA-*co*-MMA) (PHM scaffolds) exhibited characteristic peaks of C═O and −CH$_2$ stretching of both HEMA and MMA [Figure 1c−f] along with −OH stretching of HEMA.[42] In addition, ATR analysis has imparted information on phosphorylation of poly(HEMA-*co*-MMA), evidenced by the peak at 1008 cm$^{-1}$ in P-PHM9163 and P-PHM8263 [Figure 1d,f] responsible for PO$_4^{3-}$ asymmetric vibration.[43]

The XPS data (Figure 2) authenticate surface functionalization of the scaffolds. Survey spectra of the scaffolds exhibited characteristic peaks of C1s and O1s signals [Figure 2a−c]. The peak with binding energy of 133 eV corresponding to P2p signal is viewed for phosphorylated scaffolds—P-PHM9163 and P-PHM8263—[Figure 2b$_1$,c$_1$], while PHM9163 is devoid of it [Figure 2a$_1$], approving the surface modification of PHM scaffolds by phosphorylation.[44] High intensity of the P2p signal observed in P-PHM9163 [Figure 2c$_1$] can be attributed to the presence of more phosphate groups, generated through binding sites contributed by extra −OH groups of HEMA, in the 90:10 series which is greater than 80:20 series.

Surface microarchitecture of the scaffolds harvested by SEM analysis has revealed a nearly smooth surface devoid of apertures for PHM82 and PHM91 (without porogen) [Figure 3A(a),B(a)]. Because porosity plays a pivotal role in scaffold systems employed for bone regeneration applications,[45,46] pores have been introduced in the PHM scaffolds (*in situ*) with the aid of porogen illustrated by corresponding SEM micrographs [Figure 3A(b−d),B(b−d)]. In 80:20 series, majority of the pores are <10 $\mu$m in diameter, while pores with an average size of 75 $\mu$m along with micropores are discerned in 90:10 series. It is noteworthy to mention that even after surface phosphorylation, the scaffolds retained open-porous microstructure [Figure 4]. Further, interconnectivity of the pores can also be viewed from the micrographs [Figure 4B(d)]. The EDX spectra of the scaffolds are presented as insets in Figures 3 and 4.

Subsequently, the porosity (%) of the scaffolds (pre- and post-modification) was estimated and is presented in Table 1. The scaffolds that belong to 90:10 series (PHM9161, PHM9162 and PHM9163) exhibited slightly greater porosity (30.6 ± 3.2, 40.5 ± 9.2 and 42.7 ± 9.6%, respectively) compared to 80:20 series [PHM8261 (25.4 ± 3.0%), PHM8262 (24.7 ± 10.0%) and PHM8263 (29.9 ± 7.1%)]. A small decline in porosity was observed after phosphorylation, and highest porosity was detected for P-PHM9163 and P-PHM8263, the compositions with highest concentration of porogen from 90:10 and 80:20 series, respectively.

Literature testifies that 3D scaffolds with graded porosity are ideal to enhance tissue regeneration through cell adhesion, nutrient transport, cell migration and angiogenesis.[45,46] The scaffolds with micropores (<10 $\mu$m) support impregnation of nutrient media and provide specific protein binding sites owing to increase in surface area which promotes bone cell adhesion, while pores of >100 $\mu$m size invoke cell proliferation and vascularization.[47,48] Hence, the PHM scaffolds with pores of different size categories demonstrated its suitability as a matrix for inductive bone regeneration.

In conjunction with microarchitecture, success of a scaffold also relies on comparable mechanical properties with that of host tissue. The compression strength and modulus of the scaffold PHM9163 before and after phosphorylation was evaluated (data are not presented). The PHM9163 has an average compressive stress of 10.9 ± 4 MPa at maximum load (932 ± 140 N) and modulus of 153 ± 33 MPa, while P-PHM9163 has 7.1 ± 2 MPa (547 ± 101 N) and 67.6 ± 12 MPa, respectively. This observation can be well correlated with our previous finding that surface phosphorylation of the copolymer scaffold reduces compressive strength.[24] However, it is significant to note that the mechanical properties of these surface-functionalized scaffolds are matching well with the requirements for human cancellous bone.[49,50] Most importantly, on the contrary to the
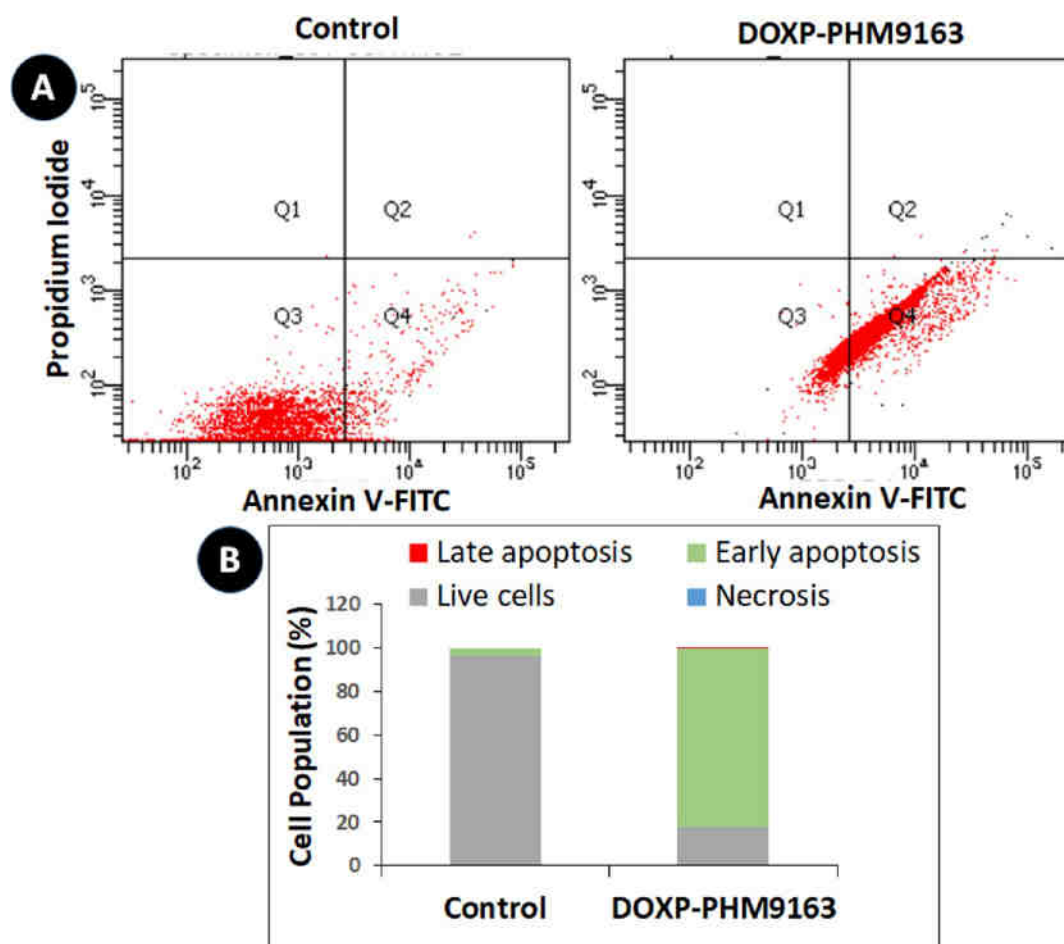
**Figure 12.** Annexin V/PI double staining of HOS cells treated with the extract of DOXP-PHM9163 for 24 h. (A) Representative scatter plots of FACS analysis following treatment with DOX-released from DOXP-PHM9163. $[(Q_1)$ necrotic cells—annexin $V^-/PI^+$; $(Q_2)$ late apoptotic cells—annexin $V^+/PI^+$; $(Q_3)$ live cells—annexin $V^-/PI^-$; $(Q_4)$ early apoptotic cells—annexin $V^+/PI^-]$. (B) Percentage cell population in each quadrant.

general fact, a positive correlation with porosity (Table 1) and mechanical strength was developed which imparts desirable properties to the scaffolds for bone tissue regeneration.

*2.3.2. Surface Phosphorylation has Substantial Effect on Swelling Behavior and Degradation of PHM Scaffolds.* The water retention and thereby swelling of porous scaffolds have huge impact on the degree of bone tissue regeneration as it opens up pores which consequently enhances surface area for better attachment and further proliferation of the cells.[51,52] The phosphorylated porous scaffolds of the 90:10 group (PHM9161, PHM9162 and PHM9163) exhibited higher degree of swelling (>100%) within 4 h of incubation in PBS than that of the 80:20 group (~75%) [Figure 5A]. This can be ascribed to the greater number of −OH groups contributed by HEMA for 90:10 scaffold category compared to 80:20. The influence of phosphorylation on water uptake capacity of the scaffolds was also evaluated (Figure 5B). The unmodified scaffolds (PHM8263 and PHM9163) exhibited 65 and 67% of swelling respectively, while the same increased to 75 and 160% for P-PHM8263 and P-PHM9163 respectively, within 4 h of incubation in PBS (pH 7.34 and temperature 37 °C). Thereafter, the scaffolds attained saturation in swelling with no further water uptake upon prolonged incubation, observed as a plateau, which helps to maintain the structural integrity and stability of the scaffolds. These alterations in swelling behavior of these surface-modified scaffolds are mainly contributed by the phosphate groups. Altogether, a synergistic effect of higher degree of phosphorylation (evidenced from XPS analysis) and hydroxyl groups has led to greater extent of swelling for P-PHM scaffolds of the 90:10 group.[24]

The porous scaffolds have displayed water contact angle values <90° (Figure 5C) offering corroborative evidences to the hydrophilic nature of the scaffolds.[53] However, there were no statistically significant changes in hydrophilicity noticed following surface phosphorylation. In the contact angle measurements, the interaction of liquid with the scaffold is only for a few seconds, thereby measuring merely the hydrophilicity at the scaffold surface. Nevertheless, long-term exposure of the scaffolds in aqueous milieu (swelling studies) allows in-depth penetration of the surrounding medium through the interconnected pores which provides opportunity to interact with more number of hydrophilic functional groups and thereby improves its water uptake capacity following surface phosphorylation.

While considering the prerequisites of a polymer matrix for bone regeneration applications, a controlled degradation profile is one of the major attributes. We have evaluated *in vitro* degradation potential of the scaffolds, and the result is provided in Figure 5D. It is apparent that the PHM scaffolds did not undergo rapid degradation by immersion in PBS (pH 7.34) at dynamic conditions. P-PHM8263 and P-PHM9163 exhibited degradation of 9 and 11% respectively, during the incubation period of two months. This dilatory mode of degradation emphasizes the suitability of the scaffolds for bone regeneration as it can provide adequate timely support before its complete degradation.[51]

Based on aforementioned characterizations—microstructure, *in vitro* swelling and degradation profile, the scaffolds P-PHM9163 and P-PHM8263 from series 90:10 and 80:20, respectively, were selected for biofunctional evaluation.

*2.3.3. In Vitro Biocompatibility of P-PHM Scaffolds.* MTT assay was performed with the extracts of P-PHM8263 and P-PHM9163 in
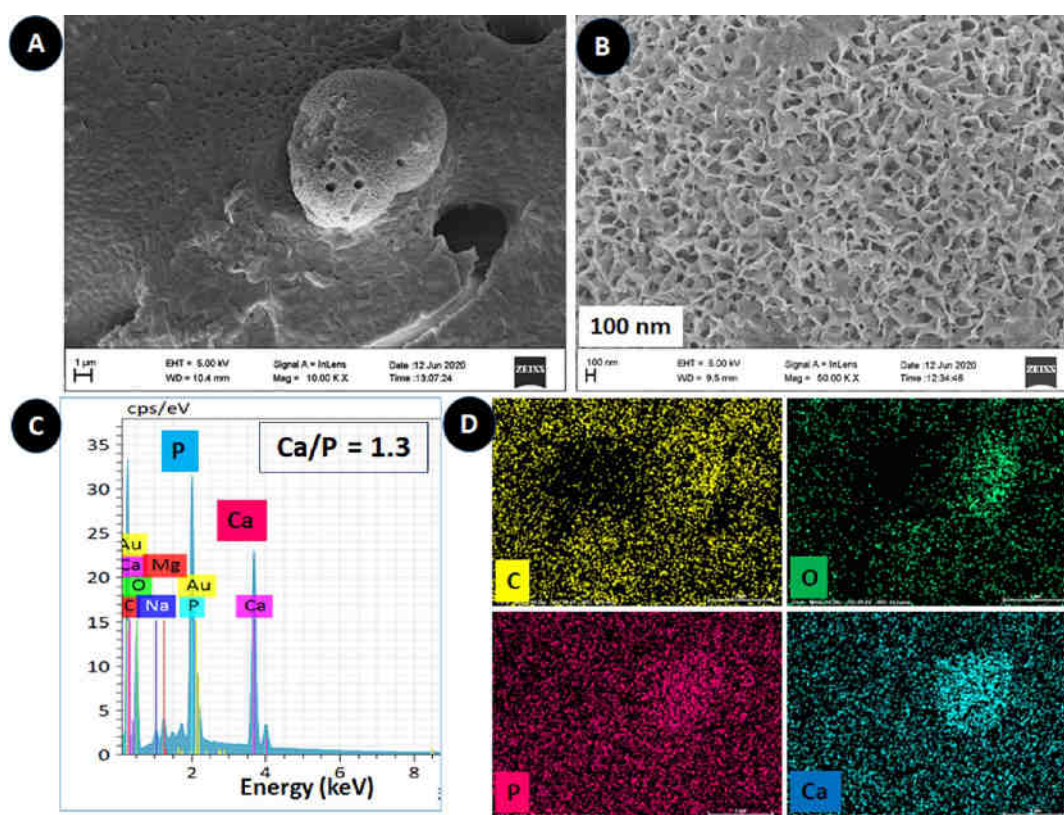
**Figure 13.** Proof of post-release biomimetic mineralization of scaffolds after sustained DOX release for 45 days. [(A,B) FESEM images depicting intense Ca-P coating (two different magnifications); (C,D) corresponding EDX spectrum and elemental mapping].

MG-63 cells, and cell viability was measured in terms of optical density of formazan crystals formed. As detailed in Figure 5E, the cell viability of P-PHM9163 resembles to that of untreated control cells ($p > 0.05$), while a decrease in viability was noticed for P-PHM8263 compared to the control ($p < 0.01$) after 24 h of incubation. However, a significant increase of cell viability in both the scaffolds was noticed on day 5 ($p < 0.001$) when compared with day 1 results; which adds better insights into the degree of cell proliferation as well. In addition, there were no statistically significant difference observed between the scaffolds and the control when the culture time increases (day 5). Figure 5F illustrates favorable cell−material interaction by the establishment of normal spindle-shaped regular morphology of the cells which can be attributed to the surface wettability of the scaffold.[54] These results, therefore, directly validate the cytocompatible nature of the scaffolds.

*2.3.4. P-PHM Scaffolds Induce Biomimetic Calcium Phosphate Mineralization.* Matrix mineralization is complementary during bone formation, where nucleation of calcium phosphate occurs in the form of hydroxyapatite (HAP), the inorganic phase of bone.[55,56] Therefore, biomimetic mineralization ability of the scaffolds in simulated physiological condition was assessed for 14 days. After incubation in SBF, the scaffolds were found to be decorated with assembly of nearly semispherical apatite crystals [Figure 6B(a−d)], while it was not visually evidenced in unmodified scaffolds [Figure 6A(a,b)]. Elemental analysis demonstrated time-dependent increase in Ca and P content (Figure 7B). The P-PHM8263 was found to have $0.54 \pm 0.37$ atomic % of Ca and $0.33 \pm 0.18$ atomic % of P on day 7 with a Ca/P ratio of 1.63 [Table 2]. On day 14, the Ca and P levels further increased to $10.25 \pm 1.35$ and $6.49 \pm 1.57$ atomic %, respectively, with Ca/P ratio 1.58 (Figure 7B(a) and Table 2). Similarly, for P-PHM9163, the Ca and P levels were amplified with increase in incubation time in SBF with a Ca/P ratio of 1.66 on day 14 (Table 2). Indeed, it depicts that phosphate coupling on the scaffolds induces early mineralization of apatite with the Ca/P ratio analogous to human bone (1.67) which underlines biomimetic mineralization

potential of the P-PHM matrix.[9] Interestingly, unmodified scaffolds have also induced apatite nucleation at a later phase (Figures 6A and 7A), though relatively lesser degree in comparison with P-PHM scaffolds and is attributed to Ca-ion binding capacity of −OH groups of poly(HEMA), but less affinity than phosphate groups.[57]

*2.3.5. P-PHM Scaffolds Induce Osteodifferentiation of rBMCs.* The rBMCs, potential osteoblast progenitors, were used to evaluate osteoblast differentiation ability of the scaffolds. The process of ossification is categorized into three major stages—proliferation, extracellular matrix mineralization, and its maturation.[58,59] The colonization of the cells was noticed on day 5 of culture and formed a layer at different locations on the scaffolds; providing a visual evidence for the cells' adhesion [Figure 8A($a_1,a^3$)]. Additionally, nucleation of calcium phosphate beginning on day 5 is authenticating early mineralization potential of the scaffolds [Figure 8A($a_2,a_4$)].

The cell-scaffold constructs were subjected to ARS and VK staining on day 14 of culture for evaluating biomineralization potential. Following the ARS staining, red spots corresponding to Ca deposition were abundant on the scaffolds (Figure 8B). Nonetheless, the staining intensity was higher for P-PHM9163 and P-PHM8263 than PHM9163 and PHM8263. This is fundamentally attributed to Ca-binding efficiency of negatively charged functional groups on the scaffolds ($PO_4^{3-}$ > −OH) which is well corroborated with *in vitro* biomimetic mineralization of these scaffolds in SBF (Figures 6 and 7). In consistent to this, VK staining (Figure 8C) also indicated more prominent brownish black mineral nodules in P-PHM scaffolds, indicating matrix mineralization.

Osteocalcin, a typical late marker indicating osteoblast formation, was quantified in cells grown on D-P-PHM9163 and D-P-PHM8263 on day 14 and day 21. The significant increase in its activity noticed on day 21 is a confirmative result substantiating osteoinduction, which is concurrent with previous reports.[58,59] Furthermore, the osteocalcin activity was significantly higher ($p < 0.001$) than untreated control (D-control) and comparable with respective positive controls (O-P-PHM9163 and O-P-PHM8263) (Figure 9). It clearly illustrates the

presence of matured osteoblast phenotype differentiated from rBMCs with accelerated mineral deposition. Altogether, higher calcium-binding capability of phosphorylated scaffolds enhanced intrinsic Ca-P mineralization potential rather earlier which led to a time-dependent sequential events of osteoblast formation.

*2.3.6. pH-Triggered Sustained Drug Release Profile of DOX-Loaded Bifunctional Scaffolds.* The P-PHM scaffolds (P-PHM9163 and P-PHM8263) were transformed to bifunctional (DOXP-PHM9163 and DOXP-PHM8263) by DOX (0.1 mg/mL) loading, intended for localized DOX delivery together with bone regeneration. The possible interaction of DOX with the scaffolds is mainly through electrostatic interaction [between primary amine of DOX's sugar moiety and phosphate group of scaffolds][60] (Figure 10A). The drug loading was estimated to 93.5 and 88.7% in P-PHM9163 and P-PHM8263, respectively. The increased DOX loading in P-PHM9163 is contributed by higher degree of phosphorylation, leading to greater interaction.

Further, cumulative release of DOX from DOXP-PHM9163 and DOXP-PHM8263, as a function of time, was evaluated in mildly acidic (PB; pH 6.5) and physiological pH (PBS; pH 7.34). As viewed from Figure 10B, DOX release from the scaffolds during initial hours at pH 6.5 (7.6% in DOXP-PHM9163; 5.4% in DOXP-PHM8263) is significantly higher than that at pH 7.34 (4% in DOXP-PHM9163; 3% in DOXP-PHM8263), indicating a pH-dependent release. Nearly two-fold increase in release noticed for PB compared to PBS at 1 h with a collective DOX release of 18% in DOXP-PHM9163 and 12% in DOXP-PHM8263 at 8 h. However, DOXP-PHM9163 has shown substantial upsurge in the release profile compared to DOXP-PHM8263 which might be attributed to its higher DOX loading capacity.

The release pattern for a prolonged time (Figure 10C) clearly depicts a pH-triggered DOX release. A remarkable difference was observed between day 1 and 10. On day 16, 84% of DOX was released from DOXP-PHM9163 at pH 6.5 and thereafter a slow pace of release noticed with a maximum of 96% on day 45, while it was only 63% (day 16) and 84% (day 45) at pH 7.34. Analogous trend has shown by DOXP-PHM8263 until day 16, and later on slower rate of release independent of pH was observed. Altogether, the DOX release rate was significantly lower at physiological pH during initial hours, but remarkably higher at mild acidic pH; which indeed would be a therapeutically favorable characteristic to support tumor-specific drug delivery as the interstitial extracellular pH of the tumor is mildly acidic (6.2–6.9) attributed to reverse pH gradient maintained by tumor cells.[37,38] The foremost mechanism is accredited to the tendency of DOX to remain in the protonated state ($pK_a$ = 8.2) under acidic environment which weakens the bonding between the scaffold and drug, leading to fast release of DOX to the surrounding medium.[61]

In addition to pH, other parameters such as microarchitecture, swelling behavior and degradation profile of the scaffold have pivotal role in dictating the drug release profile.[62] Hence, it is worth mentioning that the multisize of pores aids to accommodate more number of DOX molecules that diffuse to the medium after characteristic swelling of the scaffold. Moreover, controlled degradation (Figure 5D) and surface erosion in the scaffolds (Figure 10D) could also contribute to the sustained release of DOX for extended period to accomplish therapeutic success.

*2.3.7. DOX-Loaded Scaffolds Initiate Morphological Alterations in Actin Cytoskeleton and Nuclei of HOS Cells as a Cue of Cell Death.* We subsequently validated the effect of DOX released from DOXP-PHM9163 and DOXP-PHM8263 on HOS cells so as to ascertain the potential therapeutic efficacy of DOX-loaded scaffolds (Figure 11). DOX in the free form has already been stated to persuade cell death through initiation of various molecular signaling pathways which alter the normal cellular architecture including organization of F-actin cytoskeleton and nuclear fragmentation.[63,64] The untreated control cells were of spindle-shaped with a dense network of the F-actin cytoskeleton that configures its structural architecture. Additionally, these cells were characterized by nearly spherical-/oval-shaped intact nuclei. From Figure 11A,B, it is evident that the extracts of the DOXP-PHM scaffolds induced amendments in

the arrangements of actin stress fibers of cells by increasing the cortical actin stress fiber ring formation in a time-dependent manner which is absolutely absent in control (untreated) cells. In addition, the morphology of the cells was changed from spindle shape to more of a circular appearance following 48 h of treatment; precisely, it depicts that DOX-induced stress in the cells led to cell detachment and afterward cell death.[65] Further, the size of the nucleus is found as reduced significantly even at 24 h of the treatment with the extracts. Moreover, the number of cells with fragmented nuclei amplified upon exposure to the treatment for 48 h which has been reported as a hallmark of cell death by apoptosis.[66] Altogether, the number of giant cells depicting peripheral actin ring with multiple nuclei following the treatment has clearly illustrated the induction of cell death. These signs are found to be identical to free DOX-induced cellular alterations directing to apoptosis.[63,64]

The HOS cells were treated with DOXP-PHM9163 for 48 h, and the culture medium was collected at different time points. The pH of the medium was measured, and the data are presented as Figure S1. The cells incubated with DOXP-PHM9163 did not exhibit any significant variations in pH of the culture medium until 6 h, while a slight decrease in pH has observed at 24 and 48 h of incubation (Figure S1; not statistically significant) and is in accordance with the trend shown by the control (untreated) group. Hence, it is apparent that DOX release from the scaffold at early time points (up to 48 h) does not alter pH of the tumor cell microenvironment (*in vitro*). Further, SEM images of the scaffold after DOX release for 48 h imparted clear evidences for retention of its porous microarchitecture (Figure S2). However, surface crevices were observed in the scaffolds (Figure S2) that might be contributed by the sudden dehydration during the drying process of the scaffold, after complete swelling for 48 h in the culture medium.

*2.3.8. DOXP-PHM Scaffold Induces Apoptosis in HOS Cells.* The signs of apoptosis evidenced from delocalization of the actin cytoskeleton and fragmented nuclei were further confirmed by annexin V/PI dual staining (Figure 12). Annexin V is a phospholipid-binding protein that possesses higher attraction toward phosphatidyl serine which is exposed on the outer cell membrane, instead of inner membrane, during apoptosis.[67,68] Therefore, annexin V positive cells are suggestive of cell death by the apoptotic mechanism. In the untreated control group, 96.3% of cells were annexin $V^-/PI^-$, indicating viable cells, while remaining 3.7% of cells were in the early apoptotic stage. However, the DOXP-PHM9163 group has exhibited 82.4% of early apoptotic cells (annexin $V^+/PI^-$), 17.4% of viable cells (annexin $V^-/PI^-$) and 0.2% of late apoptotic cells (annexin $V^+/PI^+$). There were no signs of annexin $V^-/PI^+$ cells identified, suggesting absence of necrosis. It has been evidenced that majority of the cells initiated apoptosis and moving to complete cell death (late apoptosis), illustrating apoptosis as the underlying mechanism of cell death.

*2.3.9. DOXP-PHM9163 Stimulates "Post-DOX Release" Biomimetic Mineralization in Simulated Blood Plasma Ionic Condition.* After successful localized DOX release extended for 45 days into slightly acidic tumor pH, the scaffold—DOXP-PHM9163—has been retrieved and immersed in SBF for 14 days. It is obvious from FESEM images that decorative layer of organized porous apatite well spread over the scaffold (Figure 13A). In addition, the mineralized nodules exhibited well-organized interlinked array of nanosized pores which might contribute to an increase in surface area (Figure 13B). Consequently, it favors the attachment of bone—specific proteins and thereby expedites cell adhesion and bone formation.[69] Moreover, the surface roughness of the scaffold verified following sustained DOX release (Figure 10D) might be a complementary condition in augmenting mineralization. The EDX analysis (Ca/P 1.3) and elemental mapping have provided substantial evidence for Ca-P mineralization potential of the post-release scaffold (Figure 13C,D). Overall, the results precisely depict the second functionality of the scaffold (osteogenesis) even after the efficacious completion of its initial phase of dual functionality (DOX release).

## 3. CONCLUSIONS

Smart bifunctional 3D scaffolds developed through innovative approaches would triumph over clinical challenges of osteosarcoma treatment by simultaneous tumor therapy and bone regeneration. The bifunctional copolymer therapeutic scaffold developed in this study presents a comprehensive therapeutic approach for osteosarcoma and performs two active roles. Surface-phosphorylated hierarchically porous hydrophilic scaffolds with ideal load-bearing capacity mimicking host-tissue microenvironment primarily operate as a favorable matrix for osteoblast differentiation from progenitor cells through cell proliferation and matrix biomineralization [inherent bone formation]. The surface-phosphorylated micro-porous structure also facilitates encapsulation of doxorubicin and enabling its pH-responsive sustained release in mildly acidic medium resembling tumor extracellular microenviron-ment and induces apoptosis of HOS cells by establishing drug delivery and thereby tumor cell annihilation. Most importantly, the induction of biomimetic mineralization successive to sustained DOX-release emphasizes its functionality as a bifaceted treatment system for osteosarcoma. Hence, the scaffold presented would be a promising therapeutic strategy against osteosarcoma by the localized drug delivery and the induction of bone regeneration.

## ◼ ASSOCIATED CONTENT

### Ⓢ Supporting Information

The Supporting Information is available free of charge at https://pubs.acs.org/doi/10.1021/acsbiomaterials.0c01628.

> Time-dependent DOX-induced pH changes in HOS cell culture microenvironment; Microarchitecture of the bifunctional scaffold—DOXP-PHM9163 after DOX release for 48 h in HOS cell culture medium (PDF)

## ◼ AUTHOR INFORMATION

### Corresponding Author

G. S. Sailaja − *Department of Polymer Science and Rubber Technology and Centre for Excellence in Advanced Materials, Cochin University of Science and Technology, Kochi, Kerala 682 022, India; Inter University Centre for Nanomaterials and Devices (IUCND), Cochin University of Science and Technology, Kochi, Kerala 682 022, India;* ⓘ orcid.org/0000-0002-6406-7293; Phone: +91-9744799643; Email: sailajags@cusat.ac.in

### Authors

S. Sreeja − *Department of Polymer Science and Rubber Technology, Cochin University of Science and Technology, Kochi, Kerala 682 022, India*

Ramesh Parameshwar − *Division of Polymeric Medical Devices, Biomedical Technology Wing, Sree Chitra Tirunal Institute for Medical Sciences and Technology, Thiruvananthapuram 695 011, India*

P. R. Harikrishna Varma − *Head of Biomedical Technology Wing, Sree Chitra Tirunal Institute for Medical Sciences and Technology, Thiruvananthapuram 695 011, India;* ⓘ orcid.org/0000-0002-0369-1690

Complete contact information is available at:
https://pubs.acs.org/10.1021/acsbiomaterials.0c01628

### Author Contributions

S.S. has performed the experiment, analyzed the data, and written the manuscript. G.S.S. has conceived the idea, supervised the work in timely manner, and edited the manuscript. R.P. and P.R.H.V. have also edited the manuscript and provided overall guidance for the successful completion of this work.

### Notes

The authors declare no competing financial interest.

## ◼ ACKNOWLEDGMENTS

## ◼ ABBREVIATIONS

PHM, poly(HEMA-*co*-MMA); P-PHM, phosphorylated poly-(HEMA-*co*-MMA); DOX, doxorubicin; rBMCs, rat bone marrow mesenchymal cells; SBF, simulated body fluid; PI, propidium iodide

## ◼ REFERENCES

(1) Mirabello, L.; Troisi, R. J.; Savage, S. A. International osteosarcoma incidence patterns in children and adolescents, middle ages and elderly persons. *Int. J. Cancer* **2009**, *125*, 229−234.

(2) Wang, S.-Y.; Hu, H.-Z.; Qing, X.-C.; Zhang, Z.-C.; Shao, Z.-W. Recent advances of drug delivery nanocarriers in osteosarcoma treatment. *J. Cancer* **2020**, *11*, 69−82.

(3) Isakoff, M. S.; Bielack, S. S.; Meltzer, P.; Gorlick, R. Osteosarcoma: current treatment and a collaborative pathway to success. *J. Clin. Oncol.* **2015**, *33*, 3029−3035.

(4) Luetke, A.; Meyers, P. A.; Lewis, I.; Juergens, H. Osteosarcoma treatment − Where do we stand? A state of the art review. *Canc. Treat Rev.* **2013**, *40*, 523−532.

(5) Carvalho, F. S.; Burgeiro, A.; Garcia, R.; Moreno, A. J.; Carvalho, R. A.; Oliveira, P. J. Doxorubicin-induced cardiotoxicity : from bioenergetic failure and cell death to cardiomyopathy. *Med. Res. Rev.* **2014**, *34*, 106−135.

(6) Wu, C.; Luo, Y.; Cuniberti, G.; Xiao, Y.; Gelinsky, M. Three-dimensional printing of hierarchical and tough mesoporous bioactive glass scaffolds with a controllable pore architecture, excellent mechanical strength and mineralization ability. *Acta Biomater.* **2011**, *7*, 2644−2650.

(7) Torres, A. L.; Gaspar, V. M.; Serra, I. R.; Diogo, G. S.; Fradique, R.; Silva, A. P.; Correia, I. J. Bioactive polymeric − ceramic hybrid 3D scaffold for application in bone tissue regeneration. *Mater. Sci. Eng., C* **2013**, *33*, 4460−4469.

(8) Yao, Q.; Fuglsby, K. E.; Zheng, X.; Sun, H. Nanoclay-functionalized 3D nanofibrous scaffolds promote bone regeneration. *J. Mater. Chem. B* **2020**, *8*, 3842−3851.

(9) Rezwan, K.; Chen, Q. Z.; Blaker, J. J.; Boccaccini, A. R. Biodegradable and bioactive porous polymer/inorganic composite scaffolds for bone tissue engineering. *Biomaterials* **2006**, *27*, 3413−3431.

(10) Thein-Han, W. W.; Misra, R. D. K. Biomimetic chitosan–nanohydroxyapatite composite scaffolds for bone tissue engineering. *Acta Biomater.* **2008**, *5*, 1182−1197.

(11) Xu, M.; Li, H.; Zhai, D.; Chang, J.; Chen, S.; Wu, C. Hierarchically porous nagelschmidtite bioceramic − silk scaffolds for bone tissue. *J. Mater. Chem. B* **2015**, *3*, 3799−3809.

(12) Gu, W.; Wu, C.; Chen, J.; Xiao, Y. Nanotechnology in the targeted drug delivery for bone diseases and bone regeneration. *Int. J. Nanomed.* **2013**, *8*, 2305−2317.

(13) Salerno, M.; Cenni, E.; Fotia, C.; Avnet, S.; Granchi, D.; Castelli, F.; Micieli, D.; Pignatello, R.; Capulli, M.; Rucci, N.; Angelucci, A.; Del Fattore, A.; Teti, A.; Zini, N.; Giunti, A.; Baldini, N. Bone-targeted doxorubicin-loaded nanoparticles as a tool for the treatment of skeletal metastases. *Curr. Cancer Drug Targets* **2010**, *10*, 649−659.

(14) Sarigol-Calamak, E.; Hascicek, C. Tissue scaffolds as a local drug delivery system for bone regeneration. In *Cutting-Edge Enabling Technologies for Regenerative Medicine, Advances in Experimental Medicine and Biology*; Chun, H. J., Park, C., Kwon, I., Khang, G., Eds.; Springer: Singapore, 2018; pp 475−492.

(15) Palamà, I. E.; Arcadio, V.; D'Amone, S.; Biasiucci, M.; Gigli, G.; Cortese, B. Therapeutic PCL scaffold for reparation of resected osteosarcoma defect. *Sci. Rep.* **2017**, *7*, 12672.

(16) Sun, M.; Wang, M.; Chen, M.; Dagnaes-hansen, F.; Le, D. Q. S.; Baatrup, A.; Horsman, M. R.; Kjems, J.; Bünger, C. E. A tissue-engineered therapeutic device inhibits tumor growth in vitro and in vivo. *Acta Biomater.* **2015**, *18*, 21−29.

(17) Yang, F.; Lu, J.; Ke, Q.; Peng, X.; Guo, Y.; Xie, X. Magnetic mesoporous calcium sillicate/chitosan porous scaffolds for enhanced bone regeneration and photothermal-chemotherapy of osteosarcoma. *Sci. Rep.* **2018**, *8*, 7345.

(18) Kemal, E.; Adesanya, K. O.; Deb, S. Phosphate based 2-hydroxyethyl methacrylate hydrogels for biomedical applications. *J. Mater. Chem.* **2011**, *21*, 2237−2245.

(19) Çetin, D.; Kahraman, A. S.; Gümüşderelioğlu, M. Novel scaffolds based on poly (2- hydroxyethyl methacrylate) superporous hydrogels for bone tissue engineering. *J. Biomater. Sci., Polym. Ed.* **2011**, *22*, 1157−1178.

(20) Nielsen, S. U.; Olsen, M. H.; Kongsfelt, M. S.; Pedersen, S. U.; Daasbjerg, K. Hydrosilane-modified poly(2-hydroxyethyl methacrylate) brush as a nanoadhesive for efficient silicone bonding. *ACS Omega* **2019**, *4*, 12130−12135.

(21) Atzet, S.; Curtin, S.; Trinh, P.; Bryant, S.; Ratner, B. Degradable poly (2-hydroxyethyl methacrylate) - co -polycaprolactone hydrogels for tissue engineering scaffolds. *Biomacromolecules* **2008**, *9*, 3370−3377.

(22) Moghadam, M. N.; Pioletti, D. P. Biodegradable HEMA-based hydrogels with enhanced mechanical properties. *J. Biomed. Mater. Res. B.* **2015**, *104*, 1161−1169.

(23) Sailaja, G. S.; Kumari, T. V.; Yokogawa, Y.; Varma, H. K. In vitro mineralization and cell adhesion on surface modified poly (2 - hydroxyethyl methacrylate-co-methyl methacrylate). *Key Eng. Mater.* **2009**, *309−311*, 493−496.

(24) Sailaja, G. S.; Ramesh, P.; Varma, H. Effect of surface functionalization on the physicomechanical properties of a novel biofunctional copolymer. *J. Appl. Polym. Sci.* **2011**, *121*, 3509−3515.

(25) Gopalakrishnanchettiyar, S. S.; Mohanty, M.; Kumary, T. V.; Valappil, M. P.; Parameshwaran, R.; Varma, H. K. Surface-phosphorylated copolymer promotes direct bone bonding. *Tissue Eng., Part A* **2009**, *15*, 3061−3069.

(26) Hu, Y.; Grainger, D. W.; Winn, S. R.; Hollinger, J. O. Fabrication of poly (α-hydroxy acid) foam scaffolds using multiple solvent systems. *J. Biomed. Mater. Res.* **2001**, *59*, 563−572.

(27) Sailaja, G. S.; Ramesh, P.; Varma, H. K. Swelling behavior of hydroxyapatite-filled chitosan-poly(acrylic acid) polyelectrolyte complexes. *J. Appl. Polym. Sci.* **2006**, *100*, 4716−4722.

(28) Younes, H. M.; Bravo-Grimaldo, E.; Amsden, B. G. Synthesis, characterization and in vitro degradation of a biodegradable elastomer. *Biomaterials* **2004**, *25*, 5261−5269.

(29) Sreeja, S.; Muraleedharan, C. V.; Varma, P. R. H.; Sailaja, G. S. Surface-transformed osteoinductive polyethylene terephthalate scaffold as a dual system for bone tissue regeneration with localized antibiotic delivery. *Mater. Sci. Eng., C* **2020**, *109*, 110491.

(30) Ko, E. K.; Jeong, S. I.; Rim, N. G.; Lee, Y. M.; Shin, H.; Lee, B.-K. In vitro osteogenic differentiation of human mesenchymal stem cells and in vivo bone formation in composite nanofiber meshes. *Tissue Eng., Part A* **2008**, *14*, 2105−2119.

(31) Kokubo, T.; Takadama, H. How useful is SBF in predicting in vivo bone bioactivity? *Biomaterials* **2006**, *27*, 2907−2915.

(32) Lee, J. T. Y.; Chow, K. L. SEM sample preparation for cells on 3D scaffolds by freeze-drying and HMDS. *Scanning* **2012**, *34*, 12−25.

(33) Gregory, C. A.; Grady Gunn, W.; Peister, A.; Prockop, D. J. An alizarin red-based assay of mineralization by adherent cells in culture: Comparison with cetylpyridinium chloride extraction. *Anal. Biochem.* **2004**, *329*, 77−84.

(34) Nourmohammadi, J.; Roshanfar, F.; Farokhi, M.; Haghbin Nazarpak, M. Silk fibroin/kappa-carrageenan composite scaffolds with enhanced biomimetic mineralization for bone regeneration applications. *Mater. Sci. Eng., C* **2017**, *76*, 951−958.

(35) Lee, J. H.; Rhie, J. W.; Oh, D. Y.; Ahn, S. T. Osteogenic differentiation of human adipose tissue-derived stromal cells (HASCS) in a porous three-dimensional scaffold. *Biochem. Biophys. Res. Commun.* **2008**, *370*, 456−460.

(36) Lowry, O. H.; Rosebrough, N. J.; Farr, A. L.; Randall, R. J. Protein measurement with the folin phenol reagent. *J. Biol. Chem.* **1951**, *193*, 265−275.

(37) Cardone, R. A.; Casavola, V.; Reshkin, S. J. The role of disturbed pH dynamics and the Na+/H+ exchanger in metastasis. *Nat. Rev. Cancer* **2005**, *5*, 786−795.

(38) White, K. A.; Grillo-Hill, B. K.; Barber, D. L. Cancer cell behaviors mediated by dysregulated pH dynamics at a glance. *J. Cell Sci.* **2017**, *130*, 663−669.

(39) Su, G.; Zhou, T.; Liu, X.; Ma, Y. Micro-dynamics mechanism of the phase transition behavior of poly (N -isopropylacrylamide- co -2-hydroxyethyl methacrylate) hydrogels revealed by two-dimensional correlation spectroscopy. *Polym. Chem.* **2017**, *8*, 865−878.

(40) Siddiqui, M. N.; Redhwi, H. H.; Tsagkalias, I.; Softas, C.; Ioannidou, M. D.; Achilias, D. S. Synthesis and characterization of poly(2-hydroxyethyl methacrylate)/silver hydrogel nanocomposites prepared via in situ radical polymerization. *Thermochim. Acta* **2016**, *643*, 53−64.

(41) Lee, B.-S.; Chen, Y.-J.; Wei, T.-C.; Ma, T.-L.; Chang, C.-C. Comparison of antibacterial adhesion when salivary pellicle is coated on both poly(2-hydroxyethyl-methacrylate)-and polyethylene-glycol-methacrylate-grafted poly(methyl methacrylate). *Int. J. Mol. Sci.* **2018**, *19*, 2764−2782.

(42) Islam, M. R.; Bach, L. G.; Park, J. M.; Hong, S.-S.; Lim, K. T. Synthesis and characterization of poly(HEMA-co-MMA)-g-POSS nanocomposites by combination of reversible addition fragmentation chain transfer polymerization and click chemistry. *J. Appl. Polym. Sci.* **2013**, *127*, 1569−1577.

(43) Arai, Y.; Sparks, D. L. ATR-FTIR spectroscopic investigation on phosphate adsorption mechanisms at the ferrihydrite-water interface. *J. Colloid Interface Sci.* **2001**, *241*, 317−326.

(44) De Giglio, E.; Cometa, S.; Ricci, M. A.; Zizzi, A.; Cafagna, D.; Manzotti, S.; Sabbatini, L.; Mattioli-Belmonte, M. Development and characterization of rhVEGF-loaded poly(HEMA-MOEP) coatings electrosynthesized on titanium to enhance bone mineralization and angiogenesis. *Acta Biomater.* **2010**, *6*, 282−290.

(45) Loh, Q. L.; Choong, C. Three-dimensional scaffolds for tissue engineering applications. *Tissue Eng., Part B* **2013**, *19*, 485−502.

(46) De Witte, T.-M.; Fratila-apachitei, L. E.; Zadpoor, A. A.; Peppas, N. A. Bone tissue engineering via growth factor delivery: from scaffolds to complex matrices. *Regener. Biomater.* **2018**, *5*, 197−211.

(47) Karageorgiou, V.; Kaplan, D. Porosity of 3D biomaterial scaffolds and osteogenesis. *Biomaterials* **2005**, *26*, 5474−5491.

(48) Li, X.; van Blitterswijk, C. A.; Feng, Q.; Cui, F.; Watari, F. The Effect of Calcium Phosphate Microstructure on Bone-Related Cells in Vitro. *Biomaterials* **2008**, *29*, 3306−3316.

(49) Sherwood, J. K.; Riley, S. L.; Palazzolo, R.; Brown, S. C.; Monkhouse, D. C.; Coates, M.; Griffith, L. G.; Landeen, L. K.; Ratcliffe, A. A three-dimensional osteochondral composite scaffold for articular cartilage repair. *Biomaterials* **2002**, *23*, 4739−4751.

(50) Gerhardt, L.-C.; Boccaccini, A. R. Bioactive glass and glass-ceramic scaffolds for bone tissue engineering. *Materials* **2010**, *3*, 3867−3910.

(51) Levengood, S. K. L.; Zhang, M. Chitosan-based scaffolds for bone tissue engineering. *J. Mater. Chem. B* **2014**, *2*, 3161−3184.

(52) Tao, L.; Zhonglong, L.; Ming, X.; Zezheng, Y.; Zhiyuan, L.; Xiaojun, Z.; Jinwu, W. In vitro and in vivo studies of a gelatin/carboxymethyl chitosan/LAPONITE composite scaffold for bone tissue engineering. *RSC Adv.* **2017**, *7*, 54100−54110.

(53) Huhtamäki, T.; Tian, X.; Korhonen, J. T.; Ras, R. H. A. Surface-wetting characterization using contact-angle measurements. *Nat. Protoc.* **2018**, *13*, 1521−1538.

(54) Bodhak, S.; Bose, S.; Bandyopadhyay, A. Role of Surface Charge and Wettability on Early Stage Mineralization and Bone Cell − Materials Interactions of Polarized Hydroxyapatite. *Acta Biomater.* **2009**, *5*, 2178−2188.

(55) Tanahashi, M.; Matsuda, T. Surface functional group dependence on apatite formation on self- assembled monolayers in a simulated body fluid. *J. Biomed. Mater. Res.* **1997**, *34*, 305−315.

(56) Sailaja, G. S.; Ramesh, P.; Vellappally, S.; Anil, S.; Varma, H. K. Biomimetic approaches with smart interfaces for bone regeneration. *J. Biomed. Sci.* **2016**, *23*, 77.

(57) Wang, X.; Ma, J.; Wang, Y.; He, B. Structural characterization of phosphorylated chitosan and their applications as effective additives of calcium phosphate cements. *Biomaterials* **2001**, *22*, 2247−2255.

(58) Hanna, H.; Mir, L. M.; Andre, F. M. In vitro osteoblastic differentiation of mesenchymal stem cells generates cell layers with distinct properties. *Stem Cell Res. Ther.* **2018**, *9*, 203.

(59) Majors, A. K.; Boehm, C. A.; Nitto, H.; Midura, R. J.; Muschler, G. F. Characterization of human bone marrow stromal cells with respect to osteoblastic differentiation. *J. Orthop. Res.* **1997**, *15*, 546−557.

(60) Prokopowicz, M. In-vitro controlled release of doxorubicin from silica xerogels. *J. Pharm. Pharmacol.* **2007**, *59*, 1365−1373.

(61) Dadsetan, M.; Taylor, K. E.; Yong, C.; Bajzer, Ž.; Lu, L.; Yaszemski, M. J. Controlled release of doxorubicin from pH-responsive microgels. *Acta Biomater.* **2013**, *9*, 5438−5446.

(62) Cyphert, E. L.; Bil, M.; Recum, H. A.; Święszkowski, W. Repurposing Biodegradable Tissue Engineering Scaffolds for Localized Chemotherapeutic Delivery. *J. Biomed. Mater. Res., Part A* **2020**, *108*, 1144.

(63) Colombo, R.; Necco, A.; Vailati, G.; Milzani, A. Dose-dependence of doxorubicin effect on actin assembly in vitro. *Exp. Mol. Pathol.* **1988**, *49*, 297−304.

(64) Wang, S.; Konorev, E. A.; Kotamraju, S.; Joseph, J.; Kalivendi, S.; Kalyanaraman, B. Doxorubicin induces apoptosis in normal and tumor cells via distinctly different mechanisms. Intermediacy of H(2)O(2)- and p53-dependent pathways. *J. Biol. Chem.* **2004**, *279*, 25535−25543.

(65) Wei, L.; Surma, M.; Gough, G.; Shi, S.; Lambert-Cheatham, N.; Chang, J.; Shi, J. Dissecting the mechanisms of doxorubicin and oxidative stress-induced cytotoxicity: The involvement of actin cytoskeleton and ROCK1. *PLoS One* **2015**, *10*, No. e0131763.

(66) Grzanka, D.; Grzanka, A.; Izdebska, M.; Gackowska, L.; Stepien, A.; Marszalek, A. Actin reorganization in CHO AA8 cells undergoing mitotic catastrophe and apoptosis induced by doxorubicin. *Oncol. Rep.* **2010**, *23*, 655−663.

(67) Lu, X.; Qian, J.; Zhou, H.; Gan, Q.; Tang, W.; Lu, J.; Yuan, Y.; Liu, C. In vitro cytotoxicisty and induction of apoptosis by silica nanoparticles in human HepG2 hepatoma cells. *Int. J. Nanomed.* **2011**, *6*, 1889−1901.

(68) Krysko, D. V.; Berghe, T. V.; Parthoens, E.; D'Herde, K.; Vandenabeele, P. Methods for distinguishing apoptotic from necrotic cells and measuring their clearance. *Methods Enzymol.* **2008**, *442*, 307−341.

(69) Wang, S.; Kowal, T. J.; Marei, M. K.; Falk, M. M.; Jain, H. Nanoporosity significantly enhances the biological performance of engineered glass tissue scaffolds. *Tissue Engineering Part A* **2013**, *19*, 1632−1640.
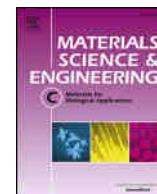
# Surface-transformed osteoinductive polyethylene terephthalate scaffold as a dual system for bone tissue regeneration with localized antibiotic delivery

S. Sreeja[a], C.V. Muraleedharan[b], P.R. Harikrishna Varma[c], G.S. Sailaja[a,d,e,*]

[a] *Department of Polymer Science and Rubber Technology, Cochin University of Science and Technology, Kerala 682 022, India*
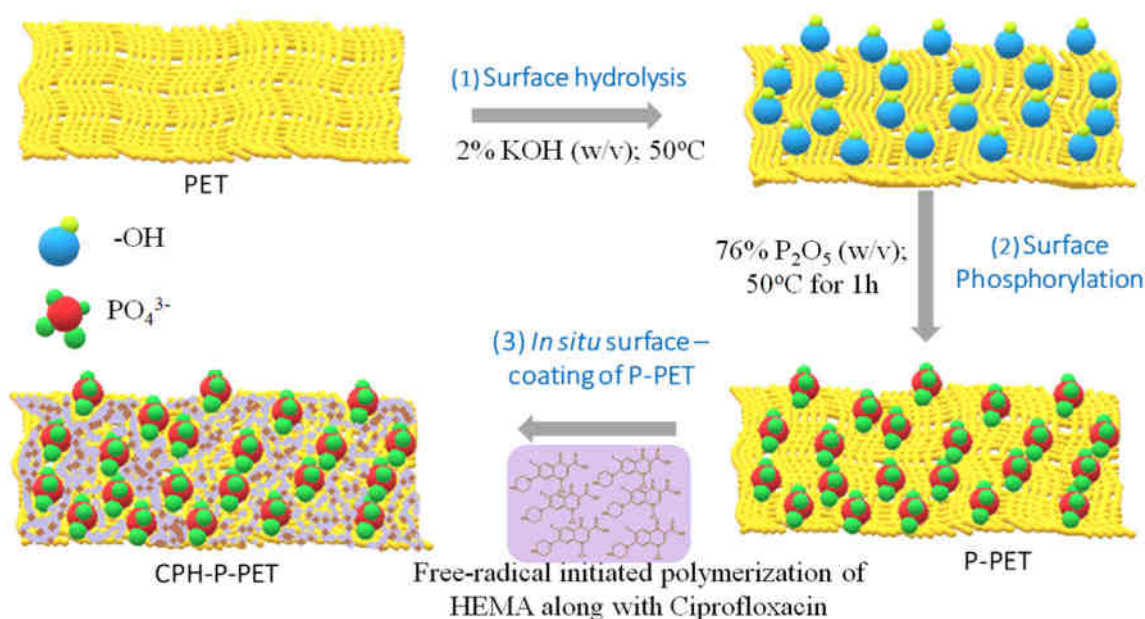[b] *Division of Artificial Internal Organs, Biomedical Technology Wing, Sree Chitra Tirunal Institute for Medical Sciences and Technology, Thiruvananthapuram, Kerala 695 012, India*
[c] *Head, Biomedical Technology Wing, Sree Chitra Tirunal Institute for Medical Sciences and Technology, Thiruvananthapuram, Kerala 695 012, India*
[d] *Inter University Centre for Nanomaterials and Devices (IUCND), Kerala 682 022, India*
[e] *Centre for Excellence in Advanced Materials, Cochin University of Science and Technology, Kerala 682 022, India*

## ARTICLE INFO

## ABSTRACT

Multifunctional scaffolds have recently attained superior significance in tissue regeneration due to combinational activity profile that is usually accomplished by separate sequential therapy. Here, we present a dual system comprised of surface-phosphorylated PET fibrous matrix coated with ciprofloxacin-impregnated biodegradable polymer poly (hydroxyethyl methacrylate) aiming at regeneration of bone tissue deprived of bacterial infections, particularly osteomyelitis. The ATR, XPS and FESEM/EDX results provided confirmative evidences for surface phosphorylation of PET and *in situ* coating of the polymer. Swelling and contact angle measurements demonstrated improved hydrophilicity which is further corroborated by *in vitro* degradation profile in PBS. Preliminary evaluation by MTT and actin staining proved its biocompatibility while enhanced *in vitro* mineralization in 1.5X SBF by FESEM/EDX clearly indicate the primary nucleation and secondary growth of beautiful apatite crystals with Ca/P ratio similar to human bone. Alizarin red S and von Kossa staining validated the biomineralization in MG-63 cells. The sequential expression of early and late biomarkers -alkaline phosphatase (ALP) and osteocalcin (OSN)- of osteoblast differentiation in rat bone marrow mesenchymal cells (BMC) has demonstrated osteoinductive nature of the system. The second functionality of the scaffold has been proven by step-wise ciprofloxacin-release profile (*in vitro*) with ~60% release within 120 h. In addition, antibacterial studies of ciprofloxacin- eluted from the scaffold have shown apparent zones of inhibition against *Staphylococcus aureus* (3.6 ± 0.3 cm) and *Escherichia coli* (3.0 ± 0.8 cm). Hence, the surface-transformed PET scaffold function as a dual system as localized antibiotic delivery vehicle against bone infections and undergo self-biomineralization leading to osteoinduction.

## 1. Introduction

Bone defects originate by trauma or diseases, which does rectify by self – repair mechanism of bone, impose a high demand for bone substitutes to aid its effective regeneration. Autologous bone, the gold standard though possess all prerequisites for the regeneration of the bone, is of highly limited use due to donor site inflammations and morbidity which presents an imperative urge for synthetic bone grafts. In order to address bone degeneration, a wide spectrum of biomaterials as well as bone marrow mesenchymal stem cell based therapeutic system are explored for the repair and regeneration of bone defects through successive integration into the host tissue [1–3]. In this regard, prompt attention has also made to engineer surface-functionalized bone grafts to offer necessary support to augment bone cell formation and its differentiation [4–7]. An ideal biomaterial harbour by itself as a template for bone tissue regeneration and possess excellent biocompatibility and well-disciplined biodegradation profile along with identical micro-texture and mechanical properties of host bone [8]. Several natural and synthetic materials have been explored to rectify bone damages through its regeneration [9–11].

In spite of numerous developments in orthopaedic implantation, infections are still a major concern. Infections could be initiated by

**Scheme 1.** Fabrication of dual functioning CPH-P-PET system.

different ways including orthopaedic implant – associated, systemic and blood-borne infections [12]. At times it leads to complete failure of the implant due to osteomyelitis, a severe bone infection caused mainly by *Staphylococcus aureus*, as most of the bacterial strains have the ability to form biofilms at biograft-tissue interfaces as well as on medical devices [13,14]. Due to the complexity of the disease, it is often highly difficult to diagnose and provide adequate treatment. Hence, the therapy could be designed according to the virulence state of bacteria and mechanism of infection [12,15]. Surgical debridement together with prolonged antibiotic therapy are the widely accepted treatment strategies. However, the orthodox systemic administration of antibiotics causes reduction in its bioavailability in the desired area. Moreover, the use of antibiotics for long period of time causes several systemic complications along with antibiotic resistance [16]. To address this problem, a thorough knowledge on pathophysiology of the infection is highly recommended. The mechanism of action of bacteria mainly facilitates through biofilm formation on the devices. Additionally, these biofilms shield the infectious organisms from antimicrobial agents. Therefore, it is inevitable to inhibit initial adherence of bacteria to the biomaterial surface. Generally, initial period of post-surgery is more prone to initiation and progression of major infections. Hence, it is ideal to customize a bone graft with antibacterial activity [17,18]. Antibiotics – loaded poly (methylmethacrylate) (PMMA) beads have been widely applied in the clinical settings as a local antibiotic delivery system against osteomyelitis. However, a second surgical intervention is required to remove the PMMA beads from the site after the antibiotic release [16,19,20]. This is to be followed by therapeutic steps for the regeneration of lost bone. Hence, an effective local antibiotic delivery system having both osteoinductive potential and controlled antibiotic delivery is of greatly in demand to circumvent both infection and preserve the structural integrity of the bone [21–23].

Numerous biocompatible systems have been designed to compete with bone infections. These include antibiotic delivery systems with sustained or controlled release properties as well as dual functional system for site-specific antibiotic release and osteoinduction [24–26]. Furthermore, a number of synthetic slow degrading polymeric materials at physiological pH are designed which lead to the sustained release of antibiotics. However, the clinical application of many antimicrobial bone grafts are found to be inconclusive as some of the graft modifications alter the physical properties of the antibiotic, at the same time, mechanical property of the material [27,28].

Polyethylene terephthalate (PET) has been clinically accepted as an artificial vascular prosthesis because of its excellent mechanical and physical properties [29,30]. PET is basically bio-inert in nature. Surface coating of PET fibres with bioactive materials has been tried and found as effective for artificial ligament grafting and thereby bone bonding [31–34]. However, the long-term functionality of these materials is not successful. Moreover, no study has been reported so far based on PET fibrous matrix to address bone infections. Several different approaches such as enzymatic modification, gamma irradiation, surface ionization by corona discharge and localized alterations using argon plasma jet at atmospheric pressure have been reported for surface functionalization of PET for various applications [35–38]. In the present study, we have focused on this aspect through surface-transformation of PET by surface-phosphorylation to invoke bone regeneration similar to other polymer matrices reported earlier [39,40]. Further, it is transformed to a dual functioning system with added potential of bone regeneration and antibiotic delivery to overcome the aforementioned challenges associated with bone infections. The physicochemical properties and biofunctional assays were performed to evaluate the efficacy of the designed dual functional system.

## 2. Materials and methods

### 2.1. Fabrication of surface-transformed PET

The virgin PET fibrous matrix was prepared by wet spinning of its fibres with water permeability of $200 \pm 100$ mL/cm$^2$ and ultrasonically cleaned with nitrogen purged ultrapure water (18.2 MΩ.cm at 25 °C) and dried under vacuum at 50 °C for overnight prior to surface modification. PET matrix was initially surface hydrolyzed by 2 wt% ($w/v$) KOH at 50 °C for 1 h and washed until neutral pH. Subsequently, hydrolyzed samples were surface phosphorylated using 76 wt% (w/v) P$_2$O$_5$ (Sigma Aldrich, India) [41]. The surface-phosphorylated PET (P-PET) serve as a positive control in the bone regeneration studies. The dual system has been fabricated by post-processing of P-PET by *in situ* free radical-initiated polymerization of hydroxyethyl methacrylate (HEMA) (Merck Millipore, USA) loaded with 1 mg/mL of antibiotic ciprofloxacin (CPH-P-PET), illustrated as Scheme 1. The polymerization reaction was carried out using benzoyl peroxide (Merck Millipore, USA) as initiator at 80 °C. The CPH-P-PET was kept at 80 °C for the completion of polymerization. The poly(HEMA) (without ciprofloxacin)

coated P-PET scaffolds, PH-P-PET, sterilized by ethylene oxide (ETO) sterilization method were used for cell culture experiments.

## 2.2. Physicochemical characterization of the scaffolds

The surface-phosphorylation was primarily analyzed by ATR spectroscopy (PerklinElmer Specac, UK) in reflectance mode in the range of $4000 \, cm^{-1}$ to $500 \, cm^{-1}$. Surface phosphorylation was confirmed by X-ray photoelectron spectroscopy (XPS) (Thermo Fischer Scientific ESCALAB Xi+, India) using monochromatic Al-Ka X-ray and binding energies of the elements (C1s, O1s and P2p) were autoshift-scaled to the spectra of C1s (284 eV). ATR spectroscopy further confirmed the surface coating of ciprofloxacin-impregnated poly (HEMA) onto P-PET and thereby formation of dual system CPH-P-PET. The surface texture of bare PET, P-PET and CPH-P-PET were harvested with Field Emission Scanning Electron Microscopy (Carl Zeiss Sigma, Germany). All the samples were gold sputtered (Jeol JFC-1600 Autofine coater, Japan) prior to surface scanning. Elemental analysis and mapping (three different locations) of PET, P-PET and CPH-P-PET performed with Energy Dispersive X-ray analyzer (EDX) (XFlash 6I100 Bruker, USA) were used for further confirmation of surface phosphorylation. The porosity of the scaffolds (P-PET and CPH-P-PET) was measured by liquid intrusion method by immersing the scaffolds in ethanol [42,43]. X-ray diffraction analysis has been performed to investigate any structural modification that might have happened due to surface phosphorylation (X-ray diffractometer; Bruker AXS D8 Advance). In order to study the glass transition (Tg) and melting (Tm) temperatures before and after surface phosphorylation, thermograms of bare and P-PET were evaluated by Differential Scanning Calorimetry (DSC; DSC Q20 V24.11 Build 124).

The water wettability and contact angle of PET, P-PET and CPH-P-PET were evaluated with contact angle goniometer (rame-hart Instrument co., USA) by the sessile drop method. Five locations on each samples were measured and the drop images were also recorded. All the measurements were performed 20s after the addition of water droplet. Water absorption capacity was further validated with swelling analysis of the scaffolds in phosphate buffered saline (PBS; pH 7.4). Swelling degree of all the specimens with size of 0.5 cm × 0.5 cm was studied at pre-defined time intervals [44]. The dry weight ($W_d$) of the specimens (triplicates) were taken prior to the experiment and transferred to 10 mL of PBS. The samples were kept at 37 °C and the wet weight of the samples were taken ($W_w$) at different time points after the removal of excess water from the surface of the scaffolds. The degree of swelling (%) was calculated using the following equation,

$$\text{Degree of swelling } (\%) = \frac{W_w - W_d}{W_d} \times 100 \tag{1}$$

The in vitro degradation profile of the samples were evaluated according to Younes et al. 2004 with slight modifications [45]. PET, P-PET and CPH-P-PET (triplicates of each) of size 1 cm × 0.5 cm were weighed and placed into bottles filled with 10 mL of PBS (pH 7.4). The tubes were kept in an orbital shaker with shaking speed of 60 rpm at 37 °C for 25 days. The buffer was replaced at regular intervals to ensure the physiological pH of 7.4. After incubation, all scaffolds were taken out and dried at 50 °C for overnight. The percentage degradation was determined using the following equation:

$$\text{Percentage degradation} = \frac{W_i - W_t}{W_t} \times 100 \tag{2}$$

where $W_i$ and $W_t$ are the initial weight and weight of the samples after degradation respectively. The morphology of CPH-P-PET scaffold after degradation study was analyzed by FESEM.

## 2.3. Cell culture

Human osteosarcoma MG-63 cells (Req. number 772) obtained from NCCS, Pune, India were cultured in Dulbecco's Modified Eagle Medium

(DMEM; Gibco, USA) supplemented with 10% (v/v) fetal bovine serum (Gibco, USA) and 1% (v/v) antibiotic solution (10,000 units/mL of penicillin and 10,000 μg/mL of streptomycin) (Sigma Aldrich, India) under standard culture conditions until it reaches ~90% confluency. The confluent cells were trypsinized using trypsin/EDTA (Sigma Aldrich, India) solution and used for evaluating biocompatibility and biomineralization of the scaffolds.

Rat bone marrow mesenchymal cells [BMC(s)] were used for the analysis of alkaline phosphatase and osteocalcin activity. The BMC(s) were isolated according to the previously described method [46]. Briefly, an eight week (270 g) old male rat (Sprague dawley) was euthanized and the femur bone was separated by cutting at the epiphysis. BMCs were isolated by flushing out cells from the femur bone using DMEM (Gibco, USA) supplemented with 10% (v/v) FBS (Gibco, USA) and 1% (v/v) antibiotic solution (Sigma Aldrich, India). The isolated cells were cultured in the same medium in $CO_2$ incubator (New Brunswick Galaxy 170 S, Germany) at 37 °C by providing aseptic condition. After 48 h of culture time, non-adherent cells were removed by refreshing the medium and the cells were maintained under the same procedure till the 4th passage.

### 2.3.1. Ethical statement

Animal procedures were performed based on the prior approval (363/GO/Re/S/01/CPCSEA,28.12.2017/07) from Institutional Animal Ethics Committee which is strictly adhered to the guidelines of Committee for the Purpose of Control and Supervision of Experiments on Animals (India).

## 2.4. Evaluation of biocompatibility of the scaffolds

Human osteosarcoma derived MG-63 cells were used for investigating biocompatibility of P-PET and PH-P-PET. The cytocompatibility of scaffolds was studied by 3-(4,5-dimethylthiazol-2-yl)-2,5-diphenyltetrazolium bromide (MTT), while cell adhesion was analyzed by actin staining. For MTT assay, $1 \times 10^4$ cells were seeded in a 24 well cell culture plate. After 24 h of culture, PET, P-PET and PH-P-PET scaffolds were incubated with the cells in a $CO_2$ cell culture incubator. On 2nd and 5th day of culture, MTT (Sigma Aldrich) solution (5 mg/mL in PBS) was added and incubated for 3 h at 37 °C [47]. The formazan crystals formed were dissolved using dimethylsulfoxide (Merck, India), transferred to a 96 well plate and the absorbance was measured at 595 nm in a plate reader (Spark® Multimode Microplate Reader, Tecan, Switzerland). The culture medium without cells was used as negative control. For cell adhesion experiment, $1 \times 10^3$ cells were seeded onto the scaffolds and cultured in $CO_2$ incubator for 48 h. After incubation, the cells on the scaffolds were fixed with 4% (w/v) paraformaldehyde (Sigma Aldrich, India), stained with Alexa Fluor 488 Phalloidin actin stain (Invitrogen™, USA) and observed under phase contrast inverted fluorescent microscope (Nikon Eclipse Ti2 Series, India). Triplicates of the samples were taken for the biocompatibility study.

## 2.5. Biofunctional assays of P-PET and CPH-P-PET

### 2.5.1. Biomimetic in vitro mineralization in simulated body fluid

The in vitro mineralization of PET, P-PET and CPH-P-PET (1 cm × 1 cm) has been studied as per the protocol reported by Kokubo and Takadama, 2006 [48]. The sterile scaffolds were immersed in 1.5X simulated body fluid (SBF) and incubated at 37 °C for 14 days. The medium was refreshed at regular time intervals of 24 h to avoid saturation of the medium and changes in pH. On 7th and 14th day, the scaffolds were taken out carefully, washed four times with deionized water to remove excess salts and dried at 37 °C for overnight. The biomimetic mineralization potential of the specimens were harvested using SEM-EDX (Jeol JSM 6390LV, Japan and OXFORD XMX N, UK) and Field Emission SEM (Carl Zeiss Sigma, Germany; XFlash 6I100 Bruker, USA) where the hydroxyapatite nucleation and its growth

profile were viewed at different time points.

### 2.5.2. Alizarin Red S and von Kossa staining

The MG-63 cells cultured for seven days on PET, P-PET and PH-P-PET scaffolds were stained with Alizarin red S (ARS) and von Kossa to evaluate the extent of biomineralization. The ARS staining was performed according to the previously reported protocol with slight modifications [49]. The cells ($1 \times 10^4$) cultured on the scaffolds were fixed with 4% (w/v) paraformaldehyde (Sigma Aldrich, India) solution and then stained with 40 mM Alizarin Red S (Sigma Aldrich, India). The pH of the staining solution was maintained as 4.2. The culture plates were incubated at room temperature for 20 min with gentle shaking. Following incubation, unincorporated dye was washed out using distilled water and the scaffolds were imaged under inverted microscope (Nikon Eclipse Ti2 Series, India). For von Kossa staining, the adhered cells on the scaffolds were fixed with 4% (w/v) paraformaldehyde solution and incubated with 5% (w/v) silver nitrate (Spectrochem Pvt. Ltd., India) under ultraviolet light for 20 min [50]. The unreacted silver nitrate was removed and the reaction was stopped by adding 5% (w/v) sodium thiosulfate (Sigma Aldrich, India). The mineralized scaffold show black nodules in the case of von Kossa staining while it appears with red spots following ARS staining. The same staining procedures were followed for the control cells (cultured on surface-treated cover slips).

### 2.5.3. Alkaline phosphatase and osteocalcin activity

BMCs were seeded on the P-PET scaffolds of size 1 cm × 1 cm at a density of $1 \times 10^4$ cells per well and used for the evaluation of alkaline phosphatase (ALP) and osteocalcin (OSN) activity. Once the cells adhered, one set of wells [sample size (n) is 6] from each group were further cultured by supplementing with osteogeneic differentiation medium (Himedia laboratory, India), however, another set ($n = 6$) was maintained in the same culture media (complete DMEM). On 14th and 21st day of culture, the cells cultured in both osteogenic medium and complete DMEM were harvested through trypsinization and washed with ice-cold PBS (freeze and thaw method), repeatedly, until the complete cell lysis. The aliquots of lysate were used for evaluating the ALP and OSN activity. The ALP activity in BMCs was studied based on the previously published procedure [51,52]. For ALP activity, the aliquots of the cells were treated with the substrate para-nitrophenyl phosphate (Sigma Aldrich, India) for 60 min at 37 ˚C. After incubation, the reaction was stopped by the addition of 0.2 N NaOH (Merck, India) and the absorbance was measured at 410 nm using a multi-well plate reader (Spark® Multimode Microplate Reader, Tecan, Switzerland). Protein estimation was carried out by Lowry's method [53]. The results were expressed as U/μg protein. A calibration curve was also plotted using the standard p-nitrophenol solution (Sigma Aldrich, India).

The level of OSN in the cell lysate was evaluated using Rat Osteocalcin/Bone gla protein (OT/BGP) ELISA Kit (Origin diagnostics, India). To 40 μL of the sample (cell lysate), anti-OT/BGP antibody (10 μL) and streptavidin-HRP conjugate (50 μL) were added and incubated for 60 min at 37 ˚C. After incubation, washed the wells with 1X washing solution (five times) provided with the assay kit and added chromogen solution A and B (50 μL each). Finally, it was incubated for 15 min at 37 ˚C away from light for colour development. Then, the reaction was stopped by adding stop solution (50 μL) and absorbance was measured at 450 nm using multi-well plate reader (Spark® Multimode Microplate Reader, Tecan, Switzerland). A standard graph (1.5–48 ng/mL) was plotted according to the protocol provided by the kit manufacturer. Simultaneously, blank was also prepared by adding chromogen A, chromogen B and stop solution.

### 2.5.4. Morphology of BMCs on P-PET

The morphology of BMCs adhered on P-PET for 14 days was visualized by FESEM. The cells adhered on the scaffolds were fixed with 2% (v/v) glutaraldehyde solution for 10 min; dehydrated with a series of graded alcohol (30%, 50%, 70%, 90% and absolute) and air dried. Further, the scaffold was gold sputtered and scanning electron micrographs were captured.

### 2.5.5. Release profile of ciprofloxacin from the CPH-P-PET and antimicrobial activity

The CPH-P-PET scaffold (triplicates) of size 0.5 × 0.5 cm were immersed in PBS (1X, pH 7.4) and incubated at 37 ˚C in a shaking environment. The medium (200 μL) was collected at predetermined time intervals, initially, for 5 days and continued for 14 days. Further, the medium was replenished with equal volume of fresh PBS. The absorbance was measured at 270 nm using multi-mode Plate reader (Spark® Multimode Microplate Reader, Tecan, Switzerland). The cumulative release of ciprofloxacin from CPH-P-PET was calculated based on the standard graph plotted with known concentrations of ciprofloxacin. The percentage release of ciprofloxacin at various time points were also calculated. The antibiotic loaded on the scaffold was calculated using the equation [54],

$$Ciprofloxacin - loaded\ (\%)$$
$$= \frac{Total\ amount\ of\ ciprofloxacin - Unbound\ ciprofloxacin}{Total\ amount\ of\ ciprofloxacin} \times 100$$

(3)

The antimicrobial activity of ciprofloxacin eluted from CPH-P-PET was evaluated by agar disc-diffusion method [17] in bacterial strains – gram-positive *Staphylococcus aureus* (NCIM number 2127) and gram-negative *Escherichia coli* (NCIM number 2343). Briefly, agar (Mueller-Hinton agar) plates were prepared and incubated at 37 ˚C for 24 h. Following the incubation, the bacterial suspension ($1 \times 10^8$ cfu/mL) was spread on the agar plate. Filter paper discs of 6 mm size were placed on the plates and added 20 μL of the test solution of concentration 3 μg on to it. The ciprofloxacin –released from CPH-P-PET at time points 8 h and 24 h was used as the test solutions. Then the plates were incubated upside down for overnight at 37 ˚C. Ciprofloxacin (3 μg/20 μL) and ultrapure water were used as positive and negative controls, respectively. Triplicates of the experiments were carried out to express the antibacterial activity of the test solution in terms of zone of inhibition (ZOI) formed around the disc. ZOI was calculated by measuring the diameter of the growth inhibition zone around the disc.

Additionally, the anti-adhesion efficacy of the CPH-P-PET was studied by incubating the scaffold and its controls (P-PET, positive and negative controls) in bacterial suspension ($1 \times 10^8$ cfu/mL) for 24 h [55]. The suspension of gram-positive *Staphylococcus aureus* was used for this study. After incubation, the scaffolds were washed thrice with PBS and fixed the bacteria by 2.5% gluteraldehyde solution for 1 h. Further, the scaffolds were dehydrated by the treatment with graded ethanol (25%, 50%, 75% and absolute ethanol) and vacuum dried. Finally, FESEM of the dried scaffolds were taken to identify the presence of bacteria.

### 2.6. Statistical analysis

All the values are presented as mean ± SD. The statistical significance of data was analyzed by ANOVA (Tukey's multiple comparison test) using GraphPad Instat3 software. p value < .05 was considered as statistically significant.

## 3. Results

### 3.1. Physicochemical characterization of CPH-P-PET

The surface transformation of PET as a dual system was initially identified from ATR spectra (Fig. 1). The ATR spectrum of PET (Fig. 1(a)) exhibits characteristic peaks at 1241 cm$^{-1}$ and 1119 cm$^{-1}$ corresponds to the terephthalic group and –C=O stretch at 1707 cm$^{-1}$.
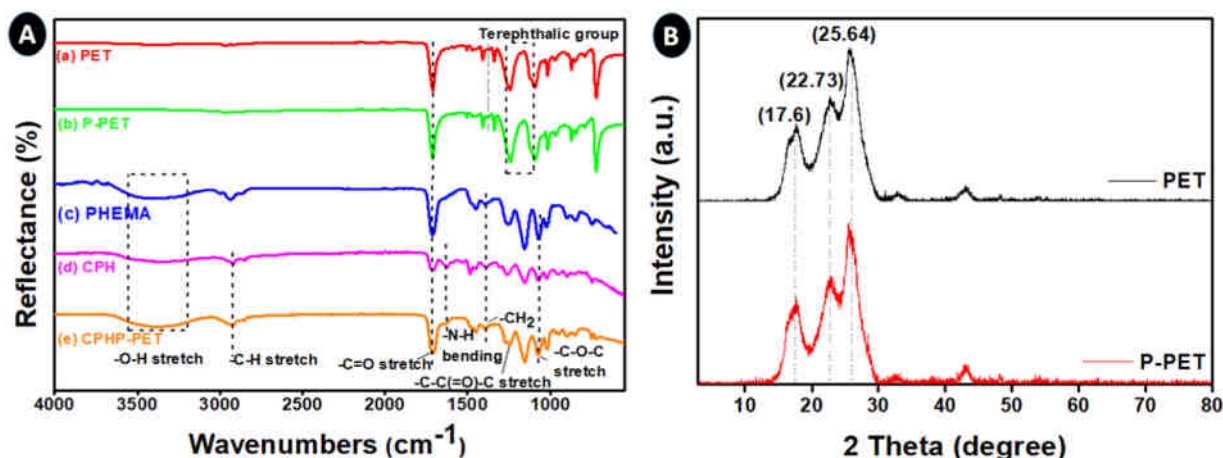
**Fig. 1.** (A) ATR spectra of PET, P-PET and CPH-P-PET. [(a): PET, (b): P-PET, (c) poly (HEMA), (d): CPH [ciprofloxacin-loaded poly (HEMA)] and (e): CPH-P-PET]. (B) XRD analysis of PET and P-PET.

Further, a sharp peak at 714 cm$^{-1}$ is assigned to the interaction of benzene ring with polar ester group of PET. In addition, the peaks at 860 cm$^{-1}$ and 966 cm$^{-1}$ are characteristics of aromatic ring in PET [56,57]. The peaks responsible for inorganic phosphate groups normally appears in the range 850 cm$^{-1}$ to 1250 cm$^{-1}$ [58,59]. However, in P-PET the peaks ascribed to –P=O and –P-OH could not be distinguished clearly due to the presence of terephthalic group and aromatic ring in the same position (Fig. 1(b)). *In situ* coating of poly (HEMA) - impregnated with ciprofloxacin onto P-PET was evidenced from Fig. 1(e) where the peaks at 1627 cm$^{-1}$, 3379 cm$^{-1}$ and 1388 cm$^{-1}$ are assigned to –N-H bending vibrations of quinolone group present in ciprofloxacin, hydroxyl (-O-H stretching) and –CH$_2$ groups of poly (HEMA) respectively [60,61]. XRD patterns of PET and P-PET are shown in Fig. 1B. The three characteristic reflections of PET observed at 2θ values 17.6, 22.73 and 25.64 are corresponding to the Bragg's reflections d (010), d (110), and d (100), respectively [38,63]. It could be apparent from the figure that the XRD pattern of P-PET resemble well as that of PET, indicating that surface phosphorylation did not alter the crystallinity of PET. There is no significant difference in the DSC thermograms of bare PET and surface phosphorylated PET (P-PET) (supporting information Fig. 1).

The surface phosphorylation on P-PET was evidenced by the elemental composition of PET and P-PET obtained from XPS analysis (Fig. 2). The survey spectrum of PET showed two high intense peaks at 283.9 eV and 532.0 eV which represents C1s and O1s respectively [Fig. 2(a1)], while P-PET has shown an additional peak with lower intensity at 132.9 eV along with C1s (283.9 eV) and O1s (531.9 eV) [Fig. 2(a2)]. A peak with binding energy at around 133 eV is generally ascribed to phosphate group which confirm the surface phosphorylation on P-PET [62]. Further, P2p scan showed a clear evidence for the presence of phosphate group in P-PET [Fig. 2(d)].

The surface texture of PET exhibited smooth fibrous matrix with diameter of 14.1 ± 0.4 μm under FESEM as depicted in Fig. 3A(a). Surface phosphorylation on P-PET and CPH-P-PET was evidenced from FESEM/EDX elemental analysis [Fig. 3B(b) and 3C(b)] and its mapping (supporting information Fig. 2). It is clearly apparent that functionalization by surface phosphorylation did not alter the micro-structure of PET significantly [Fig. 3B(a)]. Further, the micro-structure was covered by a coating of poly (HEMA) loading ciprofloxacin. This *in situ* coating on CPH-P-PET by surface polymerization has increased the surface roughness [Fig. 3C(a)]. In addition, there was no significant difference noticed in the phosphate content in CPH-P-PET (0.205 ± 0.08 atomic %) compared to P-PET (0.215 ± 0.01 atomic %) [Fig. 3B(b) and C(b)]. P-PET has showed 42% of porosity while it has reduced to 24% in the case of CPH-P-PET. This might be attributed to the surface transformation of P-PET by poly (HEMA) coating.

The water contact angle and swelling behaviour of the material were studied to identify its suitability in biological system. PET has a contact angle value of 125.43° ± 6.7 [Fig. 4A and B(a)] which is a major setback of the material that limits its application towards bone regeneration. P-PET, on the other hand, shows a contact angle value of 97.9° ± 2.8 [Fig. 4A and B(b)] due to inorganic phosphate group on the surface and hence, overcomes the challenge in bone tissue engineering. Drastic change in the contact angle values of CPH-P-PET (62.7° ± 8.4) [Fig. 4A and B(c)] was recorded with statistical significance of $p < 0.001$ which excavate the synergistic effect of poly (HEMA) and phosphate groups in contributing hydrophilicity to CPH-P-PET. Likewise, it is evident that CPH-P-PET is highly hydrophilic than P-PET as it could swell up to 70% (p < 0.001) at 15 min which further increased to 84% at 24 h (Fig. 4C). However, P-PET exhibited only 26% swelling at 15 min which reached to a maximum of 38% which is concordant with the contact angle results. In addition, the swelling saturation is accomplished within a short span of 30 min and maintains a plateau thereafter. On the contrary, PET has showed swelling of 24% which might be contributed by PBS entrapped in the porous matrix (Fig. 4C).

The *in vitro* degradation of PET, P-PET and CPH-P-PET has been studied for 25 days (Fig. 4D). As expected, there was no weight loss in the case of PET. Less than 0.2% of degradation was observed in P-PET, while CPH-P-PET has showed approximately 8% of degradation under dynamic condition in PBS. The microstructure of CPH-P-PET shows attractive network like appearance further provides authentic visual evidences for the degradation pattern of CPH-P-PET (Fig. 4E and F).

### 3.2. Cell viability and cell adhesion on P-PET and PH-P-PET scaffol

The viability of MG-63 cells on P-PET and PH-P-PET scaffolds was evaluated by MTT assay at two time points (2$^{nd}$ and 5$^{th}$ day) and expressed as absorbance value at 595 nm (Fig. 5A) which is directly proportional to the cell viability. . An increase in the cell viability with respect to time indicates proliferation index. Similar to controls, proliferation index was significantly higher for both P-PET and PH-P-PET ensuring cytocompatibility of the scaffolds. The actin staining results provided visual evidence of cell adherence (Fig. 5B), further confirms the cytocompatibility. Further, the *in situ* polymer coating on P-PET also presents a highly favourable cell-surface interaction (Fig. 5B(c)).

### 3.3. Surface transformation of PET induces biomimetic in vitro mineralization

The bare PET has not shown any sign of calcium phosphate nucleation when incubated in 1.5X SBF (Figs. 6A and 7A), while the
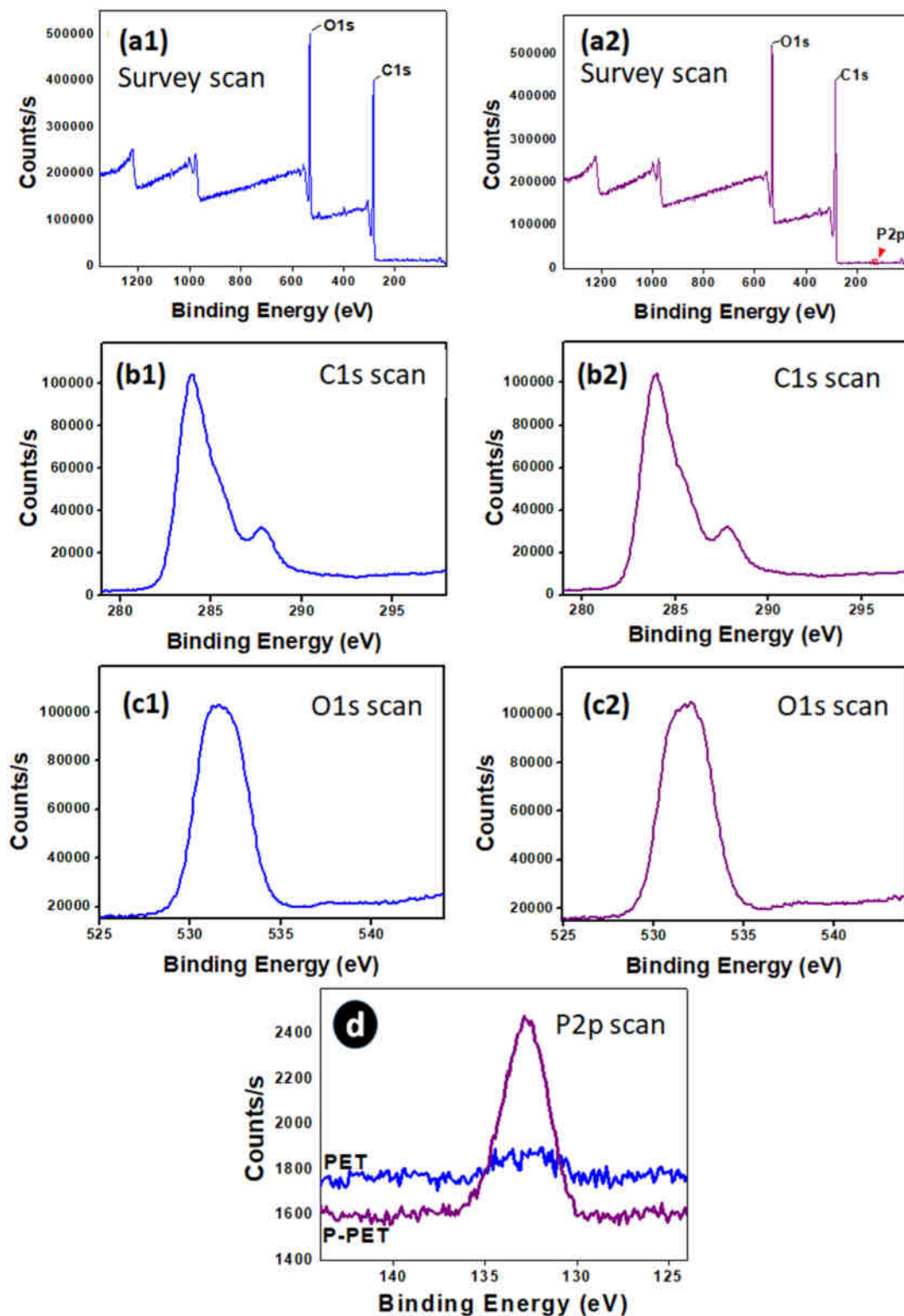
**Fig. 2.** XPS spectra of PET and P-PET. (a1) and (a2) represent survey spectra; (b1) and (b2) represent C1s scan of PET and P-PET; (c1) and (c2) represent O1s scan of PET and P-PET respectively. (d) presents P2p scan of both PET and P-PET.

primary nucleation of apatite happens at very early stage in P-PET and by 7 days the fibrous matrix is beautifully decorated with spheroidal apatite crystals (Fig. 6B(a), (b) and (c)). In each fibre of the P-PET scaffold, several nucleation sites exist and the secondary growth propagate thereafter and ensures complete coating of the matrix by day 14 (Fig. 6B(d), (e) and (f)). The calcium and phosphate level increased from 7.16 ± 3.12 atomic % and 2.86 ± 0.22 atomic % at day 7 to

12.24 ± 3.01 atomic % and 6.25 ± 1.58 atomic % by day 14, respectively as viewed from EDX spectra (Fig. 7B and Table 1). CPH-P-PET also followed similar pattern in growth profile with early mineralization and spreading of calcium phosphate by day 7 with Ca/P ratio 1.53 by day 7 to an intensified secondary growth with Ca/P ratio 1.70 at day 14 (Figs. 6C, 7C and Table 1). The elemental mapping of CPH-P-PET has provided further visual proof for the mineralization potential
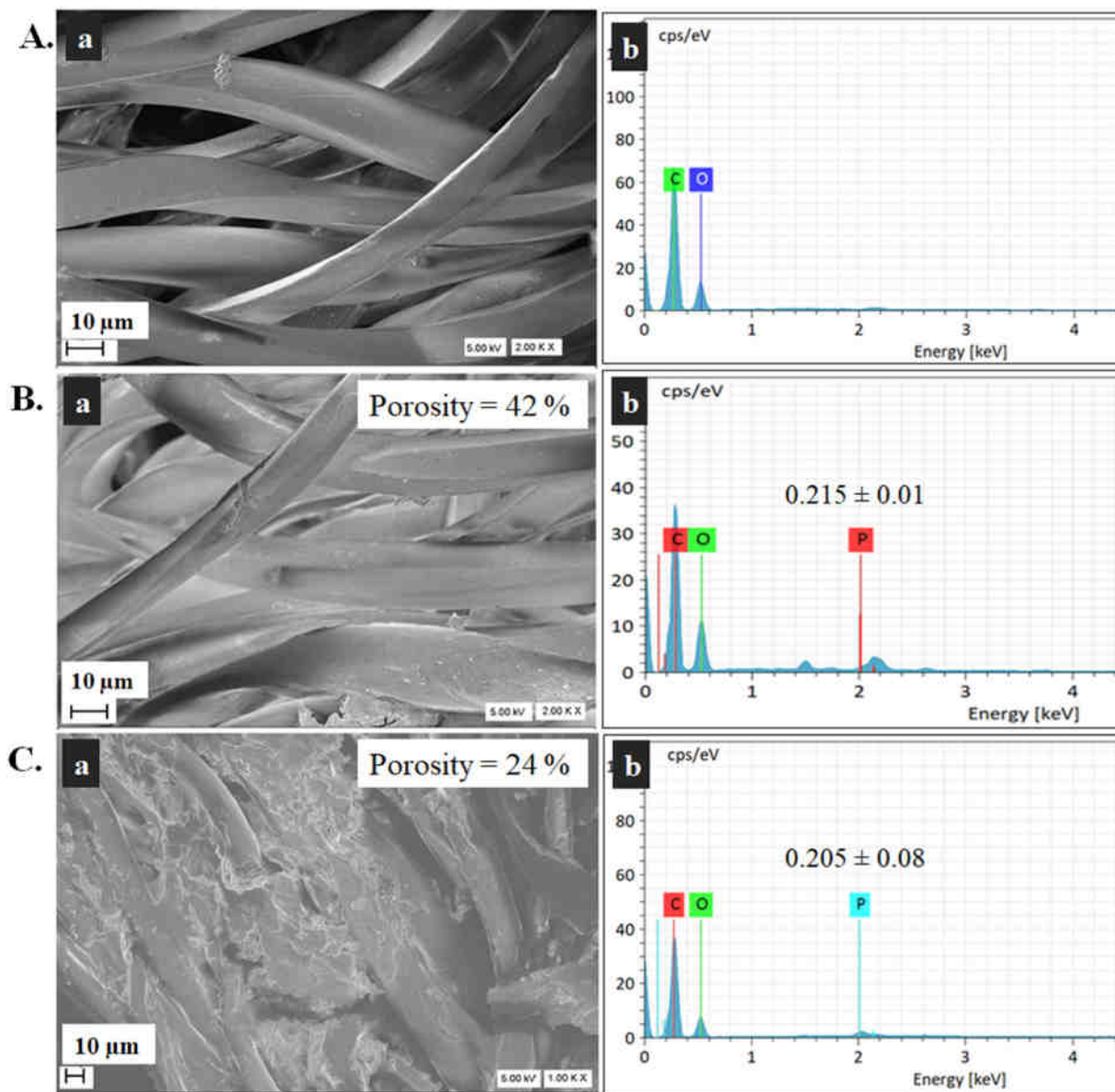
**Fig. 3.** Surface morphology and elemental analysis of (A) PET, (B) P-PET and (C) CPH-P-PET. A(a), B(a) and C(a) represent FESEM of PET, P-PET and CPH-P-PET respectively [inset is the porosity value], while A(b), B(b) and C(b) show corresponding EDX spectra.

(supporting information Fig. 3).

### 3.4. Surface-transformed PET - induced calcium-phosphate mineralization

Biomineralization of P-PET and PH-P-PET was further evaluated with MG-63 cells by ARS (Fig. 8A and B) and von Kossa staining methods (Fig. 8C). Following seven days of culture, P-PET and PH-P-PET scaffolds expressed red spots throughout the scaffolds revealing the presence of calcium phosphate deposits (Fig. 8A(c and d)). Furthermore, the results provide authentic proof for the attachment and growth of MG-63 cells on both P-PET and PH-P-PET scaffolds and corroborate observations by acting staining (Fig. 5B). Most importantly, the results elicit the suitability of PH-P-PET for bone regeneration applications. Even though PET scaffold exhibited cell adhesion (Fig. 8A(b)), the cell density was significantly lower than P-PET and PH-P-PET. To further confirm the findings, von Kossa staining of PET and PH-P-PET scaffolds was also performed (Fig. 8C). The von Kossa staining offered dark brown to black spots developed on PH-P-PET which validate further the degree of mineralization (Fig. 8C) which is

absent in PET. Similar to ARS, the intensity of the colour is directly proportional to the extent of mineralization [64]. The black nodule formation was due to the strong light – induced reduction of the product formed by interaction of silver with phosphates in calcium deposits [65].

### 3.5. CPH-P-PET induced osteogenic differentiation of bone marrow mesenchymal cells

Osteogenic differentiation potential of a biomaterial could be easily recognized based on the expression of various markers. The differentiation markers such as ALP and OSN were identified in BMC (multipotent cells) cultured on P-PET in standard culture medium (DMEM; D) and osteoblast differentiation medium (ODM, O) (Fig. 9A and 9B). On 14th day, the specific activity (the amount of p-nitrophenol formed per unit time per μg of protein) of ALP was found to be increased ($p < 0.001$) in O-control compared to D-control group, suggests the osteogenic differentiation potential of the BMCs. Similar changes were also seen in O-P-PET compared to D-control ($p < 0.001$). At the same
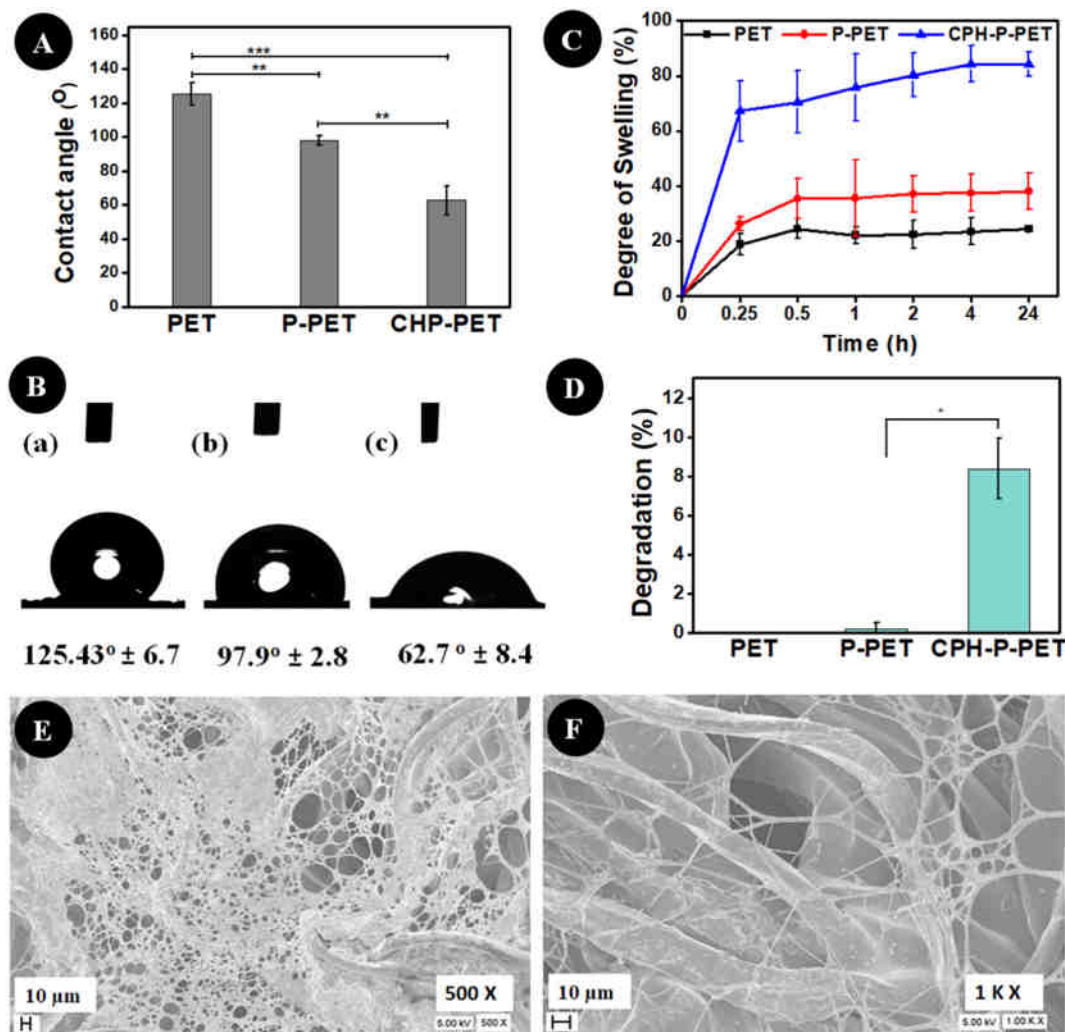
**Fig. 4.** Swelling behaviour, contact angle values and *in vitro* degradation of PET scaffolds. (A) Contact angle values; (B) Contact angle images of the scaffolds [B(a): PET, B(b): P-PET and B(c): CPH-P-PET]; (C) Percentage degree of swelling of the scaffolds in PBS; (D) Percentage degradation (*in vitro*) in PBS under dynamic condition; (E) and (F) FESEM images of CPH-P-PET after *in vitro* degradation at different magnifications (E: 500 X and F: 1000 X). Note: All values are presented as mean ± S.D. '*', '**' and '***' indicate statistical significance with $p$ value < 0.05, < 0.01 and < 0.001 respectively, while 'ns' indicates non-significance with p value > 0.05 when compared to its respective controls.
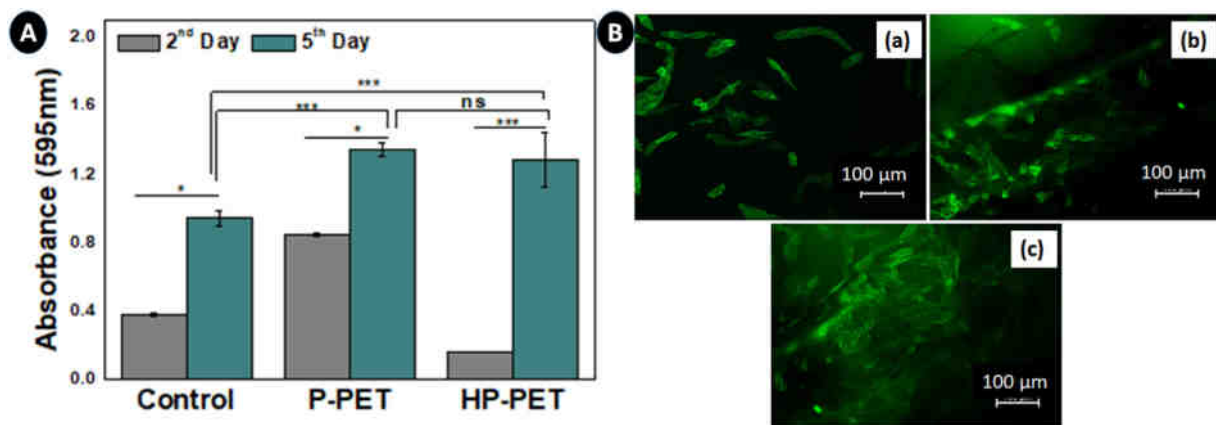


**Fig. 5.** *In vitro* cytocompatibility assays with MG-63 cells. (A) MTT assay at day 2 and day 5 (B) Images of actin filaments of (a) Control MG-63 cells (without scaffold); (b) MG-63 cells on P-PET and (c): MG-63 cells on PH-P-PET. Note: Values are presented as mean ± SD. 'ns' indicates non-significance while '*' ($p$ < 0.05) and '**' ($p$ < 0.01) indicate statistical significance.
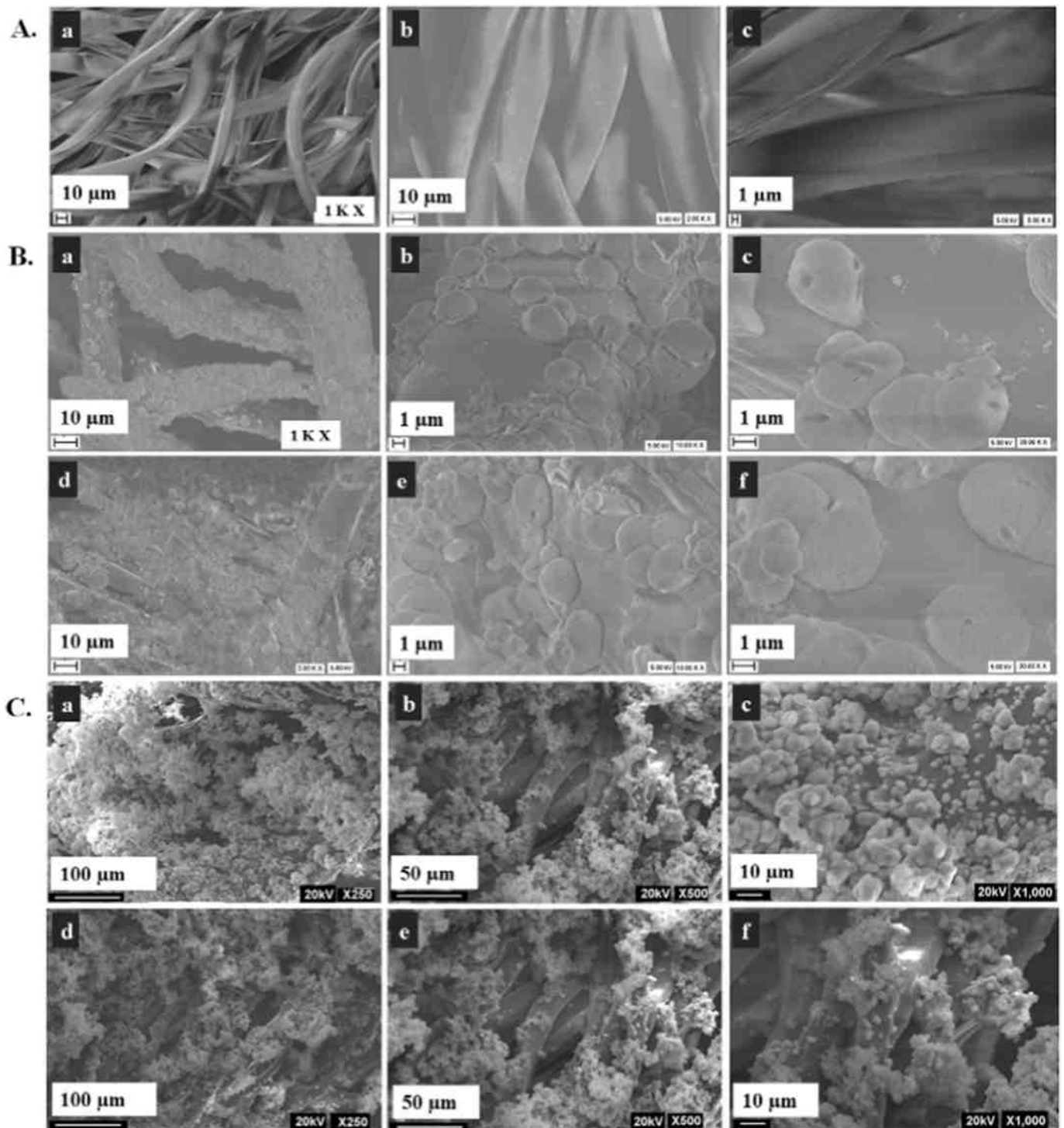
**Fig. 6.** Biomimetic mineralization of P-PET and CPH-P-PET incubated in 1.5X SBF for 7 and 14 days [A: PET, B: P-PET and C: CPH-P-PET]. A(a), A(b) and A(c): FESEM images of PET on day 14; B(a), B(b) and B(c): FESEM images of P-PET on day 7 and B(d), B(e) and B(f): FESEM images of P-PET on day 14; C(a), C(b) and C(c): FESEM images of CPH-P-PET on day 7 and C(d), C(e) and C(f): FESEM images of CPH-P-PET on day 14.

time, there was a statistically significant difference ($p < 0.001$) in ALP levels of O-P-PET and O-control. Moreover, the same pattern in ALP activity was observed in D-P-PET (without osteogenic medium) which authenticate the capability of P-PET to transform BMC to osteogenic lineage (Fig. 9A). On 21st day, ALP activity was found to be decreased significantly in D-P-PET, O-control and O-P-PET than 14th day ($p < 0.001$). On the other hand, the OSN level (expressed per mg protein) was increased significantly in D-P-PET ($p < 0.001$), O-control ($p < 0.01$) and O-P-PET ($p < 0.001$) on day 21 than day 14 (Fig. 9B).

D-control had shown no noteworthy difference in OSN level on day 21 than day 14. The morphology of BMCs upon interaction with the surface of P-PET at day 14, depicted in Fig. 9C and 9D, showed a monolayer formation of cells on the P-PET.

*3.6. Growth inhibitory effect of ciprofloxacin release from CPH-P-PET in S. aureus and E. coli*

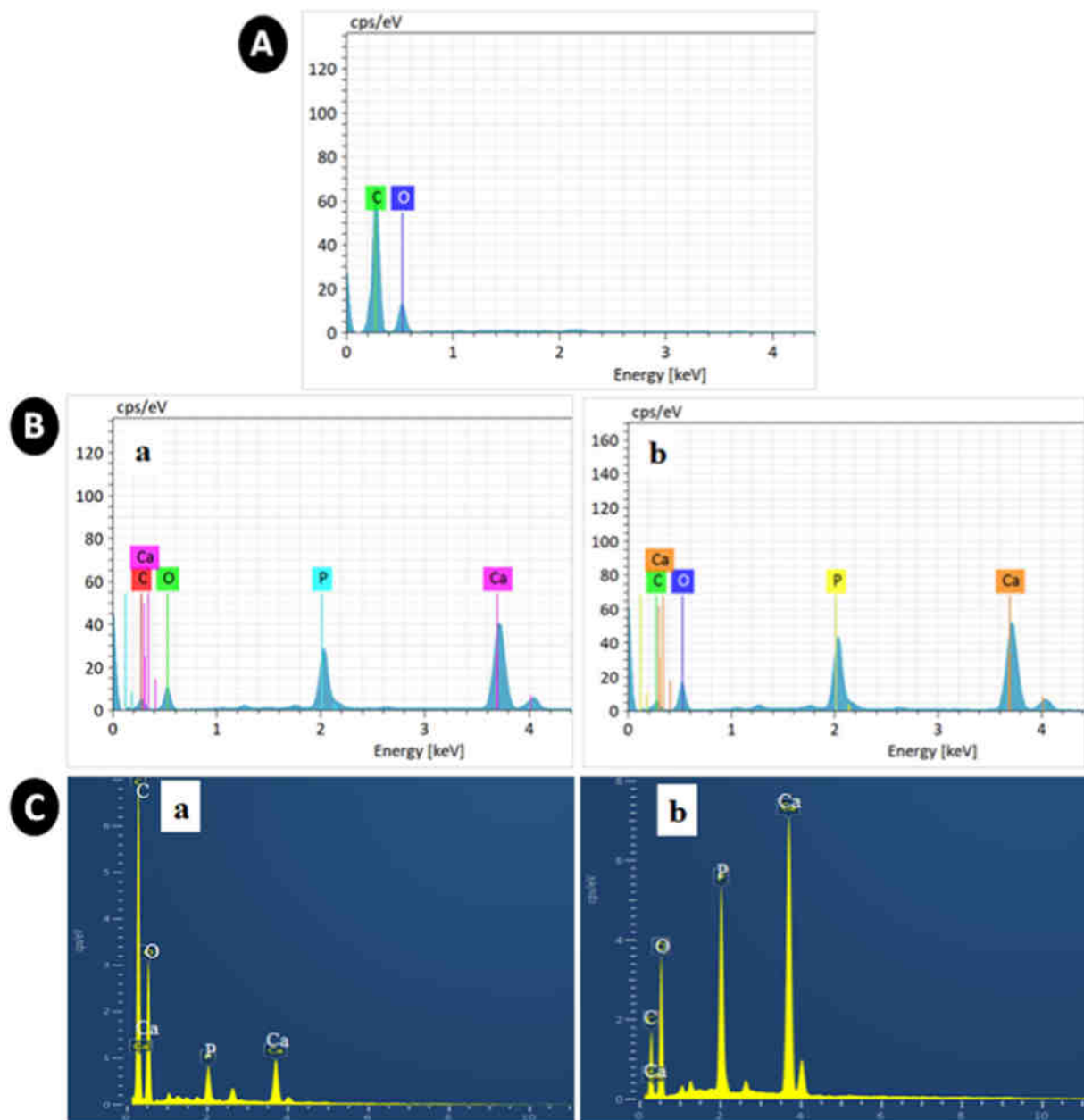The ciprofloxacin – released from CPH-P-PET at pre-defined time

**Fig. 7.** EDX spectra of PET, P-PET and CPH-P-PET. A: PET (day 14), B: P-PET [B(a): day 7 and B(b): day 14] and C: CPH-P-PET [C(a): day 7 and C(b): day 14].

**Table 1**
Ratio of Ca/P in PET, P-PET and CPH-P-PET after biomimetic mineralization in SBF.

| Scaffold name | 7th day | | | 14th day | | |
|---|---|---|---|---|---|---|
| | Ca (atomic %) | P (atomic %) | Ca/P | Ca (atomic %) | P (atomic %) | Ca/P |
| PET | 0 | 0 | – | 0 | 0 | – |
| P-PET | 7.2 ± 3.1 | 2.9 ± 0.2 | 2.51 | 12.2 ± 3.0[b] | 6.25 ± 1.5[b] | 1.96 |
| CHP-PET | 2.2 ± 1.2 | 1.4 ± 0.8 | 1.53 | 10.1 ± 1.8[c] | 5.88 ± 0.7[c] | 1.70 |

Note: All values are presented as mean ± SD. '[b]' (p < 0.05) and '[c]' (p < 0.01) indicate statistical significance when compared to PET.

intervals was measured and represented as percentage release against time. Ciprofloxacin loading on P-PET was calculated as 12.14% (1.21 mg) of total antibiotic used for its preparation. From the Fig. 10A(a), it is obvious that there was no burst release at the initial time period, but a two-stage release profile has been accomplished. At the initial hours until hour 4, 20% of loaded ciprofloxacin-infused in CPH-P-PET has been released. This is followed by a rapid release from 8 h which is maintained at the same pace till 48 h as in the case of first 4 h. Subsequently, a shoot up in ciprofloxacin release was noticed at 72 h and continued till 120 h. Almost 60% of antibiotic loaded in CPH-P-PET was released within 5 days, however, afterwards a slow pace of release was observed. Total release up to 70% was detected by 14 days [Fig. 10A(b)]. The antibacterial effect of ciprofloxacin-loaded in CPH-P-PET scaffold has been evaluated by performing antibacterial disc-diffusion assay using extracts from CPH-P-PET. The inhibitory effects of ciprofloxacin eluted from CPH-P-PET at two different time points (8 h and 24 h) were tested against both gram-positive and gram-negative bacteria identified as causative microorganisms of bone infections (Fig. 10B and 10C). Zone of inhibition was measured and generally, it is directly proportional to antibacterial activity. The antibiotic extracted from CPH-P-PET at 8 h (sample 1) and 24 h (sample 2) have shown zone
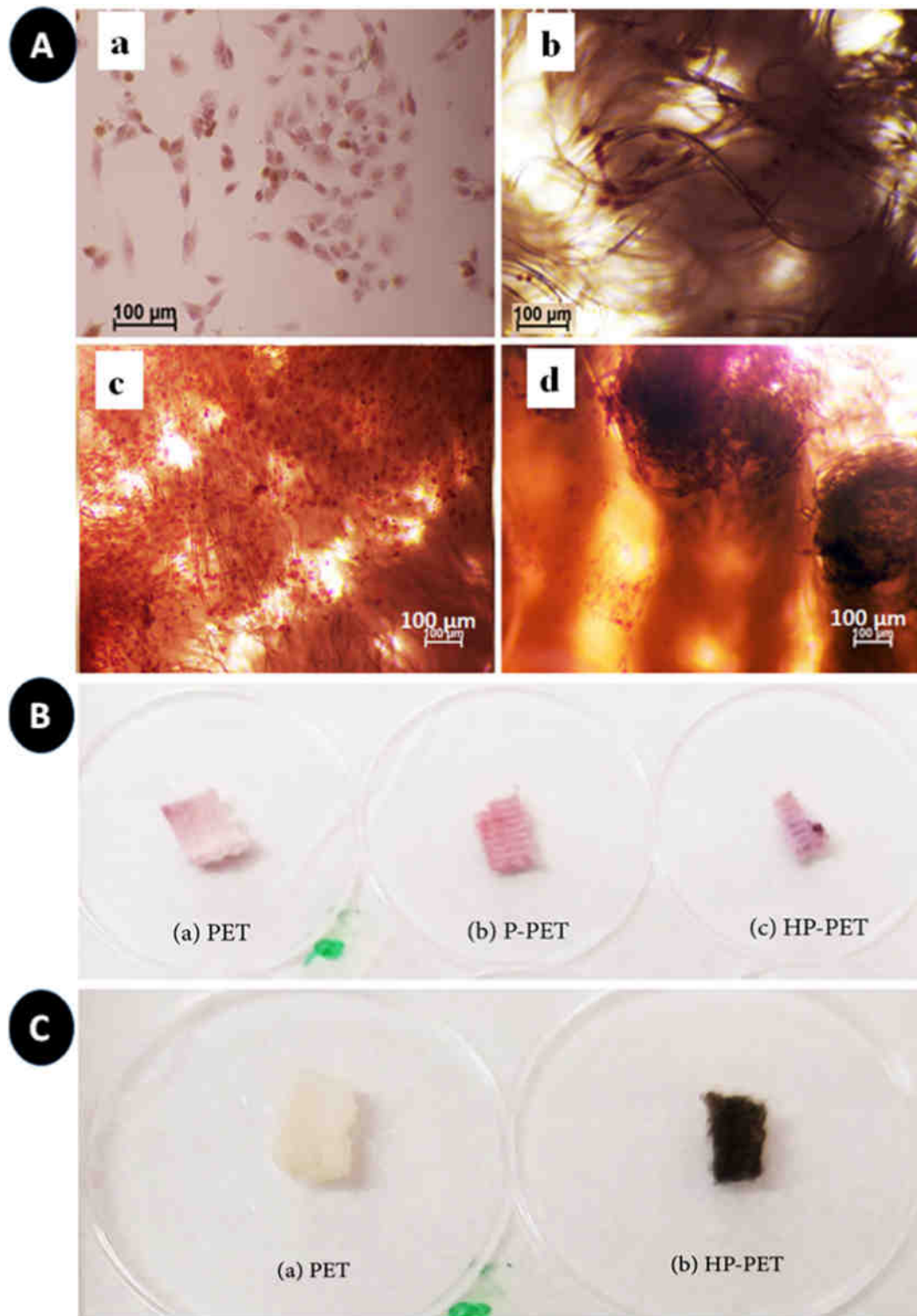
**Fig. 8.** Biomineralization study by Alizarin Red and von Kossa staining. A: Phase-contrast microscopic images of the scaffolds (Scale bar: 100 μm); B: Images of the scaffolds after Alizarin Red staining and C: Images of scaffolds after von Kossa staining. A(a): MG-63 Cells alone; A(b): PET; A(c): P-PET and A(d): PH-P-PET.

of inhibition (ZOI) of 3.44 ± 0.07 cm and 3.60 ± 0.3 cm, respectively, against *S. aureus*. Similarly, ZOI in *E. coli* was 2.93 ± 0.07 cm and 3.0 ± 0.8 cm for sample 1 and 2, respectively. At the same time, the ZOI of positive control was found as 4.7 ± 0.2 cm in *S. aureus* and 3.7 ± 0.7 cm in *E. coli*. FESEM images of CPH-P-PET and P-PET scaffolds following the anti-adhesion study have provided precise evidences that the CPH-P-PET has prevented the adhesion of *S. aureus*

significantly while these organisms were found to be attached on P-PET (Fig. 11). From the above observations, it is apparent that the antibiotic incorporated surface – designed PET could be used as an excellent antibiotic delivery system.
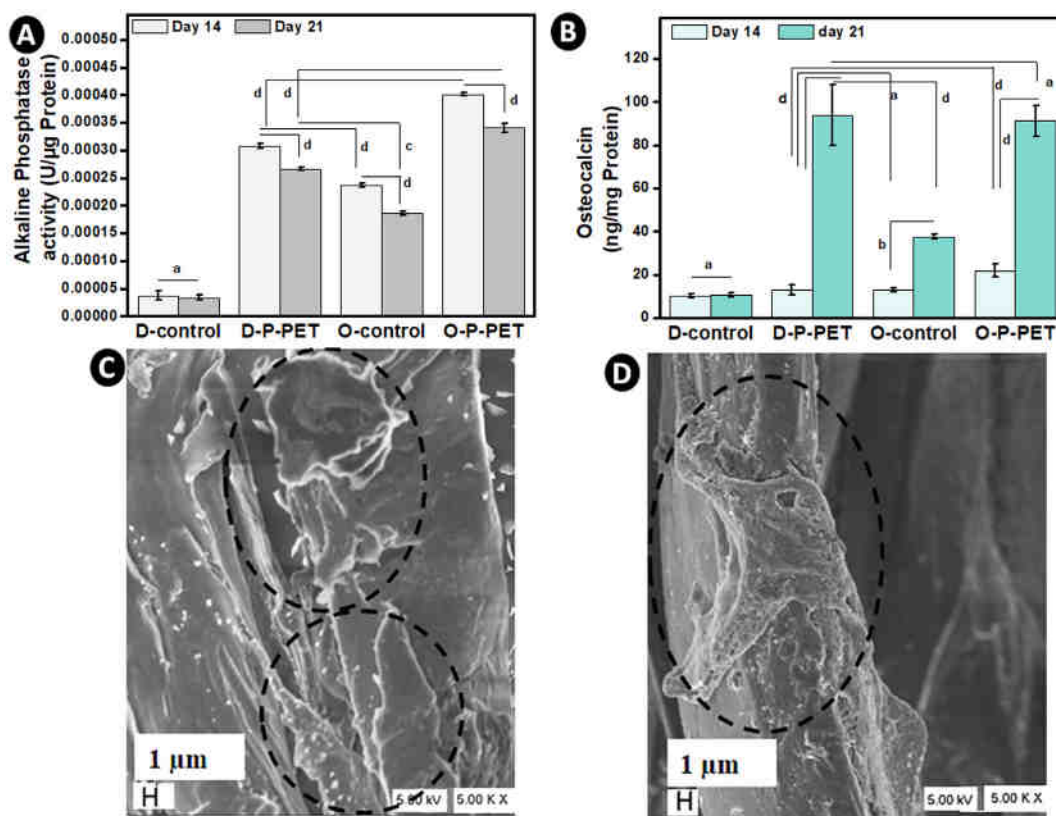
**Fig. 9.** Levels of osteogenic differentiation markers – alkaline phosphatase and osteocalcin - in bone marrow mesenchymal cells. Specific activity of ALP in BMCs cultured in both normal and osteogenic medium is expressed as U/µg protein (A). The amount of OSN is expressed in ng/mg protein (B). [D-control: BMC alone in DMEM; D-P-PET: BMC cultured on P-PET supplemented with DMEM; O-control: BMC cultured in ODM and O-P-PET: BMC cultured on P-PET in ODM]. C and D: FESEM of BMCs on P-PET on day 14. Note: All values are presented as mean $\pm$ SD. 'a' indicates non-significance ($p > 0.05$); 'b', 'c' and 'd' indicates statistical significance with $p$ values $< 0.05$, $< 0.01$ and $< 0.001$, respectively.

## 4. Discussion

Bone infection has been one of the major concerns in bone tissue regeneration. In order to circumvent infections associated with bone and enhance bone regeneration; scaffolds for bone tissue engineering ideally demand a porous structure to ensure the movement of biological fluid, adherence and proliferation of osteoblasts along with an appropriateness to local antibiotic delivery.

The microstructure of the PET matrix, its ester group together with intrinsic biocompatibility paved a pronounced insight in considering the material for bone tissue regeneration applications. In order to transform it as a better candidate, the first step required was to prepare it eligible to induce *in vitro* mineralization, which was accomplished by surface phosphorylation and confirmed by XPS and EDAX analysis (Figs. 2 and 3).

The surface hydrophilicity of the scaffold has a key role in dictating the biofunctional roles of polymeric scaffolds through surface interactions in the biological milieu. Moreover, in the case of bone regeneration, anionic hydrophilic functional groups such as $PO_4^{3-}$, –COOH, $-NH_2$ *etc.* play prominent role in primary nucleation and mineralization [66,67]. Water contact angle measurements is a direct measure of the water absorption capacity of the scaffold. It is well known that a material with contact angle value $< 90°$ is considered as hydrophilic [68]. PET with a contact angle of $125°$ has transformed to P-PET ($97°$); greater hydrophilicity than PET acquired through surface phosphorylation while CPH-P-PET has $62°$ due to the *in situ* polymerization of HEMA on P-PET. Both presence of surface phosphate groups as well as improved hydrophilicity offer enhanced compatibility, better interaction with biological system and triggered early mineralization of apatite (Figs. 5 and 6).

However, *in situ* coating of poly (HEMA) on P-PET with the aim of transforming it as a dual system has increased the surface roughness (Fig. 3Ca) which has a paramount role in the primary nucleation of calcium phosphate as reported previously [69]. In addition, it has to be noticed that there was no significant change in phosphate content of dual functional system (CPH-P-PET) suggests the accessibility of phosphate groups on CPH-P-PET to support primary calcium phosphate nucleation.

In addition to hydrophilicity, degradation profile of the scaffold has a prominent role in the success of the bone graft. It is important to mention that slow degradation profile was found to be helpful for retaining the material at the damaged site for prolonged period to provide long term support and to deliver antimicrobial agents during severe bone infection [70]. In the present study, it is apparent that the degradation pattern and surface micro-texture has altered significantly after *in situ* coating with ciprofloxacin – impregnated poly (HEMA) on P-PET. In addition, the weight loss in CPH-P-PET might also be contributed by the release of ciprofloxacin under dynamic physiological condition. From the swelling and degradation pattern of CPH-P-PET, it is obvious that poly (HEMA) on P-PET swells by absorbing water which lead to the release of ciprofloxacin incorporated into it and thereby expose the interconnected pores of the matrix to facilitate better physiological environment to support bone regeneration.

It is pertinent to discuss that the adherence of cells on biomaterials has been influenced by various parameters such as chemical composition, surface properties, mechanical characteristics and water wettability. In addition, the functional groups on the biomaterial surface also play key roles in cell adhesion through modifying its surface properties [71]. Therefore, the better attachment and proliferation index of MG-63 cells on P-PET (Fig. 5) could be accomplished through
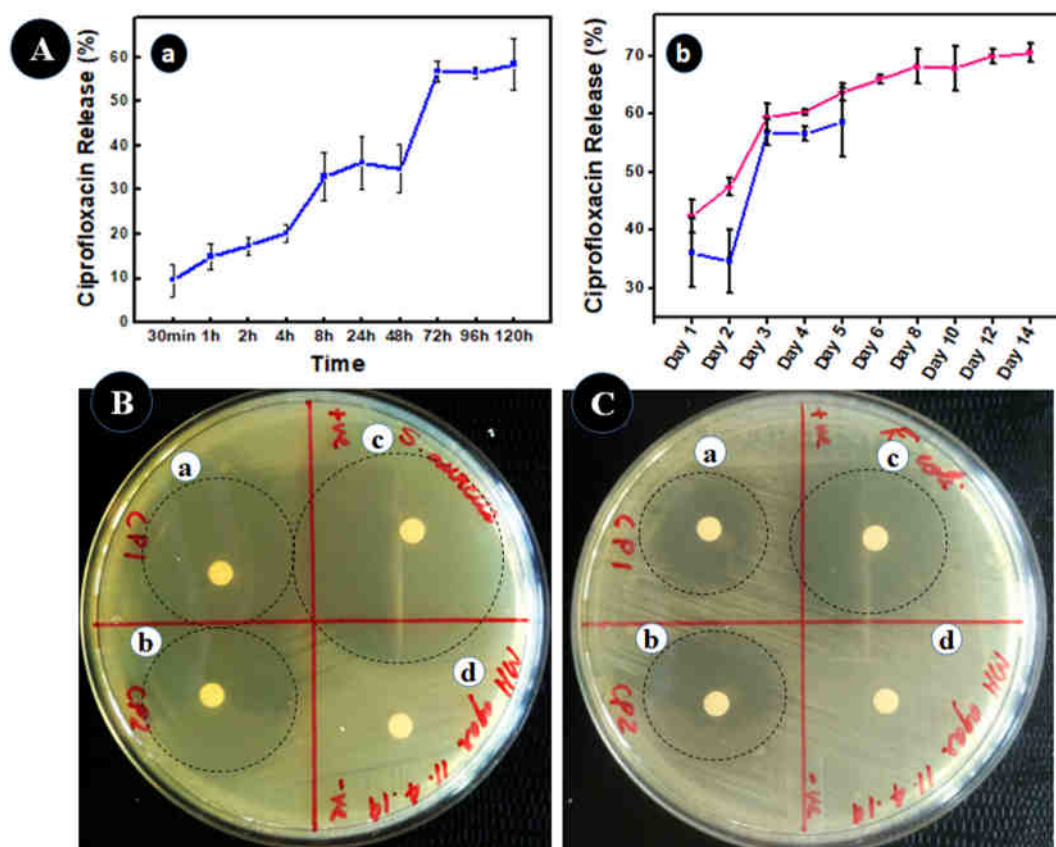
**Fig. 10.** Time-dependent antibiotic – release from CPH-P-PET [A(a): short-term release for 5 days; A(b): combined graph of drug release for 5 days (blue line) and two weeks (pink line)] and inhibition of bacterial growth [*S. aureus* (B) and *E. coli* (C)] on agar plates. B(a) represents extract collected at 8 h and B(b) represents extract collected at 24 h. Positive control B(c) is ciprofloxacin (3 μg/20 μL) and negative control B(d) is Milli-Q water. Note: all values are presented as mean ± SD. (For interpretation of the references to colour in this figure legend, the reader is referred to the web version of this article.)
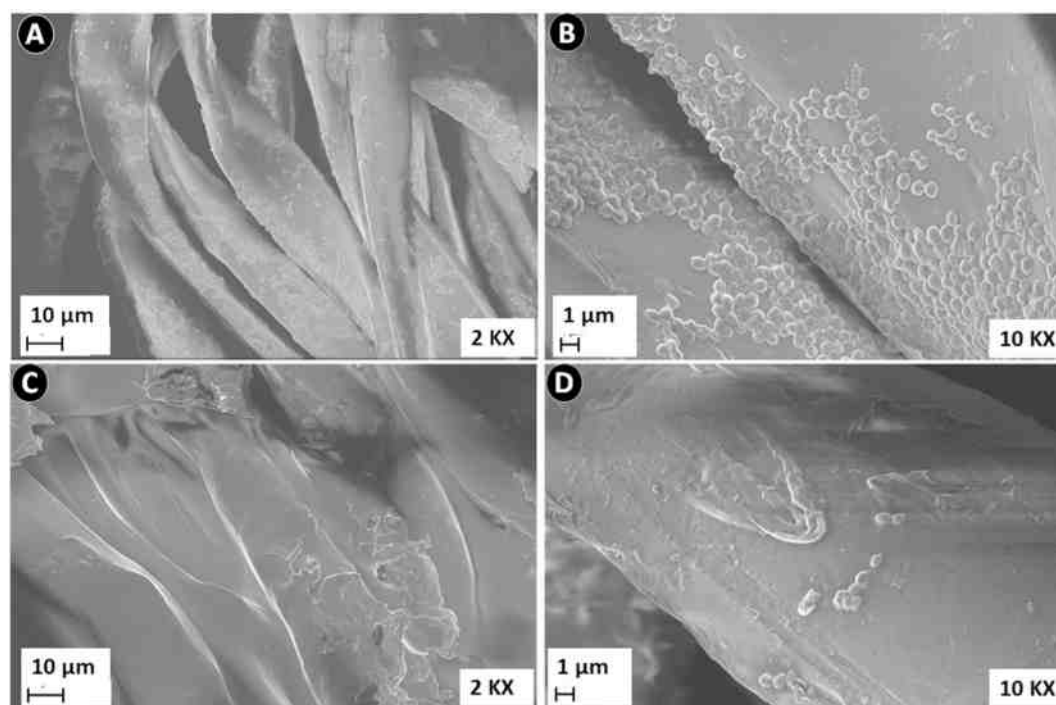


**Fig. 11.** Anti-adhesion assay performed in *S. aureus* suspension. (A) and (B) represent P-PET while (C) and (D) represent CPH-P-PET at two different magnifications.

surface functionalization of the scaffold [72]. *In vitro* mineralization is a typical indicator of bone regeneration potential of a scaffold in tissue engineering, in specific, the biomimetic nucleation, growth and deposition of calcium phosphate in the form of hydroxyapatite - the inorganic component of bone - supports bone repair and regeneration [48,73,74]. The increased Ca/P ratio attained in CPH-P-PET has indicated that neither poly (HEMA) coating nor ciprofloxacin loading alter the mineralization potential of the scaffold which is highly significant in dictating the dual functionality of CPH-P-PET. It is noteworthy to mention that the mineralization profile of P-PET is similar to our previous reports on surface phosphorylated PVA and poly (HEMA-*co*-MMA) [39,40].

Generally, biomineralization is an intrinsic feature of bone repair and formation [64,65]. The red and black nodules appeared after ARS and von Kossa staining, respectively, have provided authentic proof for the *in vitro* biomineralization potential of CPH-P-PET. Additionally, it has already been known that the activity of several markers such as ALP and OSN vary at different stages of osteogenesis [75,76]. Since ALP is an early marker of osteogenic differentiation, its activity is normally reduced after 14 days and the cells enter to next stage of differentiation with higher OSN activity [7,75–77]. Hence, our findings provide additional strong evidences for the osteoinductive potential of P-PET.

While considering a dual functioning system against bone infections, localized delivery of antibiotic to control the growth of causative microorganism is a necessity. Hence, an osteoinductive scaffold system with activity against microorganisms is ideal for bone tissue engineering. In addition, the first few days of post-surgical period is crucial as it is more prone to major infections. In this work, ciprofloxacin was impregnated in poly (HEMA) hydrogel for surface transformation of P-PET as a dual functional system with the goal to annihilate bone infections such as osteomyelitis. Antibiotic release up to ~60% within 5 days and ~70% within 14 days was observed and it was found to be effective against *S. aureus* and *E. coli* substantiating the efficacy of CPH-P-PET in bone infections. Moreover, CPH-P-PET has prohibited the adhesion of major causative organism of bone infection, *S. aureus*, on its surface which might be attributed to the activity of ciprofloxacin present on the scaffold. It could be perceived from the aforementioned research observations that CPH-P-PET trigger osteoinduction and exhibit controlled antibiotic release profile in addition to basic pre-requisites anticipated for a functional bone graft.

## 5. Conclusions

Post-operative contaminations and other mode of bacterial invasion could direct to severe bone infections, particularly osteomyelitis. A better treatment strategy with potential to localized antibiotic delivery, at the same time, regeneration of infected bone area is in need to mitigate the setbacks of conventional prophylaxis. In this scenario, we have designed a dual functioning PET based scaffold to address infection and provide a platform for the repair and regeneration of damaged bone. The CPH-P-PET was found as an excellent antibiotic delivery vehicle based on the cumulative release profile of ciprofloxacin. *In vitro* apatite formation and other biofunctional assays depicts its proficiency in new bone formation. Confirmative evidences from the expression of osteogenic biomarkers - ALP and OSN - in rat BMCs elucidated the osteoinductive nature of the scaffold. Altogether, the antibiotic carrying surface-transformed PET is a good dual-functional scaffold for bone regeneration and to prohibit bone-specific infections.

## Authors' contributions

SS has performed the experiment, analyzed the data and written the manuscript. MCV has offered the original PET fibrous matrix for the study. SGS has conceived the idea, supervised the work in timely manner and edited the manuscript. HKV has provided overall guidance for the successful completion of this work.

## Appendix A. Supplementary data

Supplementary data to this article can be found online at https://doi.org/10.1016/j.msec.2019.110491.

## References

[1] A.-M. Yousefi, P.F. James, R. Akbarzadeh, A. Subramanian, C. Flavin, H. Oudadesse, Prospect of stem cells in bone tissue engineering: a review, Stem Cells Int. 2016 (2016) 1–13, https://doi.org/10.1155/2016/6180487.

[2] S. Dhivya, A. Keshav Narayan, R. Logith Kumar, S. Viji Chandran, M. Vairamani, N. Selvamurugan, Proliferation and differentiation of mesenchymal stem cells on scaffolds containing chitosan, calcium polyphosphate and pigeonite for bone tissue engineering, Cell Prolif. 51 (1) (2018) 1–13, https://doi.org/10.1111/cpr.12408.

[3] S. Sancilio, M. Gallorini, C. Di Nisio, E. Marsich, R. Di Pietro, H. Schweikl, A. Cataldi, Alginate/hydroxyapatite-based nanocomposite scaffolds for bone tissue engineering improve dental pulp biomineralization and differentiation, Stem Cells Int. 2018 (2018) 1–13, https://doi.org/10.1155/2018/9643721.

[4] P. Datta, J. Chatterjee, S. Dhara, Electrospun nanofibers of a phosphorylated polymer-a bioinspired approach for bone graft applications, Colloids Surf. B. Biointerfaces 94 (2012) 177–183, https://doi.org/10.1016/j.colsurfb.2012.01.033.

[5] T. Jiang, S.P. Nukavarapu, M. Deng, E. Jabbarzadeh, M.D. Kofron, S.B. Doty, W.I. Abdel-Fattah, C.T. Laurencin, Chitosan-poly(Lactide-Co-Glycolide) microsphere-based scaffolds for bone tissue engineering: in vitro degradation and in vivo bone regeneration studies, Acta Biomater. 6 (9) (2010) 3457–3470, https://doi.org/10.1016/j.actbio.2010.03.023.

[6] W.W. Thein-Han, R.D.K. Misra, Biomimetic chitosan–nanohydroxyapatite composite scaffolds for bone tissue engineering, Acta Biomater. 5 (4) (2008) 1182–1197, https://doi.org/10.1016/j.actbio.2008.11.025.

[7] M. Shi, R. Yang, Q. Li, K. Lv, R.J. Miron, J. Sun, M. Li, Y. Zhang, Inorganic self-assembled bioactive artificial proto-osteocells inducing bone regeneration, ACS Appl. Mater. Interfaces 10 (13) (2018) 10718–10728, https://doi.org/10.1021/acsami.8b00385.

[8] P. Janicki, G. Schmidmaier, What should be the characteristics of the ideal bone graft substitute? Combining scaffolds with growth factors and/or stem cells, Injury 42 (Suppl. 2) (2011) S77–S81, https://doi.org/10.1016/j.injury.2011.06.014.

[9] L.H. Chiu, W.F.T. Lai, S.F. Chang, C.C. Wong, C.Y. Fan, C.L. Fang, Y.H. Tsai, The effect of type II collagen on MSC osteogenic differentiation and bone defect repair, Biomaterials 35 (9) (2014) 2680–2691, https://doi.org/10.1016/j.biomaterials.2013.12.005.

[10] W. Wei, J. Li, S. Chen, M. Chen, Q. Xie, H. Sun, J. Ruan, H. Zhou, X. Bi, A. Zhuang, et al., In vitro osteogenic induction of bone marrow mesenchymal stem cells with a decellularized matrix derived from human adipose stem cells and in vivo implantation for bone regeneration, J. Mater. Chem. B (2017) 2468–2482, https://doi.org/10.1039/c6tb03150a.

[11] S. Zang, L. Zhu, K. Luo, R. Mu, F. Chen, X. Wei, X. Yan, B. Han, X. Shi, Q. Wang, et al., Chitosan composite scaffold combined with bone marrow-derived mesenchymal stem cells for bone regeneration: in vitro and in vivo evaluation, Oncotarget 8 (67) (2017) 110890–110903, https://doi.org/10.18632/oncotarget.22917.

[12] J.H. Calhoun, M.M. Manring, M. Shirtliff, Osteomyelitis of the long bones, Semin. Plast. Surg. 23 (2) (2009) 59–72, https://doi.org/10.1055/s-0029-1214158.

[13] U. Furustrand Tafin, B. Betrisey, M. Bohner, T. Ilchmann, A. Trampuz, M. Clauss, Staphylococcal biofilm formation on the surface of three different calcium phosphate bone grafts: a qualitative and quantitative in vivo analysis, J. Mater. Sci. Mater. Med. 26 (3) (2015), https://doi.org/10.1007/s10856-015-5467-6.

[14] S.J. McConoughey, R. Howlin, J.F. Granger, M.M. Manring, J.H. Calhoun, M. Shirtliff, S. Kathju, P. Stoodley, Biofilms in periprosthetic orthopedic infections, Future Microbiol. 9 (8) (2014) 987–1007, https://doi.org/10.2217/fmb.14.64.

[15] M. Clauss, U. Furustrand Tafin, A. Bizzini, A. Trampuz, T. Ilchmann, Biofilm formation by staphylococci on fresh, fresh-frozen and processed human and bovine bone grafts, Eur. Cell. Mater. 25 (2012) 159–166, https://doi.org/10.22203/eCM.v025a11.

[16] D. Neut, H. Van De Belt, J.R. Van Horn, H.C. Van Der Mei, H.J. Busscher, Residual gentamicin-release from antibiotic-loaded polymethylmethacrylate beads after 5

years of implantation, Biomaterials 24 (10) (2003) 1829–1831, https://doi.org/10.1016/S0142-9612(02)00614-2.

[17] M. Lu, J. Liao, J. Dong, J. Wu, H. Qiu, X. Zhou, J. Li, D. Jiang, T.C. He, Z. Quan, An effective treatment of experimental osteomyelitis using the antimicrobial titanium/silver-containing NHP66 (nano-hydroxyapatite/polyamide-66) nanoscaffold biomaterials, Sci. Rep. 6 (July) (2016) 39174, https://doi.org/10.1038/srep39174.

[18] A.A. Beardmore, D.E. Brooks, J.C. Wenke, D.B. Thomas, Effectiveness of local antibiotic delivery with an osteoinductive and osteoconductive bone-graft substitute, J. Bone Jt. Surg. - Ser. A 87 (1) (2005) 107–112, https://doi.org/10.2106/JBJS.C.01670.

[19] W. Zhang, G. Lei, Y. Liu, W. Wang, T. Song, J. Fan, Approach to osteomyelitis treatment with antibiotic loaded PMMA, Microb. Pathog. 102 (2017) 42–44, https://doi.org/10.1016/j.micpath.2016.11.016.

[20] D. Senn, S. Gehmert, P.E. Ochsner, K.-D. Kühn, A.M. Nowakowski, Therapy for chronic recurrent osteomyelitis with multi-resistant pseudomonas aeruginosa using local antibiotic release by a polymethylmethacrylate custom-made tibia nail, Surg. Infect. Case Reports 2 (1) (2017) 26–30, https://doi.org/10.1089/crsi.2017.0005.

[21] A.D. Hanssen, M.J. Spangehl, Practical applications of antibiotic-loaded bone cement for treatment of infected joint replacements, Clin. Orthop. Relat. Res. (427) (2004) 79–85, https://doi.org/10.1097/01.blo.0000143806.72379.7d.

[22] T. Mcmahon, P.C.M.V. Zijl, A.A. Gilad, Phase composition control of calcium phosphate nanoparticles for tunable drug delivery kinetics and treatment of osteomyelitis. Part 2: antibacterial and osteoblastic response, 27 (3) (2015) 320–331, https://doi.org/10.1002/nbm.3066.Non-invasive.

[23] M. Zilberman, J.J. Elsner, Antibiotic-eluting medical devices for various applications, J. Control. Release 130 (3) (2008) 202–215, https://doi.org/10.1016/j.jconrel.2008.05.020.

[24] K. Anagnostakos, K. Schrder, Antibiotic-impregnated bone grafts in orthopaedic and trauma surgery: a systematic review of the literature, Int. J. Biomater. 2012 (2012), https://doi.org/10.1155/2012/538061.

[25] C.A. García-González, J. Barros, A. Rey-Rico, P. Redondo, J.L. Gómez-Amoza, A. Concheiro, C. Alvarez-Lorenzo, F.J. Monteiro, Antimicrobial properties and osteogenicity of vancomycin-loaded synthetic scaffolds obtained by supercritical foaming, ACS Appl. Mater. Interfaces 10 (4) (2018) 3349–3360, https://doi.org/10.1021/acsami.7b17375.

[26] M. Cicuéndez, J.C. Doadrio, A. Hernández, M.T. Portolés, I. Izquierdo-Barba, M. Vallet-Regí, Multifunctional pH sensitive 3D scaffolds for treatment and prevention of bone infection, Acta Biomater. 65 (2018) 450–461, https://doi.org/10.1016/j.actbio.2017.11.009.

[27] T.A.G. van Vugt, J. Geurts, J.J. Arts, Clinical application of antimicrobial bone graft substitute in osteomyelitis treatment: a systematic review of different bone graft substitutes available in clinical treatment of osteomyelitis, Biomed. Res. Int. 2016 (2016) 1–9, https://doi.org/10.1155/2016/6984656.

[28] N. Dunne, F. Buchanan, J. Hill, C. Newe, M. Tunney, A. Brady, G. Walker, In vitro testing of chitosan in gentamicin-loaded bone cement: no antimicrobial effect and reduced mechanical performance, Acta Orthop. 79 (6) (2008) 851–860, https://doi.org/10.1080/17453670810016957.

[29] J.C. Elena Filova, Endothelial cell lining of PET vascular prostheses: modification with degradable polyester-based copolymers and adhesive protein multi-layers, J Tissue Sci Eng 5 (2) (2014), https://doi.org/10.4172/2157-7552.1000139.

[30] S.H. Tang, M.Y. Domino, A. Venault, H.T. Lin, C. Hsieh, A. Higuchi, A. Chinnathambi, S.A. Alharbi, L.L. Tayo, Y. Chang, Bioinert control of Zwitterionic poly(ethylene terephthalate) fibrous membranes, Langmuir 35 (5) (2019) 1727–1739, https://doi.org/10.1021/acs.langmuir.8b00604.

[31] T. Saito, M. Takemoto, A. Fukuda, Y. Kuroda, S. Fujibayashi, M. Neo, D. Honjoh, T. Hiraide, T. Kizuki, T. Kokubo, et al., Effect of titania-based surface modification of polyethylene terephthalate on bone-implant bonding and peri-implant tissue reaction, Acta Biomater. 7 (4) (2011) 1558–1569, https://doi.org/10.1016/j.actbio.2010.11.018.

[32] C.H. Wang, Z.S. Guo, F. Pang, L.Y. Zhang, M. Yan, J.H. Yan, K.W. Li, X.J. Li, Y. Li, L. Bi, et al., Effects of graphene modification on the bioactivation of polyethylene-terephthalate-based artificial ligaments, ACS Appl. Mater. Interfaces 7 (28) (2015) 15263–15276, https://doi.org/10.1021/acsami.5b02893.

[33] S. Wang, Y. Ge, C. Ai, J. Jiang, J. Cai, D. Sheng, F. Wan, X. Liu, Y. Hao, J. Chen, S. Chen, Enhance the biocompatibility and osseointegration of polyethylene terephthalate ligament by plasma spraying with hydroxyapatite in vitro and in vivo, Int. J. Nanomedicine 13 (2018) 3609–3623, https://doi.org/10.2147/IJN.S162466.

[34] H. Li, C. Wu, J. Chang, Y. Ge, S. Chen, Functional polyethylene terephthalate with nanometer-sized bioactive glass coatings stimulating in vitro and in vivo osseointegration for anterior cruciate ligament reconstruction, Adv. Mater. Interfaces 1 (5) (2014) 1–10, https://doi.org/10.1002/admi.201400027.

[35] A. Pellis, C. Gamerith, G. Ghazaryan, A. Ortner, E. Herrero Acero, G.M. Guebitz, Ultrasound-enhanced enzymatic hydrolysis of poly(ethylene terephthalate), Bioresour. Technol. 218 (2016) 1298–1302, https://doi.org/10.1016/j.biortech.2016.07.106.

[36] I. Onyshchenko, A.Y. Nikiforov, N. De Geyter, R. Morent, Local analysis of pet surface functionalization by an atmospheric pressure plasma jet, Plasma Process. Polym. 12 (5) (2015) 466–476, https://doi.org/10.1002/ppap.201400166.

[37] M. Kanelli, S. Vasilakos, E. Nikolaivits, S. Ladas, P. Christakopoulos, E. Topakas, Surface modification of poly(ethylene terephthalate) (PET) fibers by a cutinase from fusarium oxysporum, Process Biochem. 50 (11) (2015) 1885–1892, https://doi.org/10.1016/j.procbio.2015.08.013.

[38] M. Parvinzadeh Gashti, I. Ebrahimi, M. Pousti, New insights into corona discharge surface ionization of polyethylene terephthalate via a combined computational and experimental assessment, Curr. Appl. Phys. 15 (9) (2015) 1075–1083, https://doi.org/10.1016/j.cap.2015.06.009.

[39] G.S. Sailaja, T.V. Kumari, Y. Yokogawa, H.K. Varma, In vitro mineralization and cell adhesion on surface modified poly (2 - hydroxy ethyl methacrylate-co-methyl methacrylate), Key Eng. Mater. 309–311 (2009) 493–496, https://doi.org/10.4028/www.scientific.net/kem.309-311.493.

[40] G.S. Sailaja, K. Sreenivasan, Y. Yokogawa, T.V. Kumary, H.K. Varma, Bioinspired mineralization and cell adhesion on surface functionalized poly(vinyl alcohol) films, Acta Biomater. 5 (5) (2009) 1647–1655, https://doi.org/10.1016/j.actbio.2008.12.005.

[41] S.S. Gopalakrishnanchettiyar, M. Mohanty, T.V. Kumary, M.P. Valappil, R. Parameshwaran, H.K. Varma, Surface-phosphorylated copolymer promotes direct bone bonding, Tissue Eng. Part A 15 (10) (2009) 3061–3069, https://doi.org/10.1089/ten.tea.2008.0454.

[42] Q.P. Pham, U. Sharma, A.G. Mikos, Electrospun poly (ε-caprolactone) microfiber and multilayer nanofiber/microfiber scaffolds: characterization of scaffolds and measurement of cellular infiltration, Biomacromolecules 7 (10) (2006) 2796–2805, https://doi.org/10.1021/bm060680j.

[43] A.G. Namboodiri, R. Parameswaran, Fibro-porous polycaprolactone membrane containing extracts of biophytum sensitivum: a prospective antibacterial wound dressing, J. Appl. Polym. Sci. 129 (4) (2013) 2280–2286, https://doi.org/10.1002/app.38950.

[44] G.S. Sailaja, P. Ramesh, H.K. Varma, Swelling behavior of hydroxyapatite-filled chitosan-poly(acrylic acid) polyelectrolyte complexes, J. Appl. Polym. Sci. 100 (6) (2006) 4716–4722, https://doi.org/10.1002/app.23058.

[45] H.M. Younes, E. Bravo-Grimaldo, B.G. Amsden, Synthesis, characterization and in vitro degradation of a biodegradable elastomer, Biomaterials 25 (22) (2004) 5261–5269, https://doi.org/10.1016/j.biomaterials.2003.12.024.

[46] X. Ding, G. Yang, W. Zhang, G. Li, S. Lin, D.L. Kaplan, X. Jiang, Increased stem cells delivered using a silk gel/scaffold complex for enhanced bone regeneration, Sci. Rep. 7 (1) (2017) 1–10, https://doi.org/10.1038/s41598-017-02053-z.

[47] Morgan, D. M. L. Tetrazolium (MTT) assay for cellular viability and activity. Polym. Protoc. 79 (4), 179–184. doi:https://doi.org/10.1385/0-89603-448-8:179.

[48] T. Kokubo, H. Takadama, How useful is SBF in predicting in vivo bone bioactivity? Biomaterials 27 (15) (2006) 2907–2915, https://doi.org/10.1016/j.biomaterials.2006.01.017.

[49] C.A. Gregory, W.G. Gunn, A. Peister, D.J. Prockop, An alizarin red-based assay of mineralization by adherent cells in culture: comparison with cetylpyridinium chloride extraction, Anal. Biochem. 329 (1) (2004) 77–84, https://doi.org/10.1016/j.ab.2004.02.002.

[50] J.H. Lee, J.W. Rhie, D.Y. Oh, S.T. Ahn, Osteogenic differentiation of human adipose tissue-derived stromal cells (HASCs) in a porous three-dimensional scaffold, Biochem. Biophys. Res. Commun. 370 (3) (2008) 456–460, https://doi.org/10.1016/j.bbrc.2008.03.123.

[51] M. Bodo, C. Lilli, C. Bellucci, P. Carinci, M. Calvitti, F. Pezzetti, G. Stabellini, S. Bellocchio, C. Balducci, F. Carinci, et al., Basic fibroblast growth factor autocrine loop controls human osteosarcoma phenotyping and differentiation, Mol. Med. 8 (7) (2018) 393–404, https://doi.org/10.1007/bf03402020.

[52] E.K. Ko, S.I. Jeong, N.G. Rim, Y.M. Lee, H. Shin, B.-K. Lee, In vitro osteogenic differentiation of human mesenchymal stem cells and in vivo bone formation in composite nanofiber meshes, Tissue Eng. Part A 14 (12) (2008) 2105–2119, https://doi.org/10.1089/ten.tea.2008.0057.

[53] O.H. Lowry, N.J. Rosebrough, A.L. Farr, R.J. Randall, The Folin by Oliver, J. Biol. Chem. 193 (1951) 265–275.

[54] N. Hassani Besheli, F. Mottaghitalab, M. Eslami, M. Gholami, S.C. Kundu, D.L. Kaplan, M. Farokhi, Sustainable release of vancomycin from silk fibroin nanoparticles for treating severe bone infection in rat tibia osteomyelitis model, ACS Appl. Mater. Interfaces 9 (6) (2017) 5128–5138, https://doi.org/10.1021/acsami.6b14912.

[55] B.M. Al Meslmani, G.F. Mahmoud, T. Leichtweiß, B. Strehlow, F.O. Sommer, M.D. Lohoff, U. Bakowsky, Covalent immobilization of lysozyme onto woven and knitted crimped polyethylene terephthalate grafts to minimize the adhesion of broad spectrum pathogens, Mater. Sci. Eng. C 58 (2016) 78–87, https://doi.org/10.1016/j.msec.2015.08.001.

[56] M. Edge, R. Wiles, N.S. Allen, W.A. McDonald, S.V. Mortlock, Characterisation of the species responsible for yellowing in melt degraded aromatic polyesters - I: yellowing of poly(ethylene terephthalate), Polym. Degrad. Stab. 53 (2) (1996) 141–151, https://doi.org/10.1016/0141-3910(96)00081-X.

[57] R.M. Silverstein, F.X. Webster, Spectrometric Identification of Organic Compounds, 3rd edition, 30 (2002), https://doi.org/10.1016/0022-2860(76)87024-x.

[58] Z. Wang, T. Jiang, S. Sauro, Y. Wang, I. Thompson, T.F. Watson, Y. Sa, W. Xing, Y. Shen, M. Haapasalo, Dentine remineralization induced by two bioactive glasses developed for air abrasion purposes, J. Dent. 39 (11) (2011) 746–756, https://doi.org/10.1016/j.jdent.2011.08.006.

[59] B. Zheng, C. Mao, T. Gu, H. Pan, C. Shao, J. Sun, C. Chen, R. Tang, X. Gu, Phosphorylated chitosan to promote biomimetic mineralization of type I collagen as a strategy for dentin repair and bone tissue engineering, New J. Chem. 43 (4) (2019) 2002–2010, https://doi.org/10.1039/c8nj04889d.

[60] E. Vargün, A. Usanmaz, Degradation of poly(2-hydroxyethyl methacrylate) obtained by radiation in aqueous solution, J. Macromol. Sci. Part A Pure Appl. Chem. 47 (9) (2010) 882–891, https://doi.org/10.1080/10601325.2010.501304.

[61] R.T. Tom, V. Suryanarayanan, P.G. Reddy, S. Baskaran, T. Pradeep, Ciprofloxacin-protected gold nanoparticles, 13 (2004) 1909–1914.

[62] W. Jie, F. Song, X. Li, W. Li, R. Wang, Y. Jiang, L. Zhao, Z. Fan, J. Wang, B. Liu, Enhancing the proliferation of MC3T3-E1 cells on casein phosphopeptide-bio-functionalized 3D reduced-graphene oxide/polypyrrole scaffolds, RSC Adv. 7 (55) (2017) 34415–34424, https://doi.org/10.1039/c7ra02146a.

[63] G. Galo Silva, M.L. da C. Valente, L. Bachmann, A.C. dos Reis, Use of polyethylene

terephthalate as a prosthetic component in the prosthesis on an overdenture implant, Mater. Sci. Eng. C 99 (January 2018) (2019) 1341–1349, https://doi.org/10.1016/j.msec.2019.01.136.

[64] K.T. Shalumon, G.J. Lai, C.H. Chen, J.P. Chen, Modulation of bone-specific tissue regeneration by incorporating bone morphogenetic protein and controlling the shell thickness of silk fibroin/chitosan/nanohydroxyapatite core-shell nanofibrous membranes, ACS Appl. Mater. Interfaces 7 (38) (2015) 21170–21181, https://doi.org/10.1021/acsami.5b04962.

[65] S.N. Meloan, M. Holde Puchtler, Chemical Mechanisms of Staining Methods, (1985).

[66] M.I. Janssen, M.B.M. Van Leeuwen, K. Scholtmeijer, T.G. Van Kooten, L. Dijkhuizen, H.A.B. Wösten, Coating with genetic engineered hydrophobin promotes growth of fibroblasts on a hydrophobic solid, Biomaterials 23 (24) (2002) 4847–4854, https://doi.org/10.1016/S0142-9612(02)00240-5.

[67] M. Thomas, A. Arora, D.S. Katti, Surface hydrophilicity of PLGA fibers governs in vitro mineralization and osteogenic differentiation, Mater. Sci. Eng. C 45 (2014) 320–332, https://doi.org/10.1016/j.msec.2014.08.074.

[68] K.Y. Law, Definitions for hydrophilicity, hydrophobicity, and superhydrophobicity: getting the basics right, J. Phys. Chem. Lett. 5 (4) (2014) 686–688, https://doi.org/10.1021/jz402762h.

[69] N. Fukuda, M. Kanazawa, K. Tsuru, A. Tsuchiya, R. Sunarso; Toita, Y. Mori, Y. Nakashima, K. Ishikawa, Synergistic effect of surface phosphorylation and microroughness on enhanced osseointegration ability of poly(ether ether ketone) in the rabbit tibia, Sci. Rep. 8 (1) (2018) 1–10, https://doi.org/10.1038/s41598-018-35313-7.

[70] A.C. Parker, J.K. Smith, H.S. Courtney, W.O. Haggard, Evaluation of two sources of calcium sulfate for a local drug delivery system: a pilot study, Clin. Orthop. Relat. Res. 469 (11) (2011) 3008–3015, https://doi.org/10.1007/s11999-011-1911-1.

[71] L. Tang, P. Thevenot, W. Hu, Surface chemistry influences implant biocompatibility, Curr. Top. Med. Chem. 8 (4) (2008) 270–280, https://doi.org/10.2174/156802608783790901.

[72] M. Lotfi, M. Nejib, M. Naceur, Cell adhesion to biomaterials: concept of biocompatibility, Adv. Biomater. Sci. Biomed. Appl. (2013), https://doi.org/10.5772/53542.

[73] K. Shin, T. Acri, S. Geary, A.K. Salem, Biomimetic mineralization of biomaterials using simulated body fluids for bone tissue engineering and regenerative medicine, Tissue Eng. Part A 23 (19–20) (2017) 1169–1180, https://doi.org/10.1089/ten.tea.2016.0556.

[74] M. Tanahashi, T. Matsuda, Surface functional group dependence on apatite formation on self- assembled monolayers in a simulated body fluid, J. Biomed. Mater. Res. 34 (3) (1997) 305–315, https://doi.org/10.1002/(SICI)1097-4636(19970305)34:3<305::AIDJBM5>3.0 (CO;2-O).

[75] E.E. Golub, K. Boesze-Battaglia, The role of alkaline phosphatase in mineralization, Curr. Opin. Orthop. 18 (5) (2007) 444–448, https://doi.org/10.1097/BCO.0b013e3282630851.

[76] Y.T. Tsao, Y.J. Huang, H.H. Wu, Y.A. Liu, Y.S. Liu, O.K. Lee, Osteocalcin mediates biomineralization during osteogenic maturation in human mesenchymal stromal cells, Int. J. Mol. Sci. 18 (1) (2017), https://doi.org/10.3390/ijms18010159.

[77] J. Nourmohammadi, F. Roshanfar, M. Farokhi, M. Haghbin Nazarpak, Silk fibroin/kappa -carrageenan composite scaffolds with enhanced biomimetic mineralization for bone regeneration applications, Mater. Sci. Eng. C 76 (2017) 951–958, https://doi.org/10.1016/j.msec.2017.03.166.